Characterization of ultrashort double pulses and their application in attosecond physics

PHD THESIS

Author:

Lénárd Gulyás Oldal

Supervisor:

Balázs Major

SENIOR RESEARCH FELLOW

Extreme Light Infrastructure - Attosecond Light Pulse Source

DOCTORAL SCHOOL OF PHYSICS

DEPARTMENT OF OPTICS AND QUANTUM ELECTRONICS

UNIVERSITY OF SZEGED

FACULTY OF SCIENCE AND INFORMATICS

SZEGED

2021

Contents

List of Abbreviations

AC	**A**lternating **C**urrent (derived from alternating electric field)	váltakozó elektromos tér
APT	**A**ttosecond **P**ulse **T**rain	attoszekundumos impulzussorozat
BBO	**B**eta-**B**arium **BO**rate	β-bárium-borát
CEP	**C**arrier **E**nvelope **P**hase	vivő-burkoló fázis
DC	**D**irect **C**urrent (derived from static electric field)	statikus elektromos tér
DFG	**D**ifference **F**requency **G**eneration	különbségfrekvencia-keltés
DP	**D**ouble-**P**ulse	kettős impulzus
FOD	**F**ourth-**O**rder **D**ispersion	negyedrendű diszperzió
FROG	**F**requency **R**esolved **O**ptical **G**ating	frekvenciabontott optikai kapuzás
FTSI	**F**ourier **T**ransform **S**pectral **I**nterferometry	Fourier transzformációs spektrális interferometria
FWHM	**F**ull **W**idth at **H**alf **M**aximum	félértékszélesség
GD	**G**roup **D**elay	csoportkésleltetés
GDD	**G**roup **D**elay **D**ispersion	csoportkésleltetés-diszperzió
GHHG	**G**as **H**igh **H**armonic **G**eneration	magasrendű felharmonikus-keltés gáznemű anyagban
HHG	**H**igh **H**armonic **G**eneration	magasrendű felharmonikus-keltés
IAP	**I**solated **A**ttosecond **P**ulse	izolált attoszekundumos impulzus
IR	**I**nfra**R**ed	infravörös
LASER	**L**ight **A**mplification by the **S**timulated **E**mission of **R**adiation	fényerősítés kényszerített emissziós sugárzással
PG	**P**olarization-**G**ate	polarizáció-kapu
RABBITT	**R**econstruction of **A**ttosecond harmonic **B**eating **B**y **I**nterference of **T**wo-photon **T**ransitions	interferometrikus, kétfoton-átmeneten alapuló attoszekundumos impulzussorozat rekonstruálás
SD	**S**elf-**D**iffraction	öndiffrakció
SDU	**S**plit-and-**D**elay **U**nit	osztó-késleltető elem
SFA	**S**trong-**F**ield **A**pproximation	erős tér közelítés
SFG	**S**um-**F**requency **G**eneration	összegfrekvencia-keltés
SHG	**S**econd-**H**armonic **G**eneration	másodharmonikus-keltés
SPIDER	**S**pectral **P**hase **I**nterferometry for **D**irect **E**lectric field **R**econstruction	spektrális fázisinterferometria az elektromos tér közvetlen visszanyeréséhez
SPA	**S**addle-**P**oint **A**pproximation	nyeregponti közelítés
SRI	**S**pectrally **R**esolved **I**nterferometry	spektrálisan bontott interferometria

SRSI	**S**elf-**R**eferenced **S**pectral **I**nterferometry	önreferenciás spektrális interferometria
SSRI	**S**pectrally and **S**patially **R**esolved spectral **I**nterferometry	spektrálisan és térben bontott spektrális interferometria
TDSE	**T**ime-**D**ependent **S**chrödinger **E**quation	időfüggő Schrödinger-egyenlet
TG	**T**ransient-**G**rating	átmeneti rács
THG	**T**hird-**H**armonic **G**eneration	harmadharmonikus-keltés
TOD	**T**hird-**O**rder **D**ispersion	harmadrendű diszperzió
TSM	**T**hree-**S**tep **M**odel	háromlépcsős modell
UV	**U**lta**V**iolet	ultraibolya
XPW	**C**ross-**P**olarized **W**ave	keresztpolarizált hullám
XUV	e**X**treme **U**ltra**V**iolet	extrém ultraibolya

Chapter 1

Introduction

Light is an indispensable part of our life, yet we cannot touch it directly. Light allows us to perceive objects, creatures or our fellow beings, in other words, it allows us to see. Light is one of the fundamental natural elements, similarly to water or oxygen, however it is not a vital element. It is in fact electromagnetic radiation the mediating particles of which are the photons, which behave either as waves or particles, depending on the investigated physical effect. Electromagnetic radiation can most simply be characterized by the frequency of the mediating photons, or by the corresponding wavelength, and can be divided into different subgroups based on the "colour" of the mediating particles. In other words, the broad spectrum of electromagnetic radiation represents light having different coloured photons.

During biological evolution, the human eye, or more precisely the photosensitive visual organ called retina, has evolved in a way to be able to detect photons only from a certain wavelength range. In other words, our eye is sensitive only to photons of specific colours. This section of the electromagnetic spectrum is commonly called "visible light". Our visual organ is completely insensitive to electromagnetic radiation outside this wavelength region, which can even pose danger, as our body, consisting of sensitive tissues, can be exposed to radiation without us realizing the potential hazard. Such electromagnetic waves are emitted, for instance, by the Sun, or other radiating heavenly bodies in other galaxies. Fortunately, injurious radiations from outer space is completely filtered out by the more than 10 km thick atmosphere of the Earth, so they cannot harm the human body.

Electromagnetic radiations cover a broad spectral range, starting from cosmic and gamma rays with a wavelength of only a few picometres, through the region of X-rays and visible light, up to the domain of infrared and radio waves having micrometre and several metre long wavelengths, respectively. Although the human eye is not capable of sensing such radiation, some of them have numerous well-known and very useful everyday applications. For example, X-rays are often applied in medicine for diagnostic imaging. Thermal cameras, used in the microelectronics and semiconductor industry, can detect infrared radiation. Furthermore, more and more residential properties are fitted with heating systems utilizing infrared radiation. Yet, the best known application is most probably the mobile phone. When in use, these devices emit

and receive radiation in the long wavelength region, i.e. radio frequency waves. Other well-known devices that utilize the advantages of radio frequency waves include routers used for wireless internet connection, or the Global Positioning System.

Lasers, the name of which comes from an acronym (Light Amplification by the Stimulated Emission of Radiation), also emit electromagnetic waves, however, with characteristics different from those of the applications summarized above. Because of the exceedingly advantageous and useful attributes of their radiation, they are applied in almost every major area of the industry. We encounter lasers during our everyday lives, even if we do not realize it. There are many laser types that emit light in the visible wavelength range, including barcode scanners used at the tills, laser pointers applied by teachers and conference speakers, modern printers or dental drilling devices. However, other kinds, which radiate in the ultraviolet or infrared wavelength region, i.e. outside the sensitivity range of the human eye, also have a wide range of applications. The devices applied for measuring the speed of cars, cutting, drilling and forging machinery used in the heavy metal and automotive industries, or medical equipment applied in vascular or eye surgeries emit "invisible" radiation.

Besides the colour of emitted photons, lasers can also be classified based on the temporal characteristics of their radiation. According to this categorization, we can distinguish two major types: lasers that have continuous wave radiation and lasers which emit pulse trains with a well-defined temporal separation between the emitted temporal peaks, i.e. pulsed lasers. Lasers belonging to the first group are most often used for machining metals, as they can achieve high average powers, necessary for processing solid materials. Pulsed lasers are often applied in medical applications. For this area of use, the laser beam is guided to the surface to be treated or even to the internal tissues under our skin by a flexible optical fibre, which steers light without a significant energy loss.

In addition to medical applications, pulsed lasers are also frequently used in research where ultrafast processes are investigated, as the temporal duration of their emitted pulses can go down to the femtosecond (1 fs = 10^{-15} s) range. This time period compares to a second as a second compares to ~ 32 million years. This means that we have such a short radiation that spans one millionth of one billionth of a second. For this reason, these ultrashort pulses are able to trace processes occurring within such a short time period, including changes in charge migration, coincidence measurements, and ultrafast nuclear reactions. However, the temporal duration of the pulses cannot be less than one optical cycle of the corresponding radiation. Accordingly, there exists a physical limit which prevents the production of arbitrary short laser pulses. However, certain nuclear reactions and other ultrafast processes can occur faster, so they cannot be examined by these pulsed lasers.

Due to this limitation, scientists have developed a method, called high-order harmonic generation using femtosecond laser sources to produce coherent radiation in the extreme ultraviolet wavelength region. The technique is based on the nonlinear frequency up-conversion of the driving laser, therefore the radiation emitted in the visible or in the near infrared wavelength range can be converted to the ultraviolet. The electromagnetic radiation produced in this way has a shorter wavelength as well as higher frequency than the driving laser source. Consequently, the pulse duration limit mentioned previously can be overcome, and the production of shorter pulses down to the attosecond (1 as = 10^{-18} s) range becomes feasible. This paves the way towards the experimental examination of processes occurring on such a short timescale, e.g. electron dynamics or other molecular and atomic processes.

Chapter 2

Scientific background

In the following section I will give a detailed overview about the most important features of femtosecond laser pulses, summarize their best-known temporal characterization techniques, and describe one of the experimental applications of ultrashort laser pulses, namely high-order harmonic generation (HHG).

The heart of a modern laser system is the laser oscillator, where the pulses are produced by pumping an active medium [1]. Pumping can be carried out by using flash lamps, electric discharge, or most commonly by using semiconducting diode lasers in various pumping geometries. Basically, the spectral and physical properties of the active medium, which can be semiconducting, solid or gas phase materials, determine the applicable pumping method and arrangement [2]. Upon leaving the laser oscillator, the produced radiation can be led to an amplification stage to increase the pulse energy through nonlinear processes. Finally, the temporally stretched pulses with increased energy must be temporally compressed to reach their final duration. Ultrafast laser amplifiers can emit these temporal peaks with a repetition rate of several Hz up to MHz, in the infrared (IR), visible and/or ultraviolet (UV) spectral regions, depending on the emission bandwidth of the utilized active media both in the oscillator and amplification stages of the laser system. The duration of the amplified and temporally compressed ultrashort laser pulses can vary on a timescale from picoseconds (1 ps = 10^{-12} s) to femtoseconds, with various electric field evolutions. After leaving the amplifier and compressor sections of the laser system, i.e. upon reaching their final energy level and duration, laser pulses are ready for further applications.

As the characteristics of laser radiation vary on a wide range, the application areas of emitted pulses are also very versatile. However, for most applications, the exact characteristics of the applied pulses must be known, otherwise the expected outcome cannot be reached. Such characteristics are the laser's average power, pulse energy, as well as the spectral and temporal evolution of radiation. The average power can be easily measured by power meters, and by knowing the laser repetition rate, the energy of a single pulse can also be quickly determined. We can simply measure and visualize the spectrum of a laser source too by using a commercially available spectrometer designed for the required wavelength range. However,

determination of the temporal evolution of laser pulses is a more challenging task. From a laser spectrum, recorded by a spectrometer, the so-called Fourier-limited temporal shape can be retrieved by applying the Fourier transform, which gives the minimum physically possible temporal duration of the pulse. But after leaving the laser system, laser pulses often propagate in air, go through glass plates or other transparent optics, such as lenses, or get reflected by mirrors. All these propagation effects change the temporal evolution of laser pulses [3], therefore their exact temporal shape must be measured before experimental use. Fortunately, in the last few decades laser scientists have developed several pulse characterization techniques, such as Spectral Phase Interferometry for Direct Electric field Reconstruction (SPIDER) [4], Frequency Resolved Optical Gating (FROG) [5], or Self-Referenced Spectral Interferometry (SRSI) [6].

For instance, in research fields where ultrafast processes are in the focus, it is necessary to know the exact time evolution of the laser electric field. Femtosecond lasers are one of the most powerful and valuable tools to investigate such phenomena. One of their major applications is to produce coherent radiation in the extreme ultraviolet (XUV) wavelength region via high harmonic generation [7], [8] on the surface of solids by creating plasma mirror, or by ionizing gaseous medium. Furthermore, high harmonics can also be generated in liquids or in solid bandgap materials [9]. However, because of the technical difficulties involved in these procedures, the latter are less widespread. The most often used medium for HHG is gaseous, where the generation of the coherent XUV can be described by three simple steps in the semiclassical approach [8]. To describe the HHG process in more detail, and to take into account more relevant physical effects, the quantum mechanical description must be used [10]. To this end, the time-dependent Schrödinger equation (TDSE) must be solved, which describes the interaction between a single atom and the strong laser field [11]. Although these calculations are extremely complex and time consuming, by making some assumptions (applying the so-called strong-field approximation (SFA)) the calculations can be significantly simplified [10]. In the model, the interacting atom is supposed to be hydrogen-like, thereby the calculation is simplified further. However, the model is extendable to describe more complex systems containing more than one atom, thus the main aspects of the experimental HHG can be predicted by these calculations.

2.1 Description of ultrashort laser pulses

As already mentioned above, laser pulses can be characterized by measurable quantities which strongly relate to the constructed electric field. Fundamentally, these quantities are real, however, in the context we often apply complex formalism to describe formulas. The $\tilde{E}(x, y, z, \omega)$ complex spectrum (the sign ~ above the quantity indicates the complex value), the real part measurable by spectrometers, and the corresponding $\tilde{E}(x, y, z, t)$ complex electric

field, determinable by pulse shape measuring techniques, are generally used to describe the radiation in the spectral (frequency), and in the temporal (time) domains, respectively [12]. In the frequency domain, the spectral bandwidth ($\Delta\omega_p$) is the parameter which provides the frequency span where the spectral components exceed half of the maximum value of the spectral intensity (often called as full width at half maximum (FWHM)). Similarly, in the time domain, the FWHM of a laser pulse (τ_p) is the characteristic width where the temporal components exceed half of the maximum temporal intensity. The relation between $\Delta\omega_p$ and τ_p is defined by the Fourier theorem, and for this reason these parameters cannot be changed independently from each other. The spectral bandwidth can be written as $\Delta\omega_p = 2\pi\Delta\nu_p$, where $\Delta\nu_p$ is the bandwidth expressed in frequency. In case of Gaussian-shape pulses, the theoretical limit connecting these parameters can be expressed as follows [13]:

$$\Delta\nu_p \times \tau_p \geq \frac{2ln2}{\pi} = 0.441. \tag{2.1}$$

In case of equality, the physical interpretation of the equation above is that only one shortest possible temporal duration exists in the time domain for a given spectral bandwidth. These pulses are called transform-limited, also known as Fourier-limited laser pulses. In every other case the time-bandwidth product is larger than the limit, written in Eqn. 2.1, as the duration of the laser pulse is longer than the transform-limited duration, for example, as a result of pulse propagation through different, optically transparent media. By taking into account all the pulse-distorting effects one can say the pulses are either chirped or dispersed. To describe the dispersion effects analytically, first of all the electric field must be described in detail, then the further propagation processes must be investigated.

2.1.1 Frequency- and time domain description of the electric field

Let us first consider the time-dependent part in the electric field only, neglecting the spatial components ($\boldsymbol{E}(x,y,z,t) = E(t)$) [14]. Then, the complex spectrum of the electric field can be defined by the complex Fourier transform ($\mathscr{F}$) of the electric field:

$$\tilde{E}(\omega) = \mathscr{F}\{E(t)\} = \int_{-\infty}^{\infty} E(t)e^{-i\omega t}dt = |\tilde{E}(\omega)|e^{i\Phi(\omega)}, \tag{2.2}$$

where $|\tilde{E}(\omega)|$ is the spectral amplitude, and $\Phi(\omega)$ denotes the spectral phase.

Since $E(t)$ is a real function, $\tilde{E}(\omega) = \tilde{E}^*(-\omega)$, therefore, if there is a given $\tilde{E}(\omega)$, the time-dependent electric field can be determined through the inverse Fourier transform ($\mathscr{F}^{-1}$):

$$E(t) = \mathscr{F}^{-1}\{\tilde{E}(\omega)\} = \frac{1}{2\pi} \int_{-\infty}^{\infty} \tilde{E}(\omega)e^{i\omega t}d\omega. \tag{2.3}$$

However, applying the definition of Eqn. 2.2 results in nonzero elements in the negative frequency domain. This is often inconvenient to handle, therefore the complex formalism in the

time domain is preferred. These drawbacks can be overcome by introducing the complex electric field as

$$\tilde{E}^+(t) = \frac{1}{2\pi} \int_0^\infty \tilde{E}(\omega)e^{i\omega t}d\omega, \tag{2.4}$$

and then the corresponding spectral field strength is

$$\tilde{E}^+(\omega) = \begin{cases} \tilde{E}(\omega) & \text{for } \omega \geq 0 \\ 0 & \text{for } \omega < 0. \end{cases} \tag{2.5}$$

The relation between $\tilde{E}^+(t)$ and $\tilde{E}^+(\omega)$ can be described by the Fourier transform, similarly as in the relation between Eqn. 2.2 and 2.3:

$$\tilde{E}^+(t) = \frac{1}{2\pi} \int_{-\infty}^\infty \tilde{E}^+(\omega)e^{i\omega t}d\omega \tag{2.6a}$$

$$\tilde{E}^+(\omega) = \int_{-\infty}^\infty \tilde{E}^+(t)e^{-i\omega t}dt. \tag{2.6b}$$

Analogously, $\tilde{E}^-(t)$ and $\tilde{E}^-(\omega)$ can also be expressed, and then the sum electric field can be written as

$$E(t) = \tilde{E}^+(t) + \tilde{E}^-(t), \tag{2.7}$$

and its complex Fourier transform is

$$\tilde{E}(\omega) = \tilde{E}^+(\omega) + \tilde{E}^-(\omega). \tag{2.8}$$

For convenience, the complex electric field $\tilde{E}^+(t)$ can be usually described by the product of a real, time-dependent amplitude function ($\mathcal{E}(t)$) and a phase term ($\Gamma(t)$):

$$E^+(t) = \mathcal{E}(t)e^{i\Gamma(t)}. \tag{2.9}$$

However, in most practical cases the spectral amplitude has distribution only around a well-determined angular frequency value with a $\Delta\omega$ spectral bandwidth. Therefore it is worth introducing the so-called central angular frequency ω_0 and the time-dependent phase $\varphi(t)$, thus $E^+(t)$ can be written as

$$E^+(t) = \mathcal{E}(t)e^{i\varphi(t)}e^{i\omega_0 t} = \frac{1}{2}\tilde{\mathcal{E}}(t)e^{i\omega_0 t}, \tag{2.10}$$

where $\tilde{\mathcal{E}}(t)$ and $\mathcal{E}(t)$ are the complex and real temporal envelopes, respectively.

2.1.2 Pulse propagation in dispersive medium

The propagation of electromagnetic radiation through an optically transparent medium can be described by solving the wave equation, derivable from the electromagnetic Maxwell equations. Here, without detailing the physical meanings of the Maxwell equations, and without the derivation of the wave equation, I simply show the final outcome of the calculations [14]. The wave equation applying Cartesian coordinates reads as follows:

$$\left(\frac{\partial^2}{\partial x^2} + \frac{\partial^2}{\partial y^2} + \frac{\partial^2}{\partial z^2} - \frac{1}{c^2}\frac{\partial^2}{\partial t^2}\right)E(x,y,z,t) = \mu_0\frac{\partial^2}{\partial t^2}P(x,y,z,t), \tag{2.11}$$

where $E(x,y,z,t)$ is the field vector, $P(x,y,z,t)$ is the response of the medium to the intense electric field, and μ_0 is the magnetic permeability of vacuum. The response of the medium, often called polarization or induced dipole moment, can be split into two components:

$$P = P_L + P_{NL} = P_L + (P_{NL}^{(2)} + P_{NL}^{(3)} + ...), \tag{2.12}$$

namely to the linear (P_L) and to the nonlinear (P_{NL}) polarizations. The linear part represents all the propagation effects that can be described by the laws of classical optics, i.e. dispersion, refraction, diffraction or interference phenomena. The nonlinear term of the induced dipole moment is responsible for the nonlinear processes, including HHG, sum- or difference frequency generation processes.

Let us now consider only the linear polarization term (P_L), or in other words, assume the linearity of the occurring optical processes [14], [15]. A linear, optically transparent, homogeneous medium can be characterized by its complex transfer function:

$$\tilde{T}(\omega) = A(\omega)e^{-i\varphi(\omega)}, \tag{2.13}$$

which makes the connection between the pulses entering ($E_{in}(\omega)$), and leaving ($E_{out}(\omega)$) the dispersive material. In Eqn. 2.13, $A(\omega)$ denotes the real amplitude transfer function, which modifies the amplitude of the passing laser pulse, while $\varphi(\omega)$ indicates the spectral phase, describing the phase shift of the linear medium, affecting all the spectral components. If we assume that there is no significant absorption during propagation, then the $A(\omega)$ amplitude transfer function can be considered constant and its effect on the pulse shape is independent from the angular frequency. Thereby the occurring pulse distortions can be merely attributed to the influences of the $\varphi(\omega)$ spectral phase. In order to make phase shift quantifiable, the spectral phase function must be expanded to Taylor series around the central angular frequency of the passing laser pulse (ω_0) [3]:

$$\varphi(\omega) \approx \varphi(\omega_0) + \sum_{n=1}^{N} \frac{1}{n!}\frac{d^n\varphi}{d\omega^n}\bigg|_{\omega=\omega_0}(\omega - \omega_0)^n. \tag{2.14}$$

In Eqn. 2.14, all derivatives, also known as dispersion coefficients, have different effects on the propagating pulse [3], [16], [17]. These are the following:

$\varphi(\omega_0) = \text{CEP}$ — This term, called carrier envelope phase (CEP), does not modify the pulse shape itself. The CEP represents the phase shift between the peak of the pulse envelope and the electric field maximum.

$\left.\dfrac{d\varphi(\omega)}{d\omega}\right|_{\omega=\omega_0} = \text{GD}$ — The group delay (GD) does not modify the pulse shape either. This term shifts the pulse in time only, without any distortion effect. In case of positive (negative) value, the pulse is shifted to positive (negative) times.

$\left.\dfrac{d^2\varphi(\omega)}{d\omega^2}\right|_{\omega=\omega_0} = \text{GDD}$ — This is the second-order dispersion or group delay dispersion (GDD). GDD modulates the envelope and introduces a chirp effect in the pulse electric field. The chirp effect is a result of different spectral components having distinct speeds in the material. Depending on its positive or negative value, we can distinguish positively or negatively chirped pulses, which is manifested in that the longer/shorter wavelength spectral components appear at the leading/trailing edge of the pulse. Furthermore, GDD stretches the laser pulse and significantly decreases its peak intensity. This moderately changes the CEP.

$\left.\dfrac{d^3\varphi(\omega)}{d\omega^3}\right|_{\omega=\omega_0} = TOD$ — This term, known as third-order dispersion (TOD), asymmetrically distorts the pulse shape. Depending on its positive or negative value, TOD causes side peaks on the trailing or leading side of the pulse with decreasing intensities, respectively. Moreover, this decreases the peak intensity and slightly shifts in time the peak of the main pulse. TOD does not modify the CEP.

$\left.\dfrac{d^4\varphi(\omega)}{d\omega^4}\right|_{\omega=\omega_0} = FOD$ — The effects of the fourth-order dispersion (FOD) is similar to the impact of GDD, so this introduces chirp, stretches the pulse, decreases its peak intensity and CEP is just slightly modified. Furthermore, FOD introduces "shoulders" in pulse evolution both at the leading and trailing edges.

In order to visualize the individual pulse-distorting effects, Figure 2.1 shows the effects on a 6 fs FWHM duration, transform-limited laser pulse (a), having π rad CEP (b), 20 fs GD (c), 40 fs^2 GDD (d), 120 fs^3 TOD (e), and 500 fs^4 FOD (f) in the spectral phase. The pulse has 800 nm central wavelength. The blue and orange curves represent the pulse envelopes and the evolutions of the electric fields, respectively.
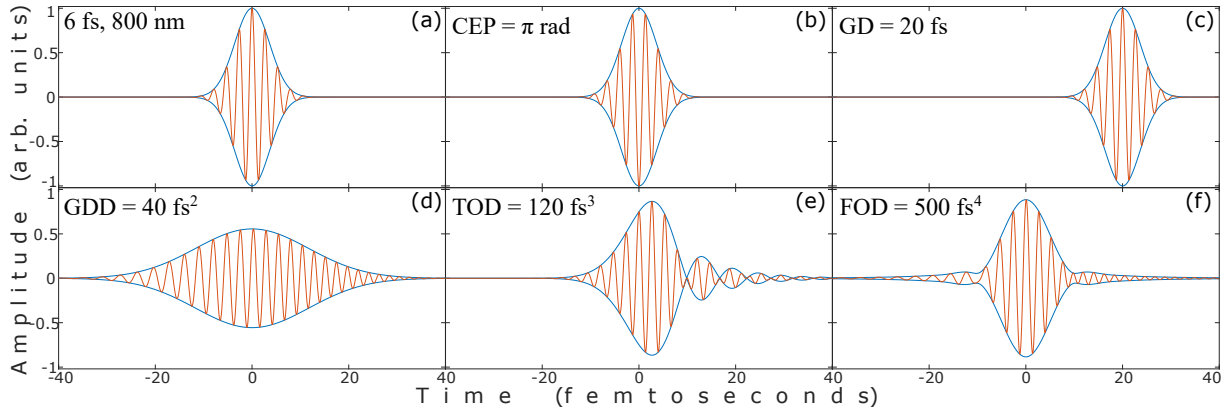
FIGURE 2.1: (a) The effect of the individual spectral phase coefficients on a 6 fs long, transform-limited laser pulse with 800 nm central wavelength. The effect of (b) π rad CEP, (c) 20 fs GD, (d) 40 fs^2 GDD, (e) 120 fs^3 TOD, and (f) 500 fs^4 FOD are presented. The blue and orange curves demonstrate the pulse envelopes and the electric fields, respectively.

2.1.3 Generation and applications of ultrashort double pulses

In general, the double-pulse (DP) or multi-peak structures are undesirable physical phenomena in laser physics, or during femtosecond pulse amplification. For instance, as it can be seen in Figure 2.1, the presence of side-peaks beside the main laser pulse often implies the presence of TOD. The appearance of these side-pulses means energy loss in the main peak, thus the residual energy in the main pulse would not be sufficient to drive ultrafast processes, including several ionization phenomena [18], [19]. Furthermore, assuming that the pre-pulse has enough energy to free electrons, and such an electric field is used to drive the gas high-order harmonic generation (GHHG) process, the overionization of the target gas might occur [20], [21], thereby impairing the investigated ultrafast phenomenon. Moreover, the presence of the DP structure in the amplification stage of the laser system deteriorates the amplification processes as either the pre- or the post-pulse gains energy too, and depletes the pump pulses. Furthermore, a sufficiently intense pre-pulse is able to saturate the gain [22], [23]; this results in the phase modulation of the main signal, which affects its propagation in the amplification medium [14], [24].

Nevertheless, there are numerous experimental applications where the utilization of double pulses are required to achieve the expected experimental outcome. For example, during HHG on solid surfaces, this kind of temporal structure is advantageous and requisite. The pre-pulse generates dense plasma on the radiated area that acts as a mirror, and becomes an active optical medium which reflects the remainder of the incident beam apart from cleaning its temporal contrast [25], [26]. It has also been proven that the conversion efficiency during the HHG process in solids can be significantly enhanced by using a femtosecond IR DP structure [27]. In addition, in ultrafast pump-probe experiments, where the aim is to somewhat alter in the investigated medium using a pump pulse, while the probe pulse is dedicated to studying

the induced effect(s), double pulses are essential and indispensable [28]–[32]. These experiments include the study of laser field controlled chemical reaction dynamics [33], in which two dominant sub-pulses with optimal frequencies and time delays are applied. Moreover, in the collinear second-harmonic generation FROG (SHG-FROG) [5] or in the SPIDER [4] pulse characterization techniques, such temporal structures are needed to reconstruct the envelope of the unknown laser pulses. Furthermore, these electric field structures are also utilized during GHHG processes, where by additionally introducing a π CEP phase shift between the two constituting pulses of the DP structure, the HHG cutoff can be dramatically extended [34]. Or, by delaying different fragments of a few-cycle laser pulse spectrum, high-order harmonics can be produced by the interference of two attosecond pulse trains [35].

For the mathematical description of a temporal DP structure, the formulas that have already been summarized in Section 2.1.1 for a single pulse can also be used. Assuming a Gaussian temporal envelope for both constituting pulses ($e^{-2ln2\frac{t^2}{\tau_p^2}}$, where τ_p is the FWHM duration of the laser pulse), and taking into account Eqn. 2.10, the total electric field of the double pulses $E_{DP}^+(t)$ can be written as

$$E_{DP}^+(t) = E_0 e^{-2ln2\frac{t^2}{\tau_p^2}} e^{i(\omega_0 t + \varphi_{CEP})} + R \cdot E_0 e^{-2ln2\frac{(t-\tau_d)^2}{\tau_p^2}} e^{i(\omega_0(t-\tau_d)+\varphi_{CEP})}. \tag{2.15}$$

In the equation above, E_0 is the amplitude, ω_0 and φ_{CEP} are the central angular frequency and the carrier envelope phase of the constituting pulses, respectively. τ_d represents the introduced time separation between the two temporal peaks, and R is the temporal amplitude ratio between them. The corresponding spectrum in the spectral domain of this unconventional electric field [2], [36] can be calculated by Fourier transformation, analogously to Eqn. 2.6b:

$$E_{DP}^+(\omega) = \mathscr{F}\{E_{DP}^+(t)\} = \int_{-\infty}^{\infty} \tilde{E}_{DP}^+(t)e^{-i\omega t}dt. \tag{2.16}$$

The electric field ($E_{DP}^+(t)$) and the corresponding spectral intensity ($|E_{DP}^+(\omega)|^2$) are represented in Figure 2.2. Figure 2.2.(a) shows the spectrum of a single, Gaussian-shape ultrashort laser pulse, having 6 fs long FWHM duration and $\omega_0 = 2.35$ PHz central angular frequency (corresponding to $\lambda_0 = 800$ nm central wavelength, solid black curve), the DP spectra by introducing a 9.3 fs (solid orange curve), and a 10.7 fs (solid green curve) temporal delay between the constituting pulses. Figures 2.2.(b) and (c) demonstrate the total electric field (orange and green curves with circles), resulting from the summation of two identical, 6 fs long laser pulses with the same, 2.35 PHz central angular frequencies (solid and dashed black curves). From these figures it becomes obvious why these two specific delay values have been chosen, as in these cases the two interfering pulses are fully destructively (b) and fully constructively (c) interfere, which can be observed in the middle of the DP structures (at ~ 5 fs). As a result, a spectral interference pattern appears in the spectral domain, which changes as the delay varies
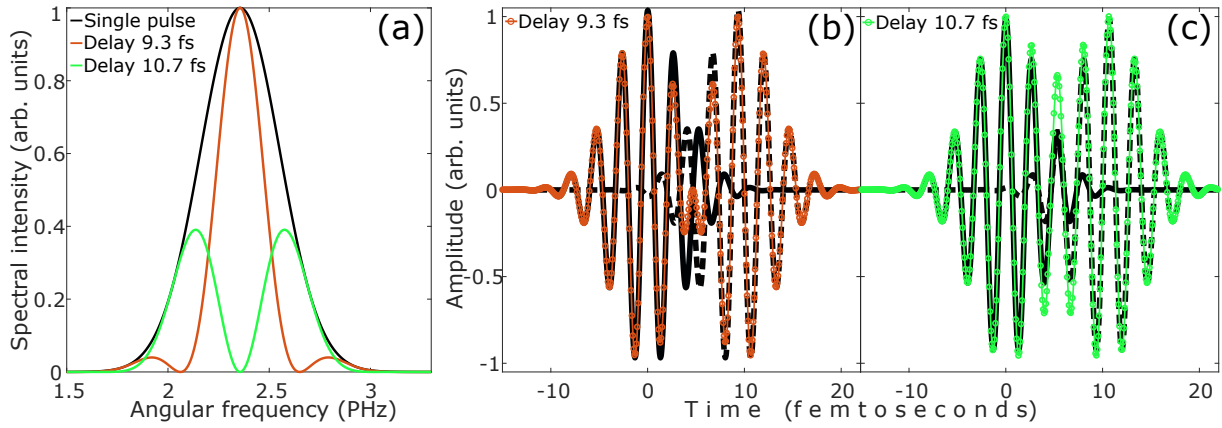
FIGURE 2.2: (a) Spectral intensities corresponding to the temporal evolutions of (b) and (c). The solid and dashed black curves in (b) and (c) show two identical 6 fs long ultrashort laser pulses with 2.35 PHz central angular frequency, and their spectrum is presented by the solid black curve in (a). The orange (b) and green (c) curves with open circles demonstrate the sum electric field of the two interfering pulses, and the corresponding spectral intensities are represented by the solid orange and green curves in (a).

[37]. The relation between the time separation (τ_d) and distance of the distinct spectral peaks in the spectral interference pattern (ω_d) can be written as $\omega_d = \frac{2\pi}{\tau_d}$ [38].

Several experimental setups have been developed to produce a DP structure in the temporal domain. One simple and easily feasible method to produce two pulses with variable delay between them is to build a Michelson- [39] or a Mach-Zehnder-type interferometer [40], containing a delay unit in one arm. The birefringent nature of optical crystals can also be utilized to split the incident pulse into two, namely the ordinary and the extraordinary ones, which encounter different refractive indices during propagation in the birefringent material [41]–[43]. Thereby a well-determined temporal delay is introduced between the ordinary and extraordinary pulses, which delay strongly depends on the material properties and the thickness of the crystal. However, these pulses are orthogonally polarized, therefore a further polarizer must be inserted into the propagation line to choose a specific polarization direction, hence the DP structure is formed. The techniques summarized above are based on the amplitude splitting of the incident laser beam, but the methods using wavefront splitting instead are also widely applied to split and later combine the incident pulses. An experimental realization of the wavefront-splitting technique is the use of reflective Dammann gratings to generate the double pulses in line [44] with reflective optics only. Wavefront-splitting can also be carried out with the previously mentioned interferometers, we only have to replace the beam splitting optics. For example, the application of a holey mirror to split the beam and later to combine them with a similar optical element is a common method [45]–[47]. Furthermore, other types of custom-made optics and optomechanics can also be used for the production of double pulses, such as the electrostatic deformable mirror based on the push-pull technology [48], the split-and-delay unit [49], or the acousto-optic programmable dispersive filter [50]–[52].

2.2 Laser pulse characterization techniques based on nonlinear optical processes

I have already mentioned in Section 2.1.2 that the temporal shape of ultrashort laser pulses significantly changes when the pulses propagate through dispersive media, thus their temporal evolution can appreciably differ from the transform-limited pulse shape. These pulse-distorting effects strongly depend on the material properties of the dispersive medium, including the refractive index [53], [54], which can also be described using the dispersion coefficients [55], [56]. The laser pulses affected by the dispersion coefficient of GDD, TOD or FOD can alter the experimental outcome, or take the expected results towards a completely different direction. Therefore, the temporal characterization of the laser pulses is sometimes unavoidable to carry out a well-controlled experiment [57]–[59]. For this reason, laser scientists have developed numerous practical techniques to be able to measure the temporal evolution of the applied laser pulses. A few of them are based on linear optical processes only, i.e. spectrally resolved interferometry (SRI) [60]. This method can determine the exact phase shift of an optically transparent dispersive material with high precision. An improvement of SRI is spectrally and spatially resolved interferometry (SSRI) [61], [62], where we can directly deduce information on the spectral phase from the shape of the phase fronts of the interfering pulses. However, these techniques are not suitable to measure the exact temporal envelopes. Accordingly, by using the SRI and SSRI techniques, the laser pulse distortions can only be specified in a relative manner, or in other words, for the complete pulse characterization one needs a laser pulse with known temporal evolution. Unfortunately, in most experimental cases such known pulse is not available, therefore the so-called self-referenced measurement must be applied, in combination with nonlinear optical processes.

To determine the absolute temporal evolution of an ultrashort laser pulse, the utilization of a nonlinear process during pulse characterization is indispensable. Nonlinear processes vary on a wide a scale. Some pulse characterization techniques, such as intensity autocorrelation [63] or SHG-FROG [5], [64], [65], are based on second-harmonic generation (SHG) [66]. This is a second-order nonlinear process that can be derived from the second-order nonlinear polarization $P_{NL}^{(2)}$ [14], already mentioned in Eqn. 2.12. An improved FROG technique is the XFROG (cross-correlation FROG) [67], which, in addition to the use of SHG, applies another second-order nonlinear process, i.e. difference frequency generation (DFG) [68] for self-referencing the unknown laser pulse. There are numerous characterization methods that apply third-order nonlinear processes: e.g. SPIDER [4], [69], which is based on sum-frequency generation (SFG) [70], or other upgraded FROG techniques, including self-diffraction FROG (SD-FROG) [64], [71], polarization-gate FROG (PG-FROG) [72]–[76], transient-grating FROG (TG-FROG) [77], [78] or third-harmonic generation FROG (THG-FROG) [79], [80]. Furthermore, another pulse

characterization method, based on a third-order nonlinear optical effect, is self-referenced spectral interferometry (SRSI) [81], [82]. The applied frequency-conserving third-order nonlinear process can be cross-polarized wave (XPW) generation [6], [83]–[85], transient-grating [86], [87] or self-diffraction [88], [89] signal production during the pulse characterization process. All third-order nonlinear processes listed above can be derived from the third-order, nonlinear, induced dipole moment ($P_{NL}^{(3)}$) [63], written in Eqn. 2.12. There are further, less widespread pulse measuring techniques, e.g. the advanced method for phase and intensity retrieval of e-fields (VAMPIRE) [90], multiphoton intrapulse interference phase scan (MIIPS) [91], the IN-SIGHT technique combined with temporal measurement at a single point of the beam [92] or the second-harmonic dispersion scan, simply d-scan [93], [94].

From the numerous experimental realizations summarized above, it becomes obvious that we have a wide range of possibilities to determine the exact temporal evolution of an unknown ultrashort laser pulse. However, it is important to mention that these measuring techniques cannot be used to determine the phase between the pulse envelope and the laser electric field maximum, namely the CEP. Measuring the CEP is out of the scope of the current research work. In the following sections, I will give a detailed description of the best-known and most widespread pulse characterization techniques used in laser physics to measure the pulse envelopes, including SPIDER [4], FROG [5] and SRSI [6].

2.2.1 SPIDER

Spectral Phase Interferometry for Direct Electric field Reconstruction (SPIDER) is a self-referenced pulse characterization method utilizing SFG and SHG processes, and realizing the experimental setup in an interferometer [4], [95]–[97]. The unknown input laser pulse is split into two equal pulses with a beamsplitter (Figure 2.3, BS1), and they propagate in the two arms of the interferometer. In one arm the pulse is further divided into two by BS2, and a τ delay is introduced between them by using a delay stage (DS). Later they are combined by another beamsplitter (BS3), thereby producing two identical replicas with a fixed delay τ between them. The other pulse, propagating in the other arm of the interferometer, is strongly chirped by using a glass slab (GS) [98], but the stretching can also be carried out with a pair of gratings [99]. At the output, the pulses coming from the two arms are focused by an achromatic lens (L) into a β-Barium borate crystal (BBO) to produce frequency-up-converted signals, such as the second-harmonic generation and sum-frequency generation signals. As the two replicas interfere with different quasi-cw slices of the chirped pulse, they are upconverted with a frequency shift with respect to each other, which results in a spectral shear $\delta\omega$. The interferogram ($S_{SPIDER}^{SFG}(\omega_c)$) that can be obtained in this way is:
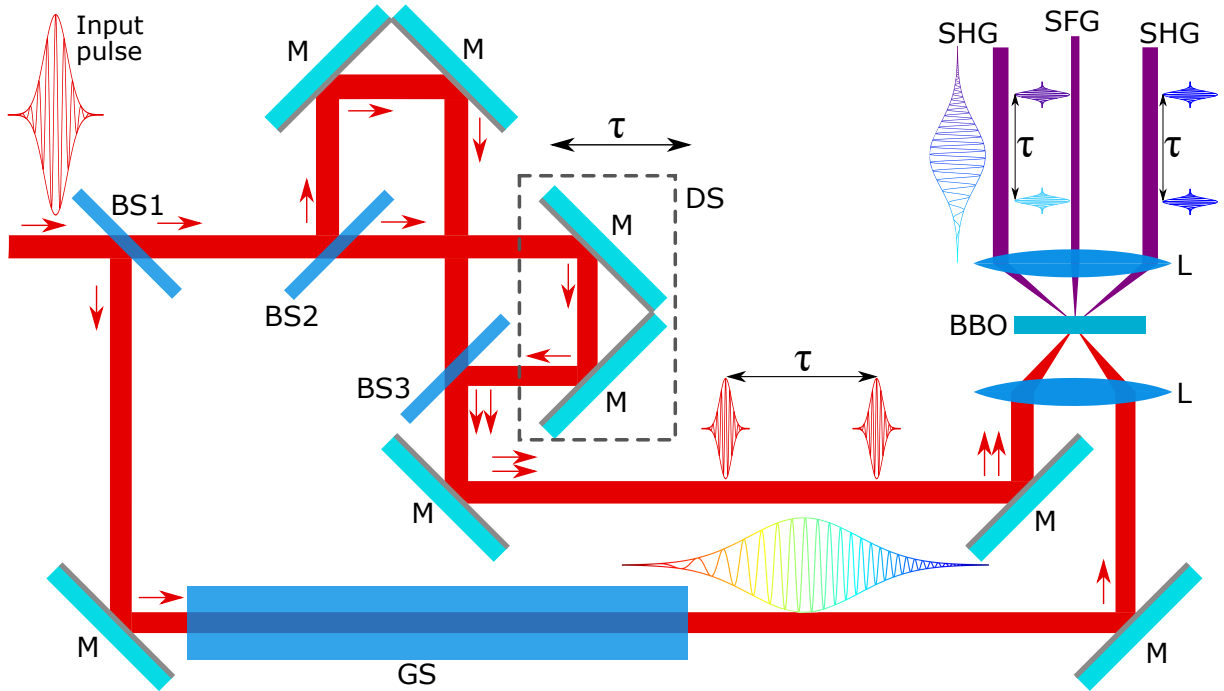
FIGURE 2.3: Schematic layout of the SPIDER pulse characterization technique. BS1, BS2, BS3 – beamsplitter, M – mirror, DS – delay stage, GS – glass slab, L – lens, BBO – β-Barium borate crystal, SHG – second-harmonic generation signal, SFG – sum-frequency generation signal, τ – delay between the two pulse replicas. The red arrows represent the propagation directions of the pulses in the interferometer arms.

$$S_{SPIDER}^{SFG}(\omega_c) = I(\omega_c) + I(\omega_c + \delta\omega) +$$
$$+2\sqrt{I(\omega_c)I(\omega_c + \delta\omega)}cos[\phi_\omega(\omega_c + \delta\omega) - \phi_\omega(\omega_c) + \omega_c\tau],$$

(2.17)

where $I(\omega)$ is the spectral intensity, $\phi_\omega(\omega_c)$ is the spectral phase, and ω_c represents the passband frequency of the detector, which is usually a spectrometer. As the first step during the evaluation, by applying two one-dimensional Fourier transforms, the spectral phase $\Delta\Phi = \phi_\omega(\omega_c + \delta\omega) - \phi_\omega(\omega_c) + \omega_c\tau$ can be extracted from the interferogram. The $\omega_c\tau$ phase term can be determined from the interferogram of the SHG signal of the two delayed identical laser pulses. This can be easily done as each pulse generates a second-harmonic signal in the nonlinear crystal, with a delay that is also τ, therefore by using again two one-dimensional Fourier transforms on their spectral interferogram, this phase term can be calculated. Thereby the unknown spectral phase is reduced to $\delta\Phi = \phi_\omega(\omega_c + \delta\omega) - \phi_\omega(\omega_c)$, but this calibration has to be carried out only once. Finally, the spectral phase $\phi_\omega(\omega)$ can be obtained at evenly spaced frequencies $\omega_i = \omega_0 + i \cdot \delta\omega$ by adding up the appropriate phase differences $\phi(\omega_n + \delta\omega) - \phi(\omega_n)$, where $n = 0, 1, ..., i - 2, i - 1$. By recording the fundamental laser spectrum independently, and by using the retrieved spectral phase, the temporal envelope of the laser pulses can be reconstructed.

2.2.2 FROG

Frequency Resolved Optical Gating (FROG) is based on the measurement of a spectrally resolved autocorrelation signal [5], [95], [97], [100]–[102]. As several methods are available to carry out autocorrelation measurements, such as SHG, PG, TG, SD or THG, a wide variety of implementations of the FROG technique is known [101]. Each method has a particular trace, but some of them are relatively similar, therefore their evaluation is also carried out in an analogous way. In the following, I will describe the firstly developed and maybe the most widely used type, the standard SHG-FROG technique, and a very similar configuration, i.e. the PG-FROG.

The SHG-FROG technique utilizes a second-harmonic generation signal to measure the temporal envelope of the unknown laser pulses. A schematic layout of the experimental setup is presented in Figure 2.4. The unknown input pulse is split into two identical pulses and they continue to propagate in the two arms of the interferometer. In one arm, a delay stage (DS) is installed so that we can adjust the temporal delay between the pulses at the output of the interferometer. Both of them are focused by the same optical element, with a lens (L), into a nonlinear optical medium, for instance, into a nonlinear BBO crystal. Depending on the temporal overlap of the two pulses, the SHG signal is generated during the propagation in the crystal. The produced signal is monitored by a spectrometer, thereby the so-called SHG-FROG
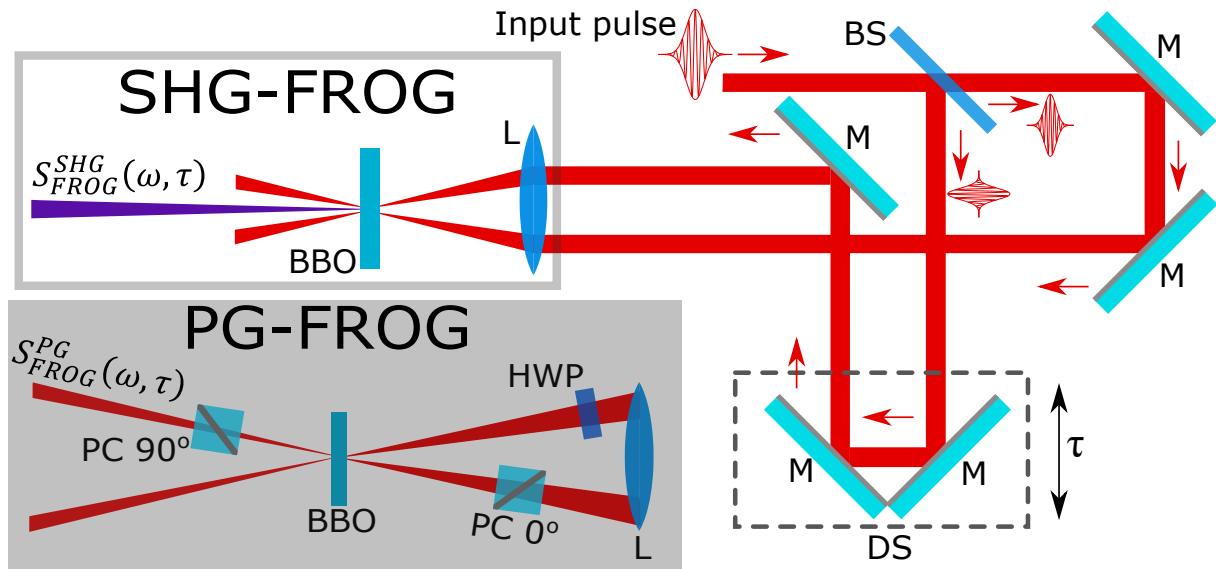

FIGURE 2.4: Schematic experimental setup of the standard SHG-FROG technique. BS – beamsplitter, M – mirror, DS – delay stage, τ – temporal delay, L – lens, BBO – β-Barium borate crystal, PC – polarization cube, HWP – half-wave plate. The arrows show the propagation directions of the pulses in the interferometer. The grey-shaded region demonstrates the experimental arrangement of the modified FROG method, PG-FROG, and the grey rectangle represents the section in SHG-FROG setup that has to be rebuilt to realize the PG-FROG. $S_{FROG}^{SHG}(\omega, \tau)$ and $S_{FROG}^{PG}(\omega, \tau)$ represent the produced interferograms.

trace ($S_{FROG}^{SHG}(\omega, \tau)$) can be recorded. The measured spectral interferogram, SHG-FROG trace [101], can be written as follows:

$$S_{FROG}^{SHG}(\omega, \tau) = \left| \int_{-\infty}^{\infty} \tilde{E}(t)\tilde{E}(t - \tau)e^{-i\omega t} \right|^2 = \left| \int_{-\infty}^{\infty} \tilde{E}(t)\tilde{g}(t - \tau)e^{-i\omega t} \right|^2, \qquad (2.18)$$

where $\tilde{E}(t)$ and $\tilde{E}(t - \tau)$ are the main and the delayed laser pulses, respectively. $\tilde{g}(t - \tau)$ can be considered as a gate pulse, which is actually the pulse to be measured itself. It is clear that the trace depends on the angular frequency ω of the measured pulses and the introduced delay τ between the two pulses. Therefore, the measured trace can be presented on a 3-dimensional graph, having ω and τ on x and y axes, and the SHG-FROG signal on the z axis. The dispersion coefficients can be retrieved from the SHG-FROG traces, so the unknown spectral phase can be reconstructed. However, information about the sign of the accumulated spectral phase cannot be extracted from such spectral interferograms.

To be able to determine, whether the dispersion coefficients positively or negatively contribute to the spectral phase, the PG-FROG measurement technique must be applied [72]–[76] (the grey rectangle in the SHG-FROG layout must be modified, as this is presented by the grey-shaded region in Figure 2.4). This setup is based on the SHG-FROG method and requires only a minor modification of the experimental setup: two polarization beamsplitter cubes (PC) need to be installed before and after the focusing optic in the propagation path of the gate pulse. These polarization cubes must be adjusted in orthogonal polarization directions (indicated as 0° and 90° degrees), therefore the gate pulse cannot go through both cubes, if linear propagation is assumed. Moreover, a further half-wave plate is inserted into the path of the measured pulse, which rotates its polarization direction by 45°, compared to the polarization state of the gate pulse. If the two pulses spatially and temporally overlap in the nonlinear crystal, they interact with each other, and as a result, the polarization direction of the gate pulse is slightly rotated, and a small portion of the reference pulse is able to go through the second PC. The modifications of the experimental setup result in a change in the recorded FROG trace too [101], [103], so accordingly, the modified interferogram can be written as

$$S_{FROG}^{PG}(\omega, \tau) = \left| \int_{-\infty}^{\infty} \tilde{E}(t)|\tilde{E}(t - \tau)|^2 e^{-i\omega t} \right|^2. \qquad (2.19)$$

Analogously to the SHG-FROG trace, the PG-FROG trace can also be presented by a 3-dimensional graph [101], having ω and τ on x and y axes, and then the colourscale represents the PG-FROG signal. By evaluating the PG-FROG traces, the complete temporal characterization of an unknown laser pulse can be performed. From these measurements, the signs of the unknown dispersion coefficients can be unambiguously determined, which is extremely important in case of ultrafast processes where information on the exact temporal evolution of the driving field is indispensable, such as in case of quantum path interference measurements

[104]–[106] or isolated attosecond pulse (IAP) generation [11], [107], [108].

2.2.3 SRSI

The denomination of the Self-Referenced Spectral Interferometry (SRSI) pulse characterization technique [6] does not follow the "animal naming trend", however, the SRSI setup is also frequently applied [109], in addition to the FROG and SPIDER methods, in femtosecond laser laboratories. SRSI can be realized in a simple and compact experimental arrangement [110], [111], presented in Figure 2.5. The reference pulse, indispensable for this characterization method, can be generated by XPW generation [84], TG [86], or SD [88] effects. Accordingly, we can distinguish the XPW-SRSI [6], TG-SRSI [87] and SD-SRSI [89] techniques, respectively. However, in my thesis I will focus on XPW-SRSI only, as this type is the most widespread, and a commercially available pulse characterization device, WIZZLER, is also based on this type.

A typical XPW-SRSI setup is demonstrated in Figure 2.5. The input pulse can be filtered spatially by an entrance iris (I), to allow us to adjust the required input energy to avoid possible damage to the optics, because this technique does not demand high energy: a pulse energy of merely around 1 pJ is sufficient in case of a typical 10 fs long pulse. The next component of the beampath is the first, reflective, Brewster incidence GaAs plate of the input polarizer (IP). After this plate, the beam is focused by a spherical mirror (SM), and is reflected by the other reflective GaAs plates of the IP, which assures the prerequisite condition of pulse characterization, i.e. the linear polarization of the laser beam (presented by the orange arrow). Ensuring
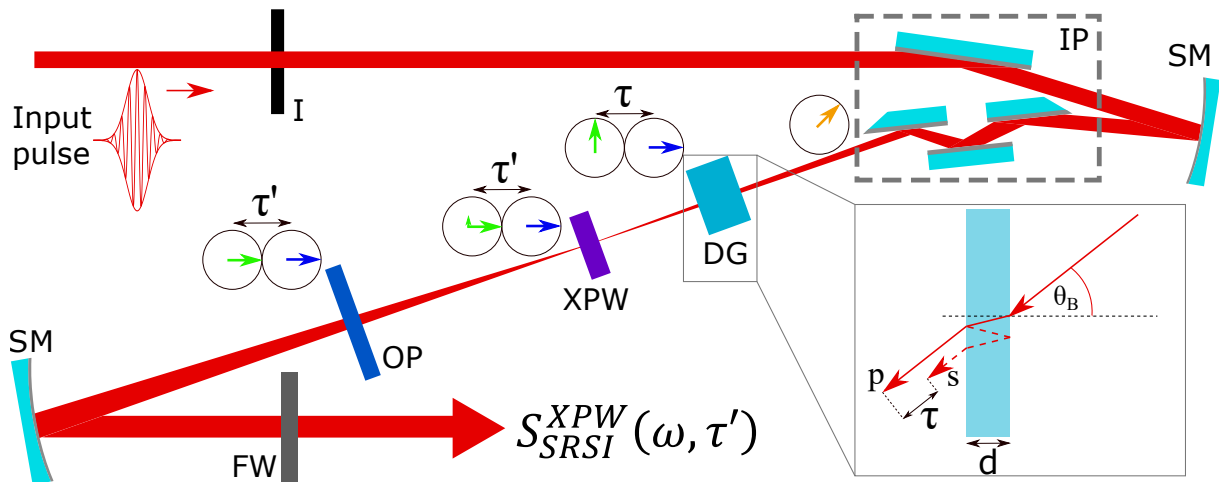

FIGURE 2.5: An experimental realization of the SRSI pulse characterization method. The main components of the setup are: I – standard iris, SM – spherical mirror, DG – delay generator, XPW – cross-polarized wave generation crystal, OP – output polarizer, FW – filter wheel. The bottom-right subfigure demonstrates the reference pulse generation process; θ_B represents the incident angle of the beam to DG, p and s mean the two distinct polarization states, τ is the introduced delay, and d is the thickness of the plate, which determines the amount of delay.

well-determined linear polarization is essential, as the applied nonlinear process in this setup is particularly sensible to the quality of the input polarization. Then, the linearly polarized pulse reaches the delay generator (DG), which is a tilted, birefringent, fused silica plate, by which two orthogonally polarized pulses are produced (perpendicular green and blue arrows next to DG). Thereby a replica pulse is generated for the characterization, which collinearly propagates with the unknown laser pulse. The production mechanism of the replica is visualized by the bottom right subfigure of Figure 2.5, from which one can observe that the replica pulse is produced by a double internal reflection in the fused silica plate, oriented at the incidence angle of θ_B, and finally a τ temporal delay is introduced between the pulses. The exact temporal delay strongly depends on the thickness and material properties of the fused silica plate. The focus of the delayed, orthogonally polarized pulses is located in the middle of a third-order nonlinear crystal. This is often a BaF_2 crystal, in which XPW is generated [83], [84], represented by the 90° rotated green arrow next to the XPW crystal. However, a small portion of the beam remains in the parallel polarization state, because the nonlinear process never reaches 100% efficiency. Besides, by propagating the two pulses through the XPW crystal, the delay is also modified slightly to τ'. After XPW generation, a second polarizer, the output polarizer (OP) is the next component of the beampath. The polarization direction is adjusted to transfer both pulses with s-polarization state. This results in two delayed pulses with the same polarization state at the output, therefore they are able to interfere with each other. Before monitoring their spectral interference ($S_{SRSI}^{XPW}(\omega, \tau')$) using a spectrometer, through the application of a continuously variable neutral density filter wheel (FW) the output energy can also be adjusted to control the energy level entering the spectrometer.

The resulting spectral interferogram of the reference ($E_{ref}(\omega)$) and the unknown laser pulse ($E(\omega)$) [6], [112], [113] can be written as

$$
\begin{aligned}
S_{SRSI}^{XPW}(\omega, \tau') &= |E_{ref}(\omega) + E(\omega)e^{i\omega\tau'}|^2 = \\
&= |E_{ref}(\omega)|^2 + |E(\omega)|^2 + f(\omega)e^{i\omega\tau'} + f^*(\omega)e^{-i\omega\tau'},
\end{aligned}
\tag{2.20}
$$

where $E_{ref}(\omega)$ and $E(\omega)$ are the spectral amplitudes of the reference and the measured pulses, respectively, and the corresponding temporal amplitudes are $E_{ref}(t)$ and $E(t)$. The term $f(\omega) = E^*(\omega)E_{ref}(\omega)$ is the interference term of the two pulses. In a first approximation, $E_{ref}(t)$ and $E(t)$ are connected to each other by the relation of

$$
E_{ref}(t) = E(t)|E(t)|^2,
\tag{2.21}
$$

which represents the XPW signal itself. From this relation, one can see that in time domain the generated XPW pulse is shorter than the generating pulse, so apart from modifying the

polarization state, this process has a slight spectral broadening effect too. Moreover, the gener-
ated XPW has a smoother spectrum and a flatter spectral phase compared to the spectrum and
spectral phase of the incident pulse, because of the temporal filtering effect of the frequency-
conserved third-order nonlinear process [114]–[116].

A simulated spectral interferogram is demonstrated by the blue curve in Figure 2.6.(a). For
the simulations, an experimentally recorded laser spectrum is utilized (orange). The yellow
curve in this figure shows the spectrum of the calculated XPW signal, using the relation of
Eqn. 2.21. From this figure, it is clear that the spectrum of the XPW signal is slightly broader
than the spectrum of the original laser pulse, proving a previous statement, namely that the
XPW generation process creates additional spectral components in the produced spectrum. In
the characterization process, it is a prerequisite that all spectral components of the XPW signal
must be more intense than the corresponding spectral components of the measured laser pulse
[113]. For the evaluation of the recorded spectral interferogram, the Fourier transform spectral
interferometry (FTSI) [117], [118] technique is utilized to extract the necessary data (the spectral
amplitude and the phase) for complete pulse reconstruction. The first step of FTSI is to inverse
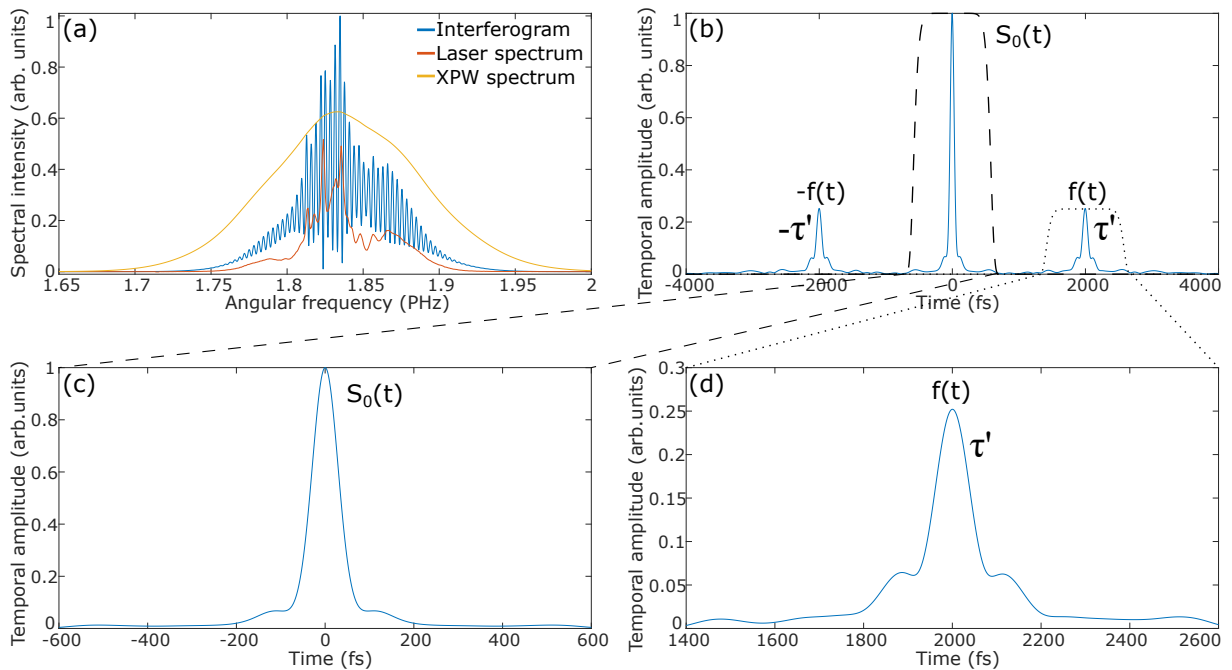

FIGURE 2.6: Steps of the FTSI method. (a) Spectrum of the input laser (orange)
and the smoother, frequency-conserving third-order nonlinear signal, the spec-
trum of the generated XPW (yellow). The blue curve represents the spectral in-
terferogram resulting from the spectral interference of the laser and the XPW
pulses. (b) By inverse Fourier transforming the spectral interferogram, the DC
term at time 0 ($S_0(t)$), and the AC terms at the delays of $-\tau'$ and τ' ($\pm f(t)$) are
obtained in time domain. The dashed grey and dotted grey curves represent the
filtering windows of the DC and the positive AC terms. (c) and (d) demonstrate
the numerically filtered $S_0(t)$ and $f(t)$ temporal peaks, respectively.

Fourier transform the spectral interferogram (blue curve in Figure 2.6.(a)); thus three well-separated peaks will be obtained in the time domain (Figure 2.6.(b)), i.e. the direct (DC) and the two alternating (AC) terms, named $S_0(t)$ and $\pm f(t)$, respectively [113]. The DC term appears at time 0, and the peaks at the positive (τ') and negative delays ($-\tau'$) are the AC terms. It is important to mention that the introduced temporal delay τ' must be sufficiently large to avoid the overlap between the distinct temporal peaks, otherwise the evaluation becomes impossible. For femtosecond pulse characterization, usually a fixed, 1 ps long delay is introduced between XPW and the measured pulses. In the simulation, the delay is 2 ps to make the distinct temporal peaks completely distinguishable. By filtering numerically the DC and the positive AC terms (indicated by the dashed and the dotted grey curves in Figure 2.6.(b)), the $S_0(t)$ and $f(t)$ terms can be obtained, as shown in Figure 2.6.(c) and (d), respectively. By transforming the filtered signals back to the frequency domain applying the Fourier theorem, the complex quantities of $\tilde{S}_0(\omega)$ and $\tilde{f}(\omega)$ can be acquired. By using these quantities, the complex spectral amplitude of both the unknown and the reference XPW pulses can be defined as

$$|\tilde{E}^+_{XPW}| = \frac{1}{2}\left(\sqrt{\tilde{S}_0(\omega) + 2|\tilde{f}(\omega)|} + \sqrt{\tilde{S}_0(\omega) - 2|\tilde{f}(\omega)|}\right), \tag{2.22a}$$

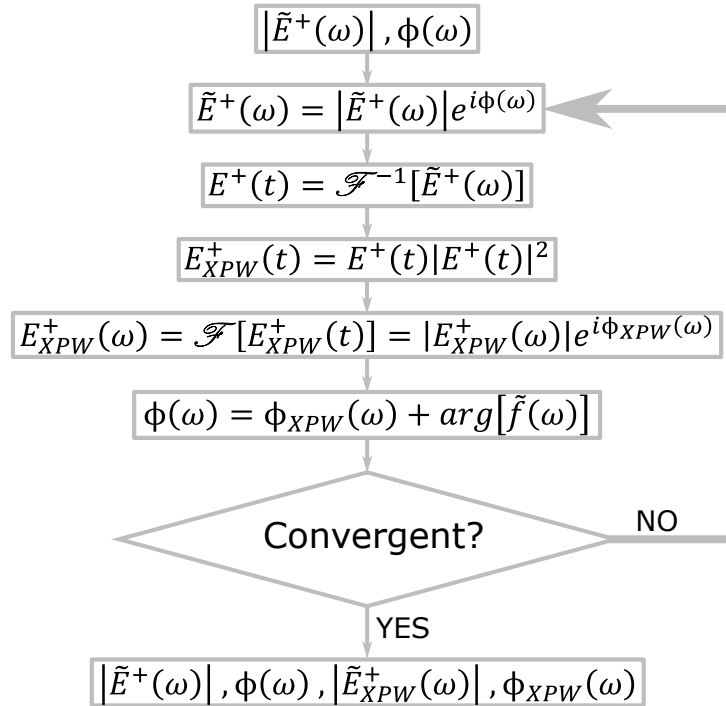$$|\tilde{E}^+(\omega)| = \frac{1}{2}\left(\sqrt{\tilde{S}_0(\omega) + 2|\tilde{f}(\omega)|} - \sqrt{\tilde{S}_0(\omega) - 2|\tilde{f}(\omega)|}\right). \tag{2.22b}$$

By performing these steps, only the spectral amplitudes can be determined (Eqn. 2.22), however, complete pulse reconstruction also requires the spectral phase. The unknown spectral phase can be retrieved separately by the so-called Gerchberg-Saxton (GS) iterative algorithm [119], [120], which utilizes the previously determined spectral amplitudes and an estimation of the spectral phase. The latter can be inferred using the argument of $\tilde{f}(\omega)$, assuming that the reference pulse spectral phase $\phi_{XPW}(\omega)$ is zero, or at least negligible compared to the spectral phase of the measured laser pulse [113]. Moreover, the phase term, caused by $GD(\omega)$, which is derived from the temporal delay τ' introduced between the two pulses, must be also considered for the preliminary assumption of the spectral phase. Therefore, the overall initial phase term is

$$\phi(\omega) = \phi_{XPW}(\omega) - arg[\tilde{f}(\omega)] - \omega\tau' \approx -(arg[\tilde{f}(\omega)] + \omega\tau'). \tag{2.23}$$

However, this phase estimation has to be further corrected by a few iteration steps of the phase retrieval algorithm. By using the initial guess of the spectral phase (Eqn. 2.23) and the previously determined spectral amplitude of the unknown pulse (Eqn. 2.22b) as the input parameters of the iterative algorithm, the following steps must be carried out to retrieve the final

spectral phase of the unknown laser pulse:

$$\left|\tilde{E}^+(\omega)\right|, \phi(\omega)$$

$$\tilde{E}^+(\omega) = \left|\tilde{E}^+(\omega)\right|e^{i\phi(\omega)}$$

$$E^+(t) = \mathscr{F}^{-1}[\tilde{E}^+(\omega)]$$

$$E^+_{XPW}(t) = E^+(t)|E^+(t)|^2$$

$$E^+_{XPW}(\omega) = \mathscr{F}[E^+_{XPW}(t)] = |E^+_{XPW}(\omega)|e^{i\phi_{XPW}(\omega)}$$

$$\phi(\omega) = \phi_{XPW}(\omega) + arg[\tilde{f}(\omega)]$$

Convergent? — NO

YES

$$\left|\tilde{E}^+(\omega)\right|, \phi(\omega), \left|\tilde{E}^+_{XPW}(\omega)\right|, \phi_{XPW}(\omega)$$

So, the first step is to simulate the spectrum of the unknown laser pulse by using the input parameters, from which the temporal evolution of the unknown pulse in a first approximation ($E^+(t)$) can be determined by applying the inverse Fourier transform on the data [113]. From $E^+(t)$, the electric field of the reference XPW pulse can be calculated by using the definition, written by Eqn. 2.21, and the determination of the corresponding spectrum of the XPW signal, utilizing the Fourier theorem, is the next step in the iterative algorithm. Then, the input spectral phase must be corrected by the phase of the XPW pulse ($\phi_{XPW}(\omega) = arg[\tilde{E}^+_{XPW}(\omega)]$). After this step, the convergence of the modified spectral phase $\phi(\omega)$ must be investigated. Simply saying, the result is convergent if the output spectral phase does not differ from the phase curve given by the former iteration loop. Nevertheless, the convergence condition of the iterative algorithm corresponds to the validity range of a given measurement [113]. If $\phi(\omega)$ does not show convergence, the iteration must be restarted from the first step of the algorithm, and all the steps must be performed once more. However, by making a few iterations, the corrected phase term will be convergent, no further loops are necessary, and the required spectral phases ($\phi(\omega)$ and $\phi_{XPW}(\omega)$) can be extracted for complete temporal characterization. The final temporal envelopes of both the laser pulse and the reference pulse can be reconstructed by using the spectral amplitudes, defined by Eqn. 2.22, and the corresponding retrieved spectral phases.

However, the iterative phase retrieval algorithm sometimes fails to reconstruct the unknown spectral phase. For example, if a few-cycle ultrashort laser pulse is strongly chirped, and besides the presence of GDD, the effect of the higher-order dispersion coefficients is also significant, the GS algorithm will not converge even after numerous iterations, as this condition

is out of its validity range [82]. Furthermore, an ultrashort laser pulse having such significant temporal distortions is unsuitable for most experimental applications. Therefore, first of all, the source of the chirp must be removed or at least decreased, then both the pulse characterization and the experiment can be carried out. Moreover, the spectral amplitude of a pulse train, consisting of ultrashort pulses, or the spectrum of a temporal DP structure has particular positions where the spectral amplitude is significantly low, or drops to zero [121]. These valleys in the spectral amplitude lead to precipitous jumps in the spectral phase, and therefore in some cases the phase is not continuous. For most pulse characterization techniques (including the standard FROG and SPIDER methods) it is challenging to reliably retrieve this discontinuous phase [122], [123]. Even the SRSI method is unable to reliably retrieve such a spectral phase. However, there exist some measuring techniques that are able to reconstruct such pulses with a significant intensity substructure. These methods include the improved ultrashort pulse retrieval algorithm for FROG [124], or the already mentioned VAMPIRE method [90]. Therefore, there is a particular demand to develop, or improve an already existing method to temporally characterize the pulses with complex intensity substructure in a reliable manner.

Although XPW-SRSI has a few limitations in pulse characterization, this self-referenced method outperforms the other techniques in many aspects [6]. For instance, the experimental arrangement of SRSI is realized in an entirely collinear geometry, which results in a compact, easily adjustable, and simple measurement setup in comparison with the already mentioned and detailed noncollinear pulse characterization techniques. Moreover, the algorithms, used in case of FROG and SPIDER to retrieve the spectral amplitude, are not straightforward [125], and concatenation along with some preliminary assumptions are required in relation to the temporal pulse shape and the spectral amplitude in case of SPIDER [126]. In SRSI, the reference pulse is self-created, and using the XPW generation process with a known spectral phase on a broader spectral bandwidth than the pulse to be characterized significantly simplifies the measurement and the phase retrieval algorithm. Furthermore, the applied nonlinear process is frequency-conserving, thereby there is no need for two distinct, or broadband spectrometers for data recording; it is sufficient to have one spectrometer with high spectral resolution. Besides, XPW-SRSI is a robust, sensitive, analytical and accurate method to temporally characterize low-dispersion, ultrashort pulses, down to few cycles, having an FWHM of 5 fs [110].

2.3 High-order harmonic generation

The shortest temporal duration of an ultrashort laser pulse with a given spectral bandwidth, as already described in Section 2.1, is the so-called Fourier-limited pulse length, which is defined by Eqn. 2.1 [13]. Without spectrally broadening the laser pulse, this can only be performed by nonlinear optical processes, as the pulse cannot be compressed temporally below

this theoretical limit. In other words, there is a physical limitation which precludes the generation of arbitrarily short pulses, i.e. a given laser pulse cannot be shorter than a single optical cycle of the given oscillating electric field [127]. The commonly used ultrafast laser sources radiate in the visible and/or in the near-IR wavelength ranges. For example, the FWHM duration of a laser pulse, having a λ_0 = 800 nm central wavelength, can be temporally compressed down to $\tau_{min} = \frac{\lambda_0}{c}$ = 2.67 fs, where c = 299792458 $\frac{m}{s}$ is the speed of light in vacuum. This specific time duration is the temporal length of a single cycle of the electric field, having this particular central wavelength, therefore the generated pulses can only have longer FWHM duration than the value of τ_{min}.

As this minimum pulse duration is directly proportional to the central wavelength, the only method to achieve shorter pulse length with a single cycle is the production of radiation in the UV spectral region. Nowadays, the most widely used experimental method to produce coherent radiation in the XUV wavelength range is the high-order harmonic generation (HHG) process [7]. HHG is extremely nonlinear, therefore such experiments require hugely intense fields (with 10^{14} $\frac{W}{cm^2}$ intensity). The primary driving sources of HHG are powerful, state-of-the-art laser systems, whose characteristics vary on a wide scale, including the central wavelength and the pulse duration of their radiation [1], [128]. For this reason, the generated high-order harmonic spectra are also diverse, as the HHG process strongly depends on the properties of the driving laser sources. In addition, the generated harmonics inherit certain properties from the driving electric field [129].

HHG can be carried out in liquids [130], in bulk semiconductor materials [131], on the surface of solids [132], or in gaseous media [133]. From these target materials the gaseous one is the most widely used, as one of the main advantages of the gaseous media over the other target materials is the continuous exchange of the medium. For example, in case of solids or bulk semiconductors, the high-energy cutoff is limited by the damage threshold of the material, while the gas atoms flow during HHG, therefore the ionized atoms are renewed continuously. For this reason, harmonics with extremely high photon energies can be generated, leading to a significantly broad XUV spectrum. The interaction of the laser electric field with a single atom, resulting in the emission of XUV radiation, can be described with the so-called semi-classical three-step model (TSM) [8], which is the basic approximation of the HHG process, and can be described by the classical Newton equations of motion. Apart from the simplicity of the model, it summarizes the main phenomena of HHG, and its results are reliable and valid in the main aspects. For the sake of a more detailed investigation, and to get a deeper insight into the processes, TDSE must be solved. However, this is a time-consuming method, even if we assume that a hydrogen-like atom is involved in the interaction. Therefore, further approximations must be introduced to simplify the interaction conditions, which are collectively called strong-field approximation (SFA) [10]. Experimental GHHG can provide a very

broad spectrum with well-defined spectral peaks, appearing at the odd multiples of the central angular frequency of the driving laser, resulting in ultrashort optical pulses in the form of attosecond pulse trains (APT) [134] or even in isolated attosecond pulses (IAP) [135]. Because of the exceptionally short pulse duration attainable with these sources, the temporal resolution in pump-probe experiments is unprecedented, thereby it provides a powerful tool for the investigation of ultrafast processes. Up to the present day, numerous arrangements have been realized in laser laboratories and research facilities for GHHG experiments [45], [136], [137] to produce XUV radiation with an extraordinarily high flux [138], to obtain unprecedented time resolution (down to 43 as [139]), or to carry out coincidence measurements at extreme high repetition rate [140]. Furthermore, handling of XUV radiation is not a trivial task, as in most materials this radiation is attenuated and absorbed, and just a few substances have acceptable reflection in this wavelength range. Therefore, to build a beamline for attosecond pulse generation, vacuum chambers are indispensable, and custom-made steering optics are required. These technical requirements can significantly raise the implementation costs of such experimental setups.

2.3.1 Semiclassical three-step model

An intuitive way to describe the HHG process through simple approximation is the so-called semiclassical three-step model [8], [141], [142]. TSM assumes an atomic potential barrier, the Coulomb potential, in which the electron (e^-) is trapped (Figure 2.7, Step 0). A prerequisite condition is that the strength of the laser electric field must be comparable with the Coulomb potential, acting on the bounded electron, otherwise the model would be out of its validity range. Because of the intense laser electric field, the potential barrier is strongly distorted, therefore the bounded electron can tunnel through the modified atomic potential with a finite probability. So the electron becomes free, and the electron's motion is defined purely by the external electric field, unaffected by the atomic potential (Step 1). The laser electric field accelerates the freed particle, and a quarter of the period later, when the direction of the field is reversed, the electron is steered back towards the ionic core (Step 2). During the motion in the continuum, the electron gains energy from the driving laser field, and there is a chance for the electron to be recombined with its parent ion. Then the accumulated excess energy is released by the emission of a high-energy XUV photon, and the atom returns to its original state (Step 3).

The driving laser electric field must be linearly polarized, otherwise the recombination probability in the third step – and therefore the emission of the XUV radiation – is significantly decreased. Taking such a linearly polarized electric field with an amplitude of A and an angular frequency of ω, the field can be written as

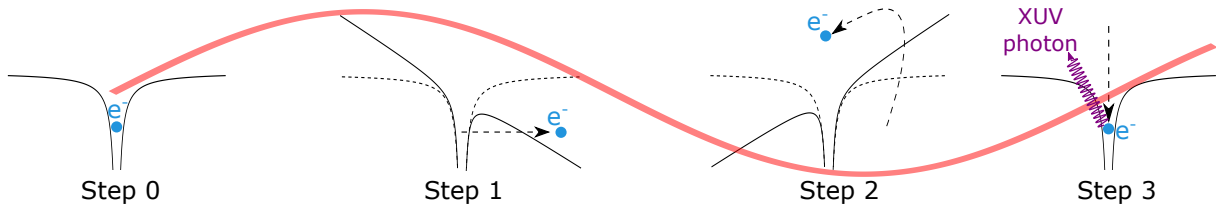$$E(t) = A\cos(\omega t + \phi), \tag{2.24}$$

FIGURE 2.7: The steps of the semiclassical TSM. Initially, the electron (e^-) is trapped by the atomic Coulomb potential (Step 0). The intense laser electric field distorts this potential and the electron can tunnel through the Coulomb barrier (Step 1). Until the sign of the laser field is reversed the freed electron is accelerated, and then the electron is driven back towards its parent ion (Step 2). Finally, the electron may recombine with the ionic core and release an energetic XUV photon (Step 3).

where ϕ is the phase of the electric field. Utilizing Newton's law of motion, having the form of $F = -eE(t) = m_e \ddot{x}(t)$, where F is the force acting on the moving electron, $x(t)$ represents the electron's spatial position during its motion, and the two dots above it indicate the second time derivative, while $-e$ and m_e are the charge and mass of the moving particle, respectively. By making merely analytical calculations [142], and assuming that the electron is ionized into the vicinity of the atomic core with zero velocity, ($x_i = x(t_i)$ and $v_i = v(t_i)$ are equal to zero at the time instant of the ionization t_i), and the position of the freed electron, driven by the laser field can be calculated as:

$$x(t) = \frac{eA}{m_e\omega^2}[cos(\omega t + \phi) - cos(\omega t_i + \phi) + \omega(t - t_i)sin(\omega t_i + \phi)]. \tag{2.25}$$

The electron appears in the continuum in the position of $x(t) = 0$, then moves and gains energy from the driving laser electric field, and finally, we can say the electron is recombined if its position becomes $x(t) = 0$ again. This is when the XUV photon is emitted. The trajectories of the liberated electrons, ionized at different time instants t_i, are presented in Figure 2.8 (top, red and blue shaded areas). The highest recombining electron energy [143] can be expressed by the equation of

$$E_{cutoff}^{TSM} = I_p + 3.17U_p, \tag{2.26}$$

where I_p is the ionization potential of the bounded electron on the outer shell in the target atom, so the driving source must overcome this binding energy to be able to ionize the atom. U_p is the ponderomotive energy that is the average electron kinetic energy driven by the oscillating electric field during the motion in the continuum, which has the form of

$$U_p = \frac{e^2A^2}{4m_e\omega^2}. \tag{2.27}$$

In Eqn. 2.26, one can observe that the cutoff energy in one part consists of I_p, however, this is a material constant and only depends on the applied target gas. Accordingly, one way to

extend this characteristic cutoff energy of the generated harmonic spectrum is the application of noble gas in the target area, for instance helium, which has higher ionization energy. Another way to reach a similar outcome is to enhance the ponderomotive energy (Eqn. 2.27). This can be performed by driving the harmonic generation process with a laser source radiating in the near- or mid-infrared wavelength region [144], since U_p is scaling with the second power of the generating field's wavelength [145]. Moreover, the E_{cutoff}^{TSM} can also be extended by increasing the field amplitude, which can be performed by tight focusing geometries, or by using high power lasers [146]. However, we must be careful with the disproportionate increase of the driving laser intensity, as undesirable effects might occur, such as overionization. This results in higher free electron density, thereby causing the self-defocusing of the propagating laser beam [147], [148], which in turn restricts harmonic emission efficiency and deteriorates the HHG process.

In the top part of Figure 2.8, the highest achievable electron energy E_{cutoff}^{TSM} is at the borderline between the reddish and bluish trajectories. These two groups of electron paths are the so-called short and long trajectories, respectively. The dashed black line represents the "core of the atom", and the two solid black curves demonstrate the movement of two electrons that
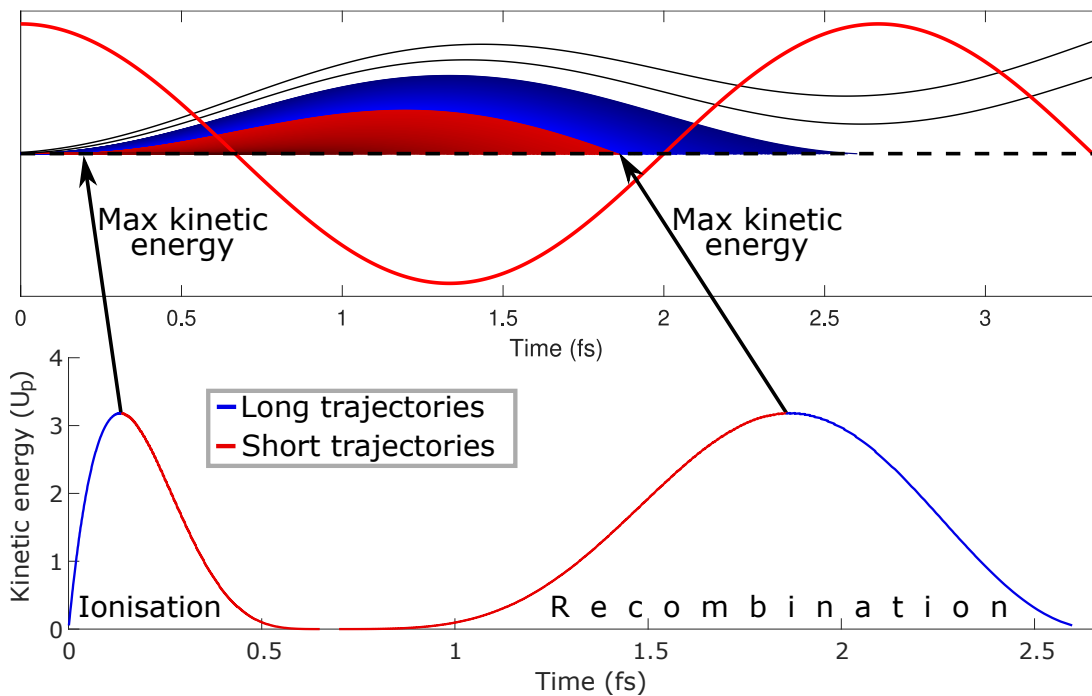
FIGURE 2.8: (top) Electron trajectories calculated by Eqn. 2.25. The reddish and bluish ranges represent the short and long trajectories, respectively. The dashed black line means the "atomic core". The two solid black curves in the top show two electron trajectories which do not lead to the recombination of the electron and the ionic core. The bright red curve demonstrates the laser electric field. (bottom) Ionization and return times of the short (red) and the long (blue) electron trajectories.

will never recombine with their parent ion. This is clear from the fact that their paths do not intersect the dashed line after their ionization time, and the laser field takes them away from the atomic core. The solid bright red curve represents the laser electric field, calculated by Eqn. 2.24, where an angular frequency of 2.36 PHz is applied in the simulation, which corresponds to a time period of τ_{min} = 2.67 fs for the electric field. The field amplitude A is adjusted to 1, while the initial phase is chosen as 0. In the bottom part of Figure 2.8 the ionization and re-combination times are presented for the short (red) and the long (blue) electron trajectories. In case of both the ionization and return times, the maximum kinetic energy is indicated ($3.17U_p$), which provides the cutoff position in the spectrum of the generated XUV radiation, and shows the electron path where the electron gains the highest kinetic energy during the motion in the continuum. These ionization processes take place in every half-cycle of the driving electric field, in the cases when the field amplitude is high enough to free the electrons [149]. In a single half-cycle of the laser electric field there is a short and a long electron path that have the same final kinetic energy, but different ionization times (Figure 2.8, bottom) [142].

The semiclassical TSM describes properly and reliably the fundamental physics of the harmonic generation process. However, the model does not take into account the quantum mechanical and the macroscopic effects, which could give a deeper insight into the phenomenon of harmonic production. Considering the quantum mechanical effects too, the theoretical description is based on the solution of TDSE by applying various approximations [10]. I will give a short overview of this model in the following section. Nevertheless, to study the propagation effects, including absorption, dispersion or the plasma generating effects during HHG, further approximations would have to be introduced [150], however, this is out of the scope of this work.

2.3.2 Strong-field approximation

As it has already been mentioned, SFA is one of the most effective ways to take into account the quantum mechanical effects during HHG. This approximation was first introduced by Lewenstein *et al.* [10], and the great advantage of this quantum model is that it is able to give a wider overview about the already discussed three steps.

The impact of an intense laser electric field on a single atom can be described by the TDSE [9], [151], [152]. For the sake of simplicity, we can take the interacting atom as hydrogen-like, and we can use atomic units for the calculations. Then the form of TDSE, applying the length gauge for the description, is

$$i\frac{\partial\psi(\mathbf{r},t)}{\partial t} = \left[-\frac{1}{2}\nabla^2 + V(\mathbf{r}) + \mathbf{r}\mathbf{E}(t)\right]\psi(\mathbf{r},t).\tag{2.28}$$

In Eqn. 2.28, $\psi(\mathbf{r}, t)$ represents the electron wave function, $V(\mathbf{r})$ means the atomic potential, and $\mathbf{E}(t)$ is the time-dependent, linearly polarized laser electric field. Parameter $\mathbf{r}$ is the position vector, and the symbol ∇ is the differential operator. In the simplest case, assuming a one-dimensional TDSE, only one preferred direction exists. However, the numerical solution of Eqn. 2.28 is time-consuming even then, and by increasing system size the approach is getting more complex. To overcome these obstacles, we must introduce the following assumptions, collectively known as strong-field approximation [9]:

i The contribution of all excited states can be neglected and only one electron takes part in the ionization process. The multiple-electron correlations are negligible.

ii During the laser-matter interaction, only the principal quantum state and the continuum state of the interacting atom is taken into account. Moreover, the electron population of the ground state cannot be depleted, and the amplitudes of the bound and continuum states are decoupled, so the bound-bound and the continuum-continuum transitions are not considered.

iii The ionized electron can move in the continuum like a free particle and only the driving laser field acts on its movement. The atomic Coulomb potential, and the influence of the other electrons do not affect the motion of the freed particle.

Applying all the three prerequisite assumptions, the time-dependent dipole moment can be expressed as

$$x(t) = i \int_{-\infty}^{t} dt' \int d^3\mathbf{p}\, d_x^*(\mathbf{p} + \mathbf{A}(t)) e^{-iS(\mathbf{p},t,t')} \mathbf{E}(t') d_x(\mathbf{p} + \mathbf{A}(t')) + c.c., \tag{2.29}$$

where d_x denotes the dipole matrix element for bound-free transitions and $\mathbf{p}$ is the canonical momentum [152]. $\mathbf{E}(t')$ is the driving laser's electric field vector, and $\mathbf{A}(t) = -\int_{-\infty}^{t} \mathbf{E}(t') dt'$ represents the associated magnetic vector potential. The notation c.c. means the complex conjugate of the preceding expression in Eqn. 2.29. Furthermore, $S(\mathbf{p}, t, t')$ is the quasiclassical action, which can be given by the following expression:

$$S(\mathbf{p}, t, t') = \int_{t'}^{t} dt'' \left(\frac{[\mathbf{p} + \mathbf{A}(t'')]^2}{2} + I_p \right). \tag{2.30}$$

The term $d(p)$ represents the atomic dipole matrix element, which takes the following form in case of a hydrogen-like interacting atom:

$$d(p) = i \left(\frac{1}{\pi\alpha} \right)^{3/4} \frac{p}{\alpha} e^{-p^2/2\alpha}, \tag{2.31}$$

where α is the fitting parameter.

By applying Fourier transform on the time-dependent dipole moment, expressed by Eqn. 2.29, the single-atom dipole spectrum $x(\omega_h)$ can be calculated as follows:

$$x(\omega_h) = \int_{-\infty}^{\infty} dt \int_{-\infty}^{t} dt' \int d^3\mathbf{p} \, d^*(\mathbf{p} + \mathbf{A}(t)) e^{\left[i\omega_h t - iS(\mathbf{p}, t, t')\right]} \mathbf{E}(t') d(\mathbf{p} + \mathbf{A}(t')) + c.c. \qquad (2.32)$$

The equation above expresses the coherent superposition of the contributions from the different quantum trajectories, occurring in distinct ionization processes. Eqn. 2.32 is called Lewenstein integral [10]. The resulting broadband dipole spectrum contains the odd multiples of the driving laser's central angular frequency, with a well-defined cutoff position at the higher energies. In case of this approximation, the cutoff law is slightly different from the prediction of TSM, written by Eqn. 2.26:

$$E_{cutoff}^{SFA} = F\left(\frac{I_p}{U_p}\right) I_p + 3.17 U_p, \qquad (2.33)$$

where the function of $F(I_p \backslash U_p)$ can vary between the values of 1.32 and 1.2 as $I_p \backslash U_p$ changes from 0 to 4. The source of the difference is the considered quantum mechanical effects. First, the electrons are not born exactly at the position $x(t) = 0$, as was assumed in case of TSM. In fact, the distance between the atomic core and the tunnel exit is a measurable length [153], therefore the electron is able to gain additional kinetic energy from the driving laser field during the tunnelling time. Furthermore, because of the diffusion mechanisms, the electron wave packets spread during their motion in the continuum, thereby this averages the obtained kinetic energy.

The numerical solution of the Lewenstein integral is feasible, which is presented by the green curve in Figure 2.9.(a). For the calculation, the driving pulse has a Gaussian-shape temporal envelope, having 6 fs FWHM duration and 800 nm central wavelength. The target gas is argon, and the pulse has $2.9 \times 10^{14} \, \frac{\text{W}}{\text{cm}^2}$ peak intensity. The fitting parameter is adjusted to $\alpha = I_p$ (see Eqn. 2.31). The cutoff energy E_{cutoff}^{SFA} is also indicated. However, to get further and deeper insight into the quantum mechanical processes, additional approximation must be introduced [154]. By investigating Eqn. 2.32, one can see a double integral over t and t', and the exponential factor, namely the phase of this complex function, expressed by the formula of $\Phi(\mathbf{p}, t, t') = \omega_h t - S(\mathbf{p}, t, t')$. Such integrals can be solved by applying the so-called saddle-point approximation (SPA) [9], [155]. The SPA method says that the single-atom dipole spectrum can be expressed by finding the saddle-points of $\Phi(\mathbf{p}, t, t')$. Mathematically it means that the solutions of the equation $\nabla\Phi(p_s, t, t') = 0$ have to be determined with respect to the ionization (t') and return times (t), and p_s is the stationary value of the canonical momentum. Then the corresponding saddle-point equations can be obtained as follows:

$$\left.\frac{\partial\Phi}{\partial t}\right|_{t_s} = \omega - \frac{[p_s - A(t_s)]^2}{2} - I_p = 0, \tag{2.34a}$$

$$\left.\frac{\partial\Phi}{\partial t'}\right|_{t'_s} = \frac{[p_s - A(t'_s)]^2}{2} + I_p = 0, \tag{2.34b}$$

$$p_s = -\frac{1}{t - t'}\int_{t'}^{t} A(t'')dt''. \tag{2.34c}$$

In Eqns. 2.34, t'_s and t_s can be considered as the stationary ionization and the recombination time instants, respectively, and p_s denotes the stationary momentum. By utilizing the above saddle-point equations, the dipole spectrum takes the mathematical form of

$$x(\omega_h) = \sum_s \frac{i2\pi}{\sqrt{det(S'')}}\left[\frac{\pi}{\epsilon + i(t_s - t'_s)/2}\right]^{\frac{3}{2}} E(t'_s)d_x^*[p_s - A(t_s)]d_x[p_s - A(t'_s)]e^{i\Phi(p_s,t_s,t'_s)}, \tag{2.35}$$
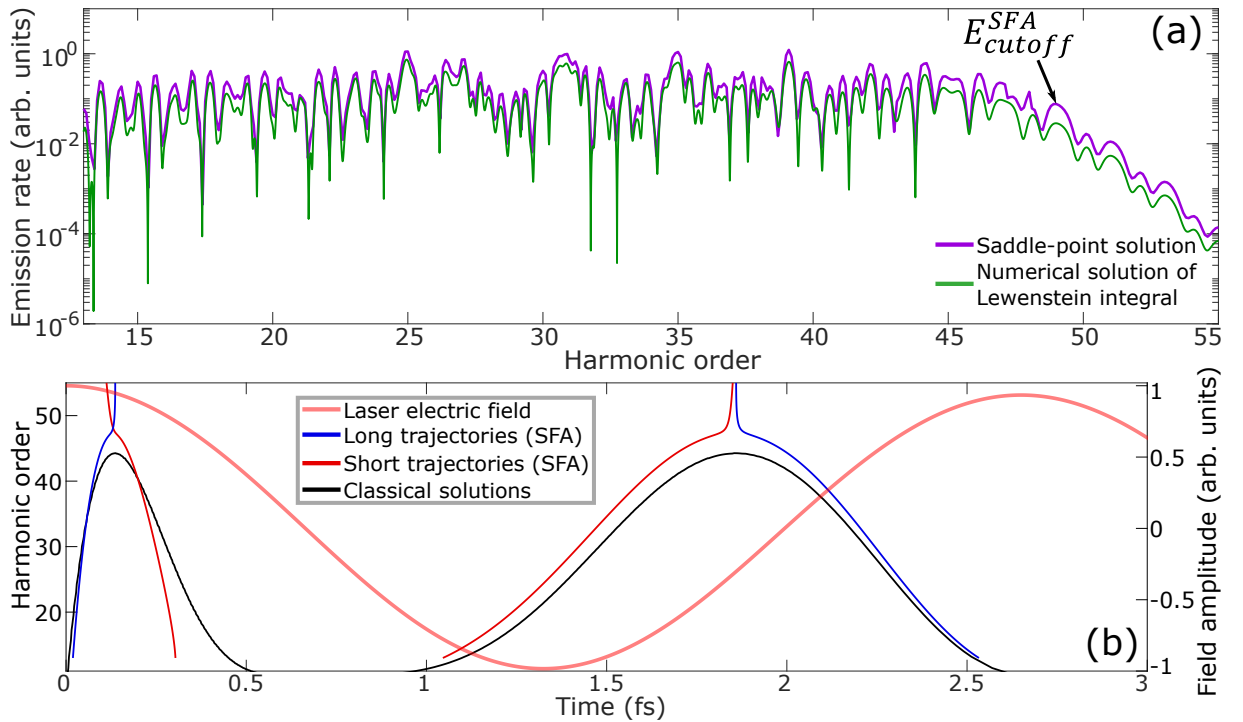
FIGURE 2.9: (a) Harmonic dipole spectra obtained from the numerical solution of the Lewenstein integral (green), and from the calculation of the saddle-points of Eqn. 2.32 (purple). The driving pulse is a 6 fs long, Gaussian-shape pulse with 800 nm central wavelength. The pulse has $2.9 \times 10^{14} \frac{W}{cm^2}$ intensity, and the target gas is argon. The cutoff position E_{cutoff}^{SFA} is marked. The fitting parameter is $\alpha = I_p$. (b) The ionization and the return times with respect to the harmonic energy in case of the short (red) and the long (blue) trajectories, obtained by the saddle-point solutions. The black curves demonstrate the classical ionization and return times, and the bright red curve represents the laser electric field.

where ϵ denotes an arbitrary small positive regularization constant, which is introduced to dispose of the singularity. The term of $det(S'')$ is the determinant of a 2×2 Hessian matrix including the second-order partial derivatives of $\Phi(p_s, t, t')$, evaluated in correspondence with the saddle-points:

$$det(S'') = det(\Phi'') = \left[\frac{\partial^2 S}{\partial t \partial t'}\right]^2 - \frac{\partial^2 S}{\partial t^2}\frac{\partial^2 S}{\partial t'^2}. \tag{2.36}$$

One series of the saddle-point solutions p_s, t_s, t'_s unambiguously determines a given value of photon energy $E_h = \hbar\omega_h$, where $\hbar$ is the reduced Planck constant ($\hbar = 6.582 \times 10^{-16}$ eV·s), and ω_h is the central angular frequency of the high-order harmonic. In simpler terms, its physical interpretation is that the photons with energy E_h are emitted by the electrons which are ionized at time instant t'_s, and have acquired a momentum p_s from the electric field, and finally, recombined with their parent ion at the recombination time instant t_s. The ionization and return times with respect to the harmonic order, similarly as in the bottom part of Figure 2.8, are presented in Figure 2.9.(b). The short and the long trajectories, given by the SFA model, are presented by the red and the blue curves, respectively. The solid black curves represent the corresponding ionization and recombination times obtained by the TSM. Comparing the results given by the TSM with those of the SFA, the difference in the cutoff position is revealed, which has been already predicted by Eqn. 2.33. The bright red curve represents the laser pulse electric field. In Figure 2.9.(b), only the highest amplitude half-cycle of the driving laser electric field is chosen for the demonstration, however, these ionization and recombination processes take place in every half-cycle of the laser pulse. By taking into account all contributions of the electron trajectories given by the saddle-points, the resulting HHG spectrum is presented by the purple curve in Figure 2.9.(a). The parameters, used during the calculations, are the same as in the numerical solution of the Lewenstein integral. One can observe that both the numerical solution of Eqn. 2.32 and the calculation of its saddle-points lead almost to the same outcome. The main spectral characteristics of the HHG dipole spectra are the same in both cases. However, the determination of the saddle-points has a great advantage over the numerical solution of Eqn. 2.32: by using SPA, a trajectory analysis can be performed, which is advantageous, for example, for the investigation of quantum path interferences [156], or for the study of the HHG process, by considering only the short or the long quantum paths [157]. Furthermore, determining the series of all saddle-point solutions is time-consuming, especially in case of multi-cycle driving pulses, where numerous quantum paths are generated. Therefore, the significantly quicker numerical solution of the Lewenstein integral (Eqn. 2.32) is more advantageous for the study of HHG in case of long driving pulses and for the investigation of the net spectral properties of the dipole spectrum.

2.3.3 Production of attosecond pulses and their applications

The generation of coherent XUV radiation does not necessarily mean the production of attosecond pulses. To make sure of that, the generated radiation must be temporally characterized. The laser pulse characterization techniques described in Section 2.2 cannot be used to temporally investigate the produced XUV, as all these methods are based on nonlinear processes that utilize nonlinear crystals to produce the reference pulse for characterization. Unfortunately, extreme ultraviolet radiation is absorbed in such crystals, therefore this is not a viable option. However, in the early 2000s, a pulse characterization technique called Reconstruction of Attosecond harmonic Beating By Interference of Two-photon Transitions (RABBITT) was developed, which is able to measure the temporal evolution of attosecond pulse trains [158], [159].

Basically, RABBITT is a pump-probe experiment, where the pump beam is XUV, while the probe beam is the fundamental field [160]. The XUV and the delayed IR pulses are focused into a high-density gas target, where electrons are liberated from the atoms. The harmonics directly ionize the target gas, while the delayed IR, having pulses with peak intensities varying from 10^{11} $\frac{W}{cm^2}$ to 10^{13} $\frac{W}{cm^2}$, are merely able to ionize the gas through multi-photon ionization. By recording the photoelectron spectrum, sharp peaks are visible, which correspond to the absorption of high-order harmonics. Because of the delayed IR, additional peaks appear at the positions of the even harmonics, which are called sidebands. These further peaks are the result of two-photon ionization processes, i.e. they are born by the up-conversion of the first lower harmonic signal, and the down-conversion of the neighbouring higher harmonic peak caused by the absorption or emission of one IR photon. By changing the delay between the pump and probe pulses, 2ω frequency oscillation can be observed in the sideband signals, and this contains information about the phases of the neighbouring harmonics [161]. By extracting the phase information from the sidebands, and using the photon spectrum of HHG, the temporal evolution of XUV radiation can be reconstructed.

The availability of attosecond pulses paves the way for the investigation of ultrafast processes that take place faster than a femtosecond. The applications of attosecond pulses are widespread, including XUV coherent tomography [162], transient absorption spectroscopy [163] or studying the ultrafast motion of electrons and holes after light-matter interactions [164]. Moreover, an outstandingly powerful tool to investigate processes on the attosecond time scale is the reaction microscope [165]. This is a complex measurement device dedicated to record ionized particles in coincidence after the attosecond pulses and/or the laser field ionize the target medium, from which a momentum map can be reconstructed. A similar experimental tool is the velocity map imaging experimental end-station, which is able to determine the phase variation of electronic wave packets in momentum space for the reconstruction of the

wave functions of atoms and molecules [166]. Last but not least, the so-called NanoESCA experimental tool is able to look into the electronic structure of surfaces and condensed phase matter by utilizing the XUV radiation [167]. Thanks to this device, a high resolution photoemission electron microscope is available for the study of magnetic materials [168]. Moreover, it allows for the investigation of the momentum distribution of photoelectrons released from a small area of the sample surface [169].

All in all, the range of the experimental applications of APTs and IAPs are almost endless. However, the different experimental campaigns usually require attosecond pulses with variable temporal and spectral characteristics. Therefore, the ability to control these properties of XUV sources is beneficial in an attosecond pulse generating beamline. In conclusion, APTs and IAPs have become the most powerful tools in attosecond science to study the ultrafast dynamics of electronic wave packets and investigate phenomena taking place in few hundreds of attoseconds.

Chapter 3

Results

In Chapter 2, I gave a detailed overview of scientific areas that are necessary to understand the aim and motivation of my research work. One can easily see that the characterization of double- and multi-peak laser pulses is highly important, as they appear in many areas of scientific applications [26], [27], [34], [35]. However, the measurement of their temporal evolution is challenging [123], and there are only a small number of laser pulse characterization techniques which are able to reconstruct such unconventional laser pulses [90]. Furthermore, the GHHG experiments are widespread and are under continuous development. This field of science is one of the most commonly used methods to investigate ultrafast dynamics and processes that take place on the attosecond time scale [162]–[169].

In the following sections, I will describe the main results of my work, which will expand the range of possibilities of ultrashort laser pulse characterization techniques for the measurement of femtosecond DP structures [T1]. Moreover, I will summarize the results of the theoretical investigation into the impact of double pulses on the generated high harmonic dipole spectra [T2]. Finally, I will demonstrate the experimental validation of the theoretically observed spectral variation effects in the produced high-order harmonics [T3]. The experimental campaign was performed using a high-repetition-rate attosecond pulse generation beamline at the Extreme Light Infrastructure - Attosecond Light Pulse Sources (ELI ALPS) Research Facility [O1].

3.1 Production and characterization of double pulses

In this section I will focus on the main improvements of a femtosecond pulse characterization technique, namely the SRSI phase retrieval algorithm. With the developed modification, the method is able to extract the spectral phase with edgy and precipitous jumps, associated with the DP structure [T1]. First, I will describe the modifications introduced in the spectral phase retrieval algorithm of the already existing method. Then, I will demonstrate a procedure for the experimental production of double pulses for further investigations. Finally, after

the first successful software examinations, I will present the experimental validation of the improved phase retrieval algorithm, and compare it with the outcome of the original algorithm.

3.1.1 Introduction of the phase correction term in the spectral phase retrieval algorithm

As it has already been described in Section 2.2.3, the original algorithm of SRSI utilizes a numerically calculated spectral amplitude (Eqn. 2.22b), and an estimated initial spectral phase (Eqn. 2.23) as input parameters of the GS iterative phase retrieval algorithm. Then, the initial guess for the phase is corrected after a few iterations, and the impact of higher-order dispersion coefficients on laser pulse shape can be determined, without any information about CEP. However, in case of DP characterization, the iterative phase retrieval algorithm cannot accurately retrieve the unknown spectral phase. The reason behind this is that the low amplitude positions in the spectrum (see Figure 2.2) lead to discontinuities in the spectral phase, which is challenging to retrieve in this unconventional case. A prerequisite of a valid measurement with SRSI is that the spectral components of the XPW signal must be more intense than the corresponding components of the unknown laser pulse, and this has to be true for all spectral components, presented in Figure 3.1.(a). In this figure, the orange curve shows a simulated spectrum of a DP structure, consisting of two identical pulses with a Gaussian-shape temporal envelope, having 5 fs FWHM duration, and a 30 fs long temporal delay between them. Both pulses have 800 nm central wavelength in the spectral domain, and a flat zero spectral phase is chosen (see Eqn. 2.15). The yellow curve represents the corresponding XPW spectral intensity, calculated by Fourier transforming the formula of Eqn. 2.21. The blue curve demonstrates the spectral interferogram, produced by the interference of the signals, shown by the orange and yellow curves. By evaluating the spectral interferogram, the spectral amplitude of both the XPW pulse and the unknown laser pulse can be reconstructed (see Eqn. 2.22). However, the interferogram contains further information, required for the complete characterization of double pulses, which is not yet extracted.

By defining a more compact formula than the expression of Eqn. 2.20, the spectral interferogram can be expressed as

$$\tilde{S}(\omega) = \tilde{S}_0(\omega) + \tilde{f}(\omega)e^{i\omega\tau_d} + c.c., \tag{3.1}$$

where $\tilde{S}_0(\omega)$ and $\tilde{f}(\omega)$ are the DC and AC terms of the spectral interferogram, respectively, and τ_d represents the temporal separation between the constituting pulses of the DP structure. Because of double pulses, the inverse Fourier transform of the recorded spectral interferogram results in nine peaks in time domain, as Figure 3.1.(b) demonstrates. One can remember that in case of single pulse characterization, three peaks were obtained, as this can be seen in Figure

2.6.(b). Accordingly, the DC and AC terms in the temporal interferogram have a substructure because of the DP structure, and in this case the direct and alternating components can be written as

$$\tilde{S}_0(t) = \sum_{k=0,+,-} S_k(t) \tag{3.2a}$$

$$\tilde{f}(t) = \sum_{k=0,+,-} f_k(t) + c.c. \tag{3.2b}$$

From Figure 3.1.(a) (and from Eqn. 3.2.(a) and (b)) we can derive important information: besides the spectral modulation caused by the interference of the XPW and measured pulses, there is a further lower-period modulation in the spectral interferogram, produced by the double pulses. This additional feature is closely related to the temporal separation and temporal amplitude ratio of the constituting pulses of the characterized DP structure. This information can be extracted by analyzing the temporal interferogram, by following the steps presented in Figure 3.1(b)-(c). First, for energy conservation during evaluation, the positive and negative AC terms must be shifted to the temporal position of the DC term, where the amount of the exact temporal shift τ' can be determined by the FTSI method. τ' is the delay introduced by the delay generator and the XPW crystal (see Section 2.2.3). Then, we obtain the modified temporal
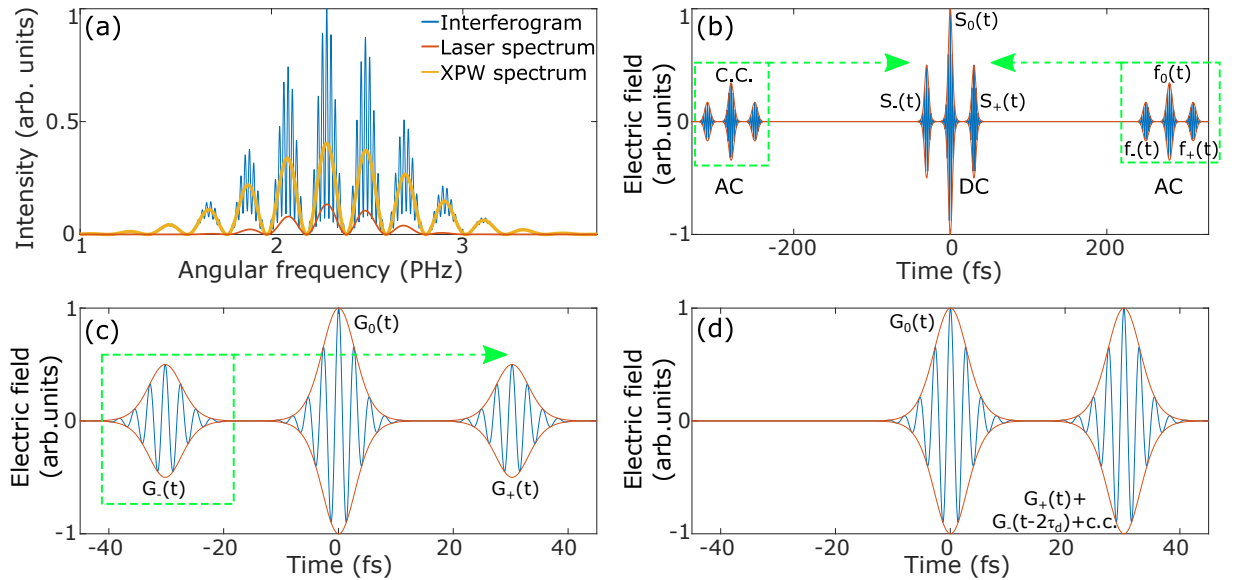
FIGURE 3.1: (a) Laser spectrum (orange), XPW pulse spectrum (yellow), and their interference, the spectral interferogram (blue). (b) Temporal interferogram and step 1 to retrieve the time separation and amplitude ratio of the unknown double pulses: shift the AC terms to overlap with the DC term and sum them. (c) Step 2: move the $G_-(t)$ peak to overlap with $G_+(t)$ and sum them. (d) Given modified temporal interferogram from which further information can be extracted for complete DP reconstruction.

interferogram, which is shown in Figure 3.1.(c), and has the mathematical form of

$$G_k(t) = S_k(t) + f_k(t + \tau') + c.c., \tag{3.3}$$

where index k can be $0, +, -$. As a next step, the peak $G_-(t)$ must be moved in time to the temporal position of $G_+(t)$ and summed, where the temporal shift $2\tau_d$ can be calculated again by the FTSI method (Figure 3.1.(d)). τ_d represents the temporal separation between the constituting pulses of the DP structure. In fact, τ_d can be extracted only from the investigation of the DC or AC terms, but for the determination of the amplitude ratio this step is indispensable. The term $G_0(t)$ remains unchanged. By applying these steps, the temporal interferogram is modified which leads to the following relation:

$$S_{mod}(t) = G_0(t) + G_+(t) + G_-(t - 2\tau_d). \tag{3.4}$$

By making Fourier transform on $S_{mod}(t)$, and taking its argument, we can extract a phase term, without the impact of higher-order dispersion coefficients, but with information about the amplitude ratio and temporal delay of the unknown double pulses. This phase term is referred to as φ_{corr}. The spectral phase resulting from the higher-order dispersion terms (φ_{disp}) is determined by a polynomial fit to the outcome of the original phase retrieval algorithm (φ_{iter}). The final spectral phase for complete pulse reconstruction is $\varphi_{calc} = \varphi_{disp} + \varphi_{corr}$.

As a comparison, the different spectral phase terms are presented in Figure 3.2, by defining the temporal amplitude ratio as (a) 0.2, (b) 0.7, and (c) 1 between the constituting pulses of the DP structure (see Eqn. 2.15). In these figures the blue curves represent the simulated spectra of the double pulses, while the yellow curves show the corresponding simulated spectral phases (φ_{expd}). The outcomes of the iterative phase retrieval algorithm (φ_{iter}) are shown by the dashed red curves in Figure 3.2 for each case, which gives correct result only when the amplitude ratio is low ($R = 0.2$). The phase correction terms (φ_{corr}) are represented by the solid green curves in Figure 3.2. The final, combined spectral phases are indicated by the solid black curves (φ_{calc}) which shows the most accurate result for the highest temporal amplitude ratio ($R = 1$). However, in case of the lowest one ($R = 0.2$), the modified phase still provides an acceptable outcome when compared to the expected spectral phase (φ_{expd}).

As a conclusion, the introduced phase correction term during pulse reconstruction significantly improves the accuracy of the retrieved spectral phase in case of the characterization of double pulses, especially by increasing the temporal amplitude ratio. Furthermore, the correction term slightly spoils the outcome of the original algorithm, but the ability to reconstruct more common and simpler laser pulse envelopes is still possible, which statement will be proven later in Section 3.1.5.
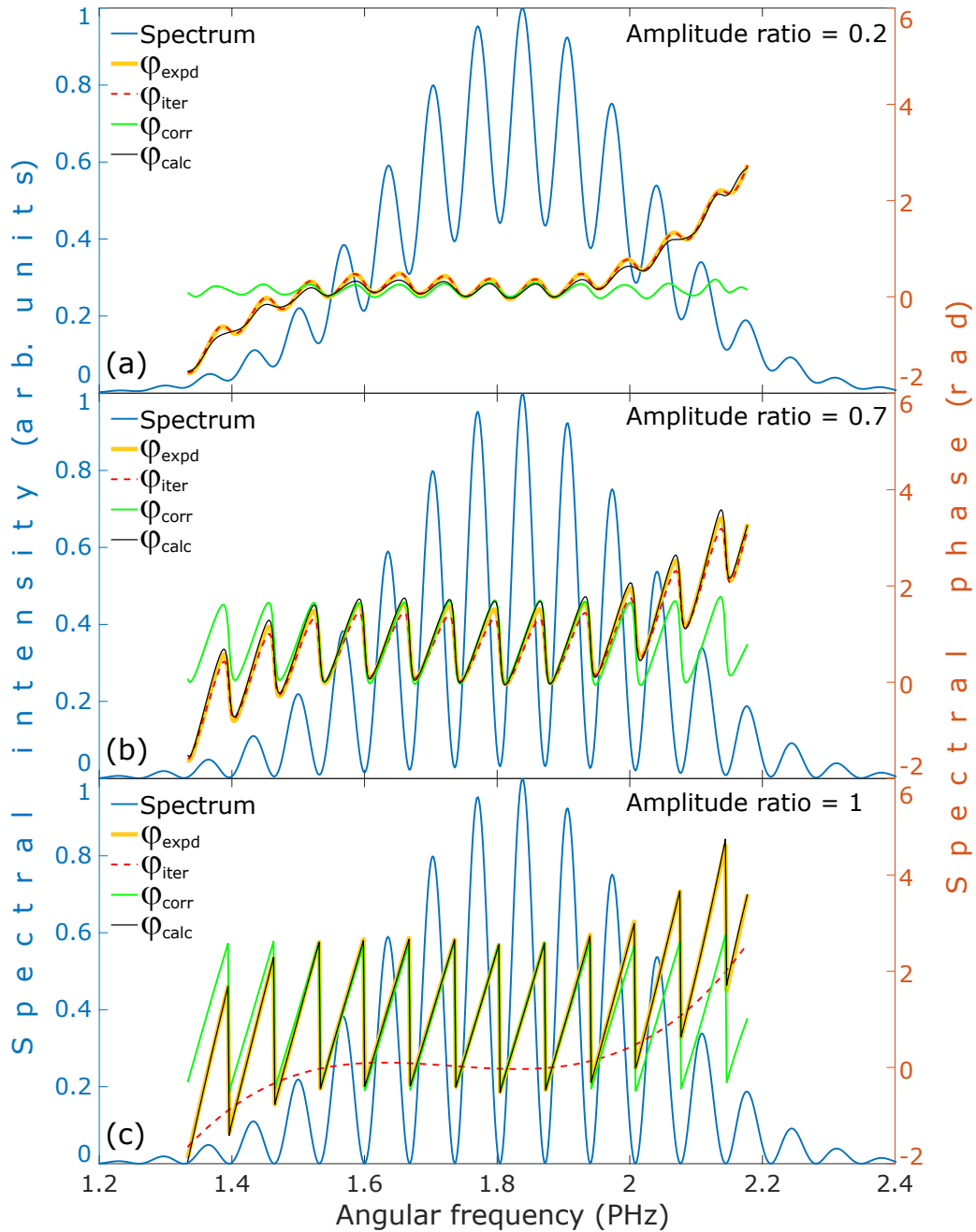
FIGURE 3.2: Simulated spectra (blue) and spectral phases (yellow) of DP structures. The outcomes of the iterative algorithm (φ_{iter}), the phase correction terms (φ_{corr}) and the final spectral phases (φ_{calc}) are presented by the dashed red, solid green and solid black curves, respectively, in case of (a) 0.2, (b) 0.7, and (c) 1 amplitude ratio R (see Eqn. 2.15).

3.1.2 Validation of the improved method by simulations

Before experimental validation, I tested the improved method by simulations. I chose two special cases that could be useful case studies for these theoretical investigations: (I) In the case where the two constituting pulses of the DP structure partially overlap in time domain, therefore their interaction produces both temporal and spectral interference. (II) In the other

case, I tested the improved technique by two strongly chirped femtosecond pulses, having much longer time separation between them than the FWHM duration of the initial single pulse. In both cases the constituting peaks have a Gaussian envelope with 37 fs long FWHM temporal length. Moreover, their central wavelength is 800 nm, which corresponds to 2.35 PHz central angular frequency. These simulation parameters were chosen so the theoretical results would correspond to the subsequent experimental investigations.

In case (I), a pulse-duration-comparable time separation, more exactly, a 45 fs long temporal delay is introduced between the two constituting pulses of the DP structure. There is no added spectral phase with higher-order dispersion coefficients, and the temporal amplitude ratio R between the two peaks is adjusted to 1. The resulting temporal envelope of the DP structure is presented by the solid blue curve in Figure 3.3.(b), while the corresponding spectral intensity and phase are shown by the black curve with open circles and the solid blue curve in Figure 3.3.(a), respectively. The spectral phase, retrieved by the original algorithm by disregarding the proposed phase correction term, is demonstrated by the green squares in Figure 3.3.(a). The corresponding reconstructed temporal intensity is presented by the green squares in Figure 3.3.(b), by using the green squares as the spectral phase, and the black curve with open circles as the spectral amplitude for pulse reconstruction. Analogously, the spectral phase and the reconstructed pulse envelope obtained by the improved technique are shown by the orange curve with open circles and the orange curve with dots in Figure 3.3.(a) and (b), respectively. One can clearly observe a much better match with the expected result by using the improved method instead of utilizing only the outcome of the original algorithm.
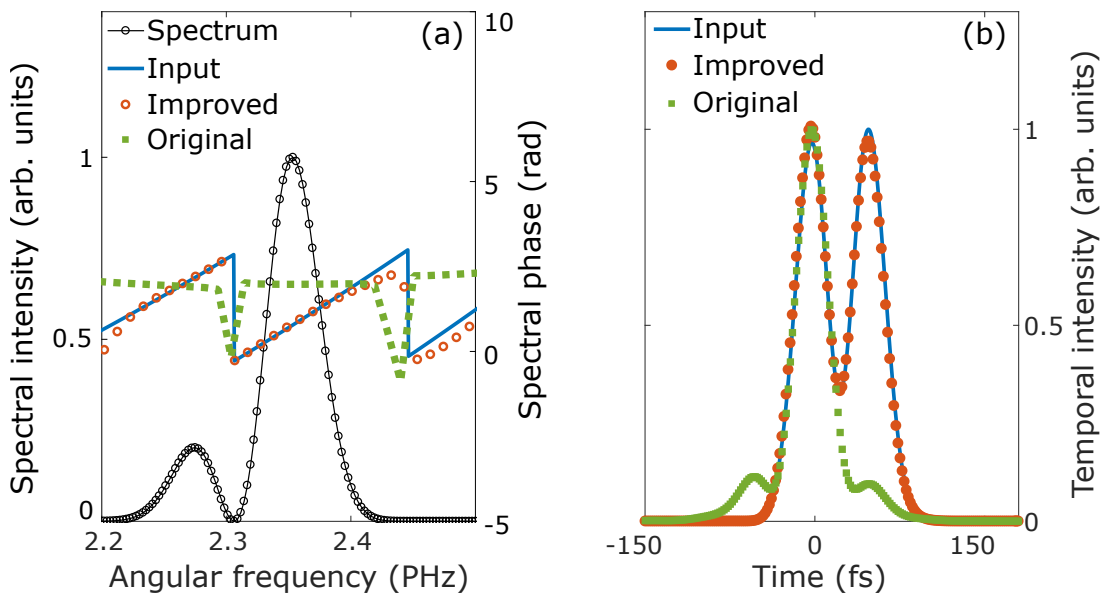
FIGURE 3.3: (a) Spectrum (black curve with open circles) and spectral phases of double pulses: expected (solid blue), and retrieved spectral phase curves by utilizing the original (green squares) and the improved method (orange open circles). (b) Corresponding temporal intensities: simulated double pulses (solid blue), reconstructed pulse envelopes by using the original (green squares), and the improved technique (orange dots).

During the second simulation test, in case (II), the temporal separation was set to be 268 fs between the constituting peaks of the double pulses, and to simulate the spectral phase, 300 fs^2 GDD and 60000 fs^3 TOD were applied. The other simulation parameters were the same as in case (I). Similarly as in Figure 3.3, Figure 3.4.(a) represents the spectral domain, and Figure 3.4.(b) shows the temporal domain results. Accordingly, the simulated DP spectrum and spectral phase are presented by the black curve with open circles and the solid blue curve in Figure 3.4.(a), respectively. The corresponding envelope of the DP structure is the solid blue curve in Figure 3.4.(b). The outcome of the phase retrieval, and the result of the reconstruction by using the original (green squares) and the improved method (orange circles) are demonstrated by Figure 3.4.(a) and (b), respectively. One can see that a DP structure having longer time delay and strongly chirped constituting pulses can still be reconstructed by applying the proposed method. It is important to mention that the chosen amplitude ratio is 1 in case (II) as well, but the pulses in Figure 3.4.(b) show some deviation in the peak intensity. This is due to the side peaks of the first constituting pulse, produced by TOD, interfering destructively with the other pulse of the DP structure. In fact, there are slight differences between the expected (solid blue) and reconstructed pulse envelopes (orange dots). However, by comparing the results to the outcome of the original algorithm, the accuracy of reconstruction is significantly improved. The time delay in these simulations are comparable to the experimental conditions (see the
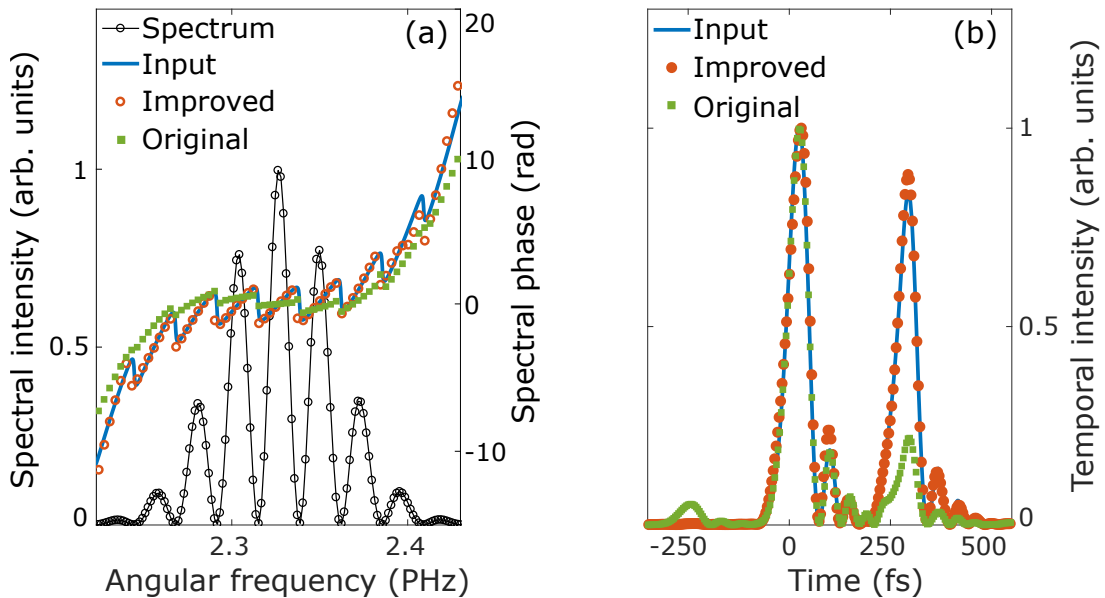
FIGURE 3.4: (a) The spectral intensity (black curve with open circles) and spectral phase of the simulated DP structure (solid blue), considering as the expected spectral phase. The phases, retrieved by the original (green squares) and the improved methods (orange open circles), are also presented. (b) Temporal intensity substructures, showing the expected pulse shape (solid blue), and the result of pulse reconstruction by the original (green squares) and the improved techniques (orange dots).

following two sections).

3.1.3   Experimental production of temporal double-pulse structure

There exist a few experimental arrangements for
the production of temporal double pulses, as it has
been already mentioned in Section 2.1.3. For the pur-
pose of this study, we used the birefringence-based
method to produce two pulses with a well-determined
temporal delay for experimental testing of the im-
proved phase retrieval algorithm. Figure 3.5 represents
the schematic arrangement used for the production of
the DP structure. To assure linear polarization, the in-
coming beam goes through a broadband polarizer (P1)
which transmits only one polarization direction from

FIGURE 3.5: Schematic layout for the ex-
perimental generation of double pulses to
validate the improved pulse reconstruc-
tion method.

the presumably unpolarized beam. The actual polarization states are shown by the arrows
in the bottom part of Figure 3.5. With this we are confident that a linearly polarized beam
is available. The next component of the beampath is a birefringent β-Barium borate (BBO)
crystal, which splits the incoming beam into ordinary (*o*, green) and extraordinary (*eo*, blue)
components, and τ_d temporal delay is introduced between them (τ_d strongly depends on the
thickness and the material properties of the applied nonlinear crystal). After the BBO, we need
a second broadband polarizer (P2) which transmits the two beams with the same polarization
state. Therefore after the beams pass through P2, the DP structure is formed.

By rotating the BBO or P2 around the propagation axis of the beam, the temporal amplitude
ratio of the pulses can be varied. Since the polarization state of the input beam is determined by
P1, by rotating the BBO the crystal optical axis is rotated, therefore the splitting ratio between
o and *eo* beams is changing. One can achieve a similar outcome by the rotation of P2, while
keeping the BBO crystal in a fixed rotational position. In addition, by rotating the birefringent
crystal around a perpendicular axis to the propagation direction, the effective optical path of
the two beams changes, thereby the delay can also be varied slightly between the pulses.

3.1.4   Inspection of the improved pulse characterization method under experimen-
tal conditions

As described in the previous section, the DP structure is experimentally produced by ap-
plying the sequence of a broadband polarizer (P1), a nonlinear BBO crystal, and another broad-
band polarizer (P2) for testing the improved spectral phase retrieval algorithm. In the experi-
mental setup (Figure 3.6) a ~ 700 μm thick BBO crystal is used, which introduces an approxi-
mately 268 fs delay between the *o* and *eo* pulses. The spectrum of the experimentally generated
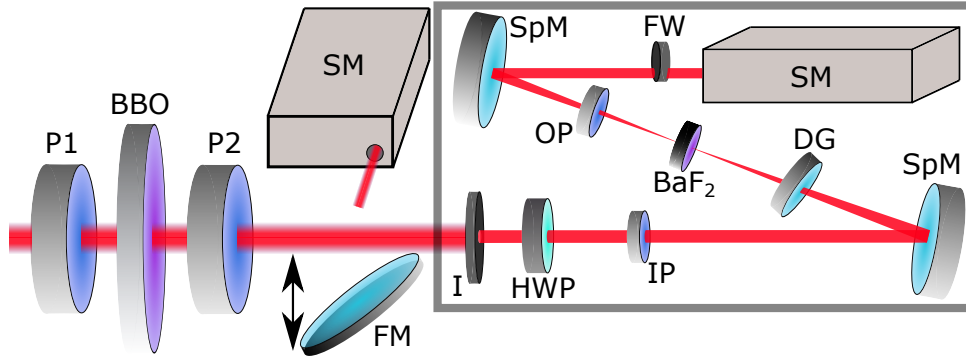
FIGURE 3.6: Experimental arrangement for testing the improved spectral phase retrieval algorithm: P1, P2 – polarizers, BBO – β-Barium borate crystal, FM – flip-mirror, SM – visible-IR spectrometer. Grey rectangle represents the WIZZLER pulse characterization device: I – input iris, HWP – half-wave plate, IP and OP – input and output polarizers, SpM – spherical mirrors, DG – delay generator, BaF_2 crystal for XPW generation, FW – filter wheel.

DP structure can be monitored by inserting a flip-mirror (FM) into the beam path, which steers the pulses towards a visible-IR spectrometer (SM). Thereby we can record the spectral intensity, from which the spectral amplitude can be determined for pulse reconstruction. Validation of the improved phase retrieval algorithm is performed by using commercially available pulse characterization equipment, called as WIZZLER (Fastlite Ultrafast Scientific Instrumentation). The WIZZLER's schematic layout is represented by the grey rectangle in Figure 3.6. The WIZZLER device consists of almost the same optical elements as the schematic representation of SRSI in Figure 2.5. In the applied experimental setup, a BaF_2 crystal is utilized to generate the reference XPW, and a broadband spectrometer (SM) is used to record the produced spectral interferograms. Moreover, a half-wave plate (HWP) can be inserted before the input polarizer (IP) for the possible rotation of the input polarization axis, as XPW signal generation is particularly sensitive to the driving polarization direction. The other optical components are the same as in Figure 2.5. The experimental setup was built in the TEWATI laser laboratory of the Department of Optics and Quantum Electronics at the University of Szeged.

I recorded spectral interferograms from an arbitrary 0° to 90° rotational angles of the BBO crystal with 5° step size, adjusted by a manually rotatable optical mount. The angle-dependent temporal amplitude ratio of the constituting pulses of the DP structure can be calculated by the proportion of the temporal amplitudes of the produced ordinary ($A_o = A \cdot cos^2\alpha$) and the extraordinary ($A_{eo} = A \cdot sin^2\alpha$) pulses:

$$R = \frac{A_{eo}}{A_o} = \frac{A \cdot sin^2\alpha}{A \cdot cos^2\alpha} = tan^2\alpha. \tag{3.5}$$

In the equation above, α represents the angle between the optical axis of BBO and the polarization direction of the input single pulse. The measured temporal amplitude ratio between
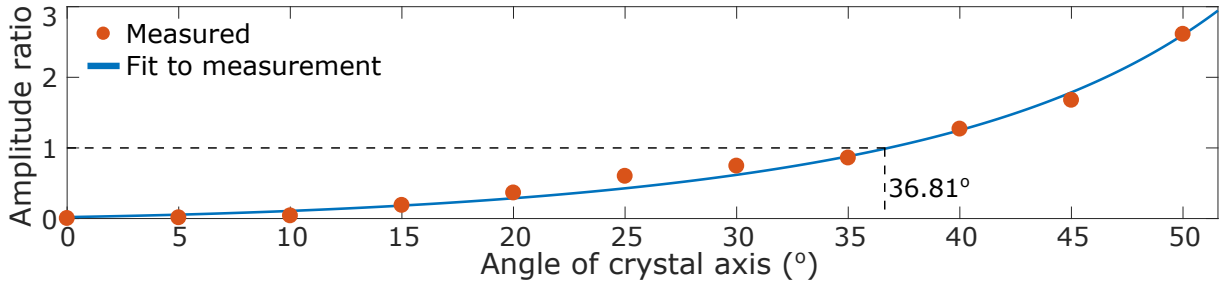
FIGURE 3.7: The measured temporal amplitude ratios of the reconstructed dou-
ble pulses by applying the improved pulse reconstruction method (orange dots).
The blue curve is a $tan^2(\alpha + \delta)$ fit to the measured data for calibrating the rotation
angle of the BBO crystal. The value 36.81° shows the angle where the pulses are
generated with equal amplitudes.

the two produced pulses as a function of rotational angle are demonstrated by the orange dots
in Figure 3.7. These ratios are obtained by reconstructing the double pulses, utilizing the im-
proved pulse characterization technique. The solid blue curve demonstrates a $tan^2(\alpha + \delta)$ fit to
the measured data, from which the rotational angle of the nonlinear BBO crystal can be cali-
brated. The constant δ is used for taking into account the rotation angle offset. By using the
calibration curve, the equal amplitude ratio can be determined, reached at the crystal angle
of 36.81°. It is important to note that the ordinary and extraordinary pulses cannot be distin-
guished by this method, so the maximum amplitude ratio is 1 during these measurements. The
values above this in Figure 3.7 are the reciprocal of the corresponding ratios.

Figure 3.8.(a) and (b) present the results of the reconstruction of the experimentally pro-
duced double pulses created at the 35° nominal rotational angle of the BBO crystal. In Figure
3.8.(a), the dark and light blue curves are the spectrum and spectral phase of the single pulse
(SP), respectively, obtained by the WIZZLER device. The black curve with open circles shows
the experimentally recorded DP spectrum, while the green squares and orange dots represent
the spectral phase evolution retrieved by the original and the improved technique, respectively.
The corresponding reconstructed pulse envelopes are in Figure 3.8.(b); the solid blue curve is
the temporal shape of the SP, the green squares is obtained by the WIZZLER and the orange
dotted curve is the outcome of the improved pulse reconstruction method. For the sake of
comparison, the simulation results can be seen in Figure 3.8.(c) and (d). In the experiment, the
single pulse has a Gaussian-shape temporal envelope, having approximately 37 fs long FWHM
duration at a central wavelength of around 800 nm. Consequently, these parameters are used
to get the simulation results (and this is the reason why these parameters are applied for the
calculations summarized in Section 3.1.2). Moreover, the delay introduced between the con-
stituting pulses is 268 fs, and their amplitude ratio is chosen as 0.9 (both values are defined
by the experimental parameters). The calculation results are shown by the solid blue curve
in Figure 3.8.(d), and the corresponding spectral intensity and phase are the black curve with
open circles, and the solid blue curve in Figure 3.8.(c), respectively. The outcome of the original
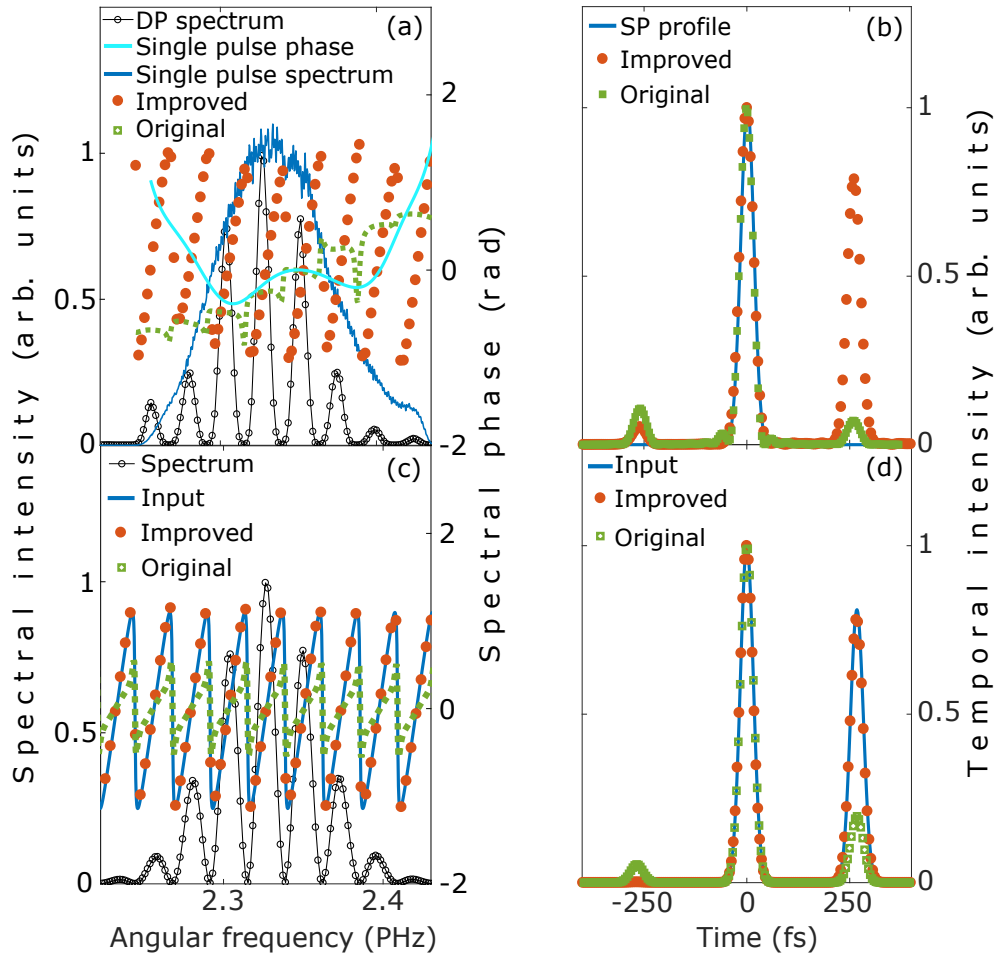
FIGURE 3.8: (a) Single pulse spectrum (dark blue) and spectral phase (light blue) obtained by the WIZZLER device. The black curve with open circles is the measured spectral intensity of the DP structure. The green squares and orange dots represent the phases retrieved by the original and the improved technique, respectively. (b) Reconstructed SP (solid blue) and DP temporal intensities (green squares and orange dots) calculated by the corresponding spectrum and spectral phase. (c) Spectrum of the simulated DP structure (black curve with open circles), spectral phase (solid blue), its retrieval by the improved (orange dots) and the original (green squares) method. (d) Simulated DP shape (solid blue) and the result of reconstruction obtained by the improved (orange dots) and the original (green squares) technique.

and the improved methods, by retrieving the simulated spectral phase (solid blue), is demonstrated by the green squares and orange dots in Figure 3.8.(c), respectively. The corresponding reconstructed temporal envelopes are in Figure 3.8.(d).

One can clearly observe both in the simulated and the experimentally obtained values that the improved technique provides more accurate results than the original algorithm when reconstructing double pulses. The original method retrieves correctly the temporal delay, however, it inaccurately determines the amplitude ratio, thereby the final pulse reconstruction is imprecise. At the same time, the improved algorithm retrieves properly both the delay and the temporal amplitude ratio, so it gives accurate results for the reconstruction of a DP structure,

while maintaining the ability to reconstruct the SP shape, as in this case the proposed phase correction term is merely a constant zero flat phase, since φ_{corr} smoothens out as the amplitude ratio decreases (see Figure 3.2).

3.1.5 Comparing the results of the original and the improved pulse reconstruction techniques

I dedicate this section to comparing the results obtained by the original and the improved pulse reconstruction methods. The deviation of the retrieved phase ($\varphi_{ret}(\omega)$) from the expected one ($\varphi_{expd}(\omega)$) is calculated in both cases by applying the following expression:

$$DEV = (\omega_2 - \omega_1)^{-1} \int_{\omega_1}^{\omega_2} |\varphi_{ret}(\omega) - \varphi_{expd}(\omega)| d\omega. \tag{3.6}$$

In the equation above, ω_1 and ω_2 represent the limits of the angular frequency region where the two phase curves are compared to each other. The expected phase curve for this analysis is defined by applying 20 fs^2 GDD and 300 fs^3 TOD. In these simulations, the duration of a single pulse is 6.2 fs, and its central angular frequency is 1030 nm. The resulting deviations are demonstrated in Figure 3.9 by choosing different amplitude ratios between the pulses. The blue curve with circles shows the deviation of the initial phase estimation (Eqn. 2.23), being
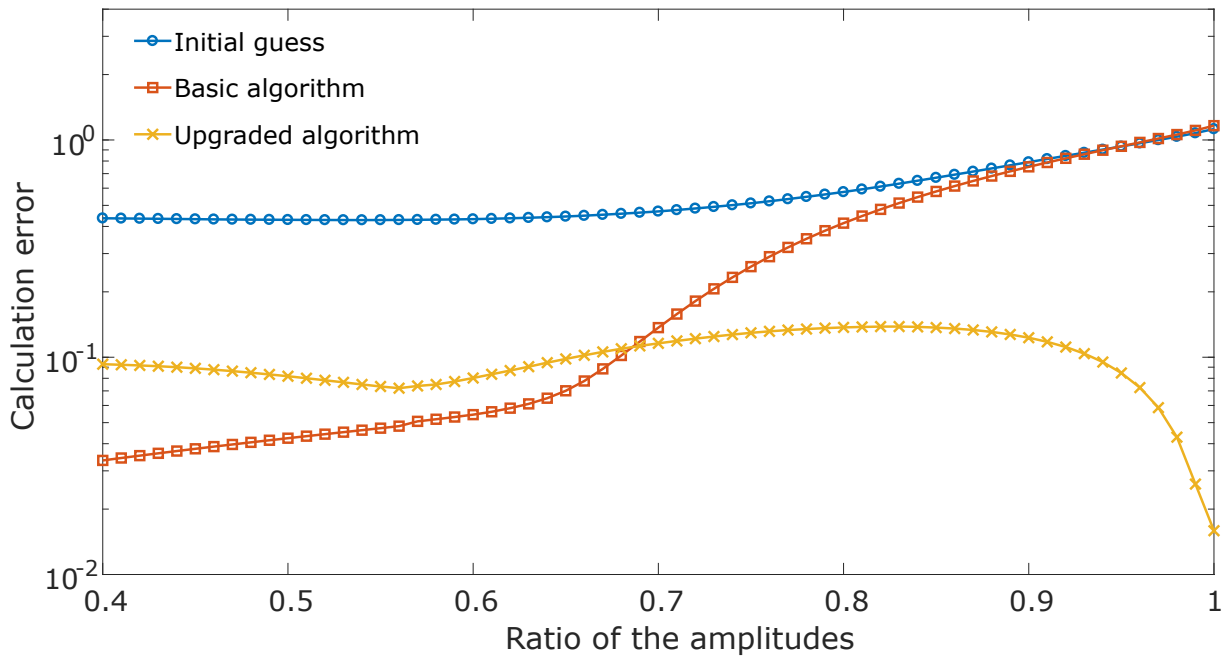
FIGURE 3.9: Deviations from the expected result at different amplitude ratios in the DP structure. The discrepancy of the input spectral phase of the iterative algorithm from the expected one is shown by the blue curve with circles. The deviations of the original and the improved methods from the expected spectral phase is presented by the red curve with squares and the yellow curve with crosses, respectively. The expected phase for this analysis is defined by introducing 20 fs^2 GDD and 300 fs^3 TOD. The pulse duration is 6.2 fs around 1030 nm central angular frequency.

the input phase of the phase retrieval algorithm. One can unambiguously see that this shows a huge error, exceeding 30% deviation along the whole investigated range, and the discrepancy grows with increasing amplitude ratios. After a few iterations, the original algorithm modifies the initial guess, and gives a small error (less than 0.8% deviation from the expected spectral phase) up to the amplitude ratio of ~ 0.65 (red curve with squares). When the amplitude ratio of 0.65 is exceeded, the accuracy of the original method deteriorates, and above the ratio of 0.8 the original algorithm does not substantially modify the initially estimated spectral phase. In contrast, the improved phase retrieval method obtains the best outcome at higher amplitude ratios, so in this region the proposed modifications unambiguously improve phase retrieval (yellow curve with crosses). In addition, by investigating the lower amplitude ratio region (below 0.7), the error of the improved technique is still acceptable, being almost constant and lower than 1%. Unfortunately, the phase correction term slightly spoils the accuracy at lower amplitude ratios, but the outcome of the improved method is still close to the precision of the original method.

All in all, the proposed spectral phase retrieval method greatly improves the accuracy of the final outcome of DP reconstruction, therefore the list of laser pulse characterization techniques that are able to offer reliable results for the reconstruction of the DP structure is extended.

Summary I. *I have improved an already existing femtosecond laser pulse characterization technique, called SRSI to be able to reconstruct femtosecond double-pulse structures. I have shown that by manipulating the temporal interferogram, a spectral phase correction term can be extracted. The combination of this phase correction term and the originally retrieved spectral phase gives an improved final phase for complete pulse reconstruction. I verified the improved method by simulations, and I successfully reconstructed the temporal shape of experimentally produced double pulses. I determined the deviations of the retrieved spectral phases, obtained both by the original and the improved methods, from the expected spectral phase, and by this I quantitatively demonstrated the level of improvement of the technique on a wide range of amplitude ratios of double pulses* [T1].

Legal notes:

3.2 Spectral features of high-order harmonics generated by double pulses

The main aspects of the high-order harmonic generation process have already been described in Section 2.3. As mentioned in that section, for harmonic generation the target material can be various, but I will focus my investigations only on harmonic generation in gaseous material. During the GHHG processes, it is a well-known property that the produced harmonics inherit certain properties from the driving light source, including the coherence and certain spectral characteristics of the driving laser. Therefore, it is a promising approach to introduce spectral modifications in the driving source, and as a result some spectral properties of the produced high-order harmonics can be changed. I propose to manipulate the driving laser spectrum by the interference of two ultrashort pulses, having pulse-duration-comparable temporal delay between them. Due to the short time delay, the temporal interference pattern can also be observed besides the spectral interference effect. While temporal overlap provides an unconventional electric field, for example a super-Gaussian like temporal envelope at certain delays, the interference in the spectral domain modifies the laser spectrum. By varying the time separation between the constituting pulses of the DP structure, the spectral interference can also be altered, therefore electric fields with various temporal and spectral shapes can be produced to drive the HHG process.

The proposed method is thoroughly investigated by single-atom model simulations [T2], and the theoretically observed spectral variation effects are verified under experimental conditions [T3], [O1]. In the following sections, I will summarize the main results of the study of HHG driven by temporal double pulses in gaseous material [T2]. Firstly, laser pulse spectra will be investigated to visualize the introduced modifications both in the driving spectrum and in the laser electric field. Then, the impact of double pulses on the HHG process will be demonstrated, where the dipole spectra are obtained by the numerical solution of the Lewenstein integral. Finally, the observed changes in DP-driven harmonic spectra, namely harmonic photon energy tuning and the alteration of their spectral bandwidth effects, will be shown.

3.2.1 Modulation of the spectral characteristics of laser sources

I have already mentioned that the required spectral modifications in the laser spectrum can be introduced by interfering two femtosecond laser pulses, having pulse-duration-comparable temporal delay between them. For this reason, I dedicate this section to demonstrating how the spectral characteristics of laser radiation are modulated by varying the delay between the constituting pulses of a DP structure. The technique, and its effects are analyzed both using theoretical calculations [T2] and carrying out an experimental campaign [T3], but in addition, I will present an alternative method to achieve the same outcome.

Firstly, I investigate the spectral variations of the laser spectrum caused by the interference of two identical pulses and modified by the variable delay between them. A representative example can be seen in Figure 3.10. The initial single pulse has 12 fs long FWHM duration and 2.36 PHz central angular frequency (corresponding to 800 nm central wavelength). There is no added spectral phase with higher-order dispersion. The spectrum of the single pulse is presented by the blue curve in Figure 3.10.(a), while the corresponding electric field is in Figure 3.10.(b). The notation of 0 fs in the legend means there is no delay between the two interfering pulses, thus they constructively interfere with each other. The amplitude ratio of the two peaks is chosen as R=1 (Eqn. 2.15). If one of the pulses is simply shifted by 13.3 fs, the resulting temporal evolution of the electric field changes, as shown by Figure 3.10.(c). The two pulses constructively interfere at this delay position, similarly as in Figure 2.2.(c). Accordingly, because of spectral interference, the spectrum is also modified as the dashed orange curve represents it in Figure 3.10.(a). One can clearly observe a spectral narrowing effect when comparing the DP spectrum to the spectrum of the initial single pulse (solid blue in (a)). Increasing further the temporal delay to the value of 14.7 fs, the constituting pulses destructively interfere, visible in Figure 3.10.(d), similarly as I presented previously in Figure 2.2.(b). The corresponding spectral intensity is demonstrated by the yellow circles in Figure 3.10.(a). With the peak intensity reduced in the time domain, the spectral interference shows two frequency bunches in the spectrum with much lower maximum spectral intensity than it could be observed in case of
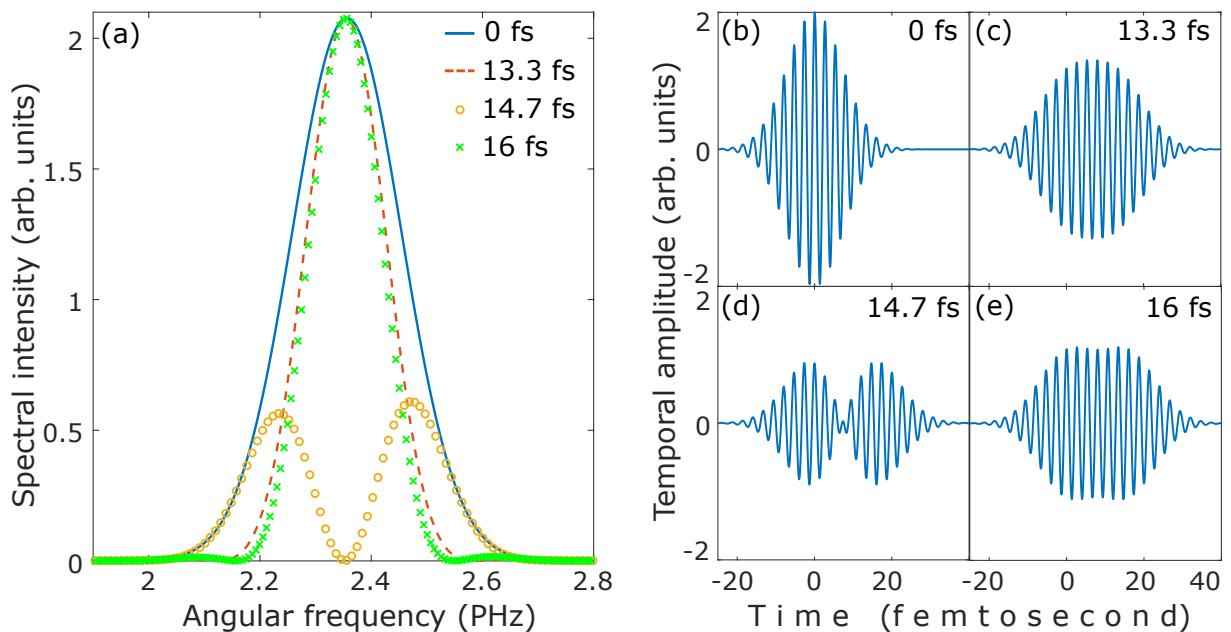
FIGURE 3.10: (a) Spectra of double pulses by applying different time delays between the constituting temporal peaks. (b)–(e) Corresponding temporal amplitudes at the delay of (b) 0 fs (solid blue in (a)), (c) 13.3 fs (dashed orange in (a)), (d) 14.7 fs (yellow circles in (a)), and (e) 16 fs (green crosses in (a)). The amplitude ratio is adjusted to R=1 (Eqn. 2.15). The initial pulse has a Gaussian-shape envelope with 12 fs long FWHM duration and 2.36 PHz central angular frequency.

the previous delay. By shifting further the same constituting pulse with one more half-cycle towards a longer time delay, i.e. to the delay of 16 fs, the temporal envelope of the resulting electric field has a super-Gaussian shape, as can be seen in Figure 3.10.(e). It can be of interest that there are more electric field half-cycles which have the same temporal amplitude. Therefore, there are numerous electron trajectories that have the same evolution, which results in sharper harmonics close to the cutoff region. The corresponding spectral intensity is shown by the green crosses in Figure 3.10.(a), which spectrum is slightly narrower than the obtained spectral intensity at the delay of 13.3 fs. By further increasing the temporal delay, more and more spectral bunches appear in the spectrum, resulting in a dense fringe pattern because of the spectral interference effect. With this representative example, I wanted to show the exact changes of the spectrum by changing the temporal delay between the constituting pulses. One can observe that there is an unambiguous spectral narrowing effect and there are also changes in the distribution of the spectral components, caused merely by the spectral interference of the two pulses.

One can achieve a similar outcome by using two femtosecond laser pulses with a fixed delay between them, and varying one constituting pulse's CEP (Figure 3.11). As a result, the relative CEP value between the two pulses changes. Analogously to Figure 3.10, subfigure (a) shows the spectral intensities of the constructed double pulses, while subfigures (b)-(e) represent the corresponding temporal amplitudes when introducing (b) 0 rad, (c) $\frac{1}{2}\pi$ rad, (d) π rad, and (e)
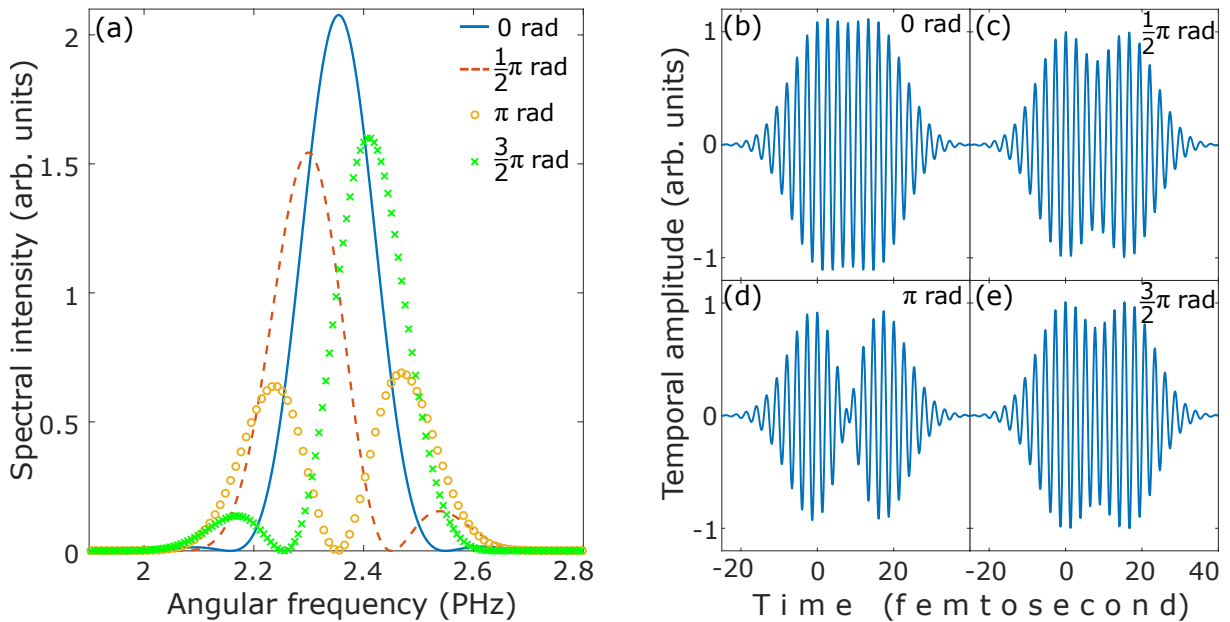
FIGURE 3.11: (a) Spectra of DP structures applying fixed, 16 fs time separation between the peaks, while one pulse's CEP varies. The spectral intensities are presented by applying 0 rad (solid blue), $\frac{1}{2}\pi$ rad (dashed orange), π rad (yellow circles), and $\frac{3}{2}\pi$ rad (green crosses) absolute CEP of one pulse, while the corresponding electric fields are demonstrated by subfigure (b)-(e), respectively. The applied initial pulse parameters are the same as those in Figure 3.10.

$\frac{3}{2}\pi$ rad absolute CEP for one of the constituting pulses (φ_{CEP} in Eqn. 2.15). The introduced fixed temporal delay is adjusted to 16 fs, where the two pulses constructively interfere with each other in case of 0 rad CEP. In fact, the blue curve in Figure 3.11.(a) is the same as the spectral intensity presented by the green crosses in Figure 3.10.(a). The electric field evolution in 3.11.(b) also matches the corresponding temporal amplitude, represented by Figure 3.10.(e). The initial pulse parameters are the same as those in Figure 3.10. One can clearly see that both the temporal amplitude and the spectral intensity vary by changing the CEP of one constituting pulse, and a similar spectral effect can be obtained as was presented in the previous case.

Basically, by varying the time separation between the two pulses of the DP structure, their relative CEP changes. Generally, the delay can be more easily controlled under experimental conditions, therefore I utilized the delay-variation method during my study to modulate the spectral characteristics of the laser source. In the following, I will focus only on the delay variation technique, and quantify which spectral characteristics and how much they change.

Two spectral characteristics of a laser source are worth investigating, namely the central angular frequency and the spectral bandwidth, since they have a strong influence on the HHG process. In case of pulses that have a Gaussian-shape spectrum, these characteristics can be easily determined, because their spectral components have symmetric distribution. However, for asymmetrical spectral intensities, this task is not so obvious. For such spectra, the following mathematical expression (weighted mean) is worth using to calculate the central angular frequency:

$$\omega_0 = \frac{\int_{-\infty}^{\infty} \omega I(\omega) d\omega}{\int_{-\infty}^{\infty} I(\omega) d\omega}, \tag{3.7}$$

where $I(\omega)$ denotes the spectral intensity at ω angular frequency. Analogously, the spectral bandwidth can also be determined by applying the relation of

$$\Delta\omega = \sqrt{\frac{\int_{-\infty}^{\infty} (\omega - \omega_0)^2 I(\omega) d\omega}{\int_{-\infty}^{\infty} I(\omega) d\omega}}. \tag{3.8}$$

In Eqn. 3.8 the term ω_0 represents the central angular frequency given by Eqn. 3.7, and $I(\omega)$ and ω have the same physical interpretation as in Eqn. 3.7.

By changing continuously the temporal delay between the constituting pulses of the constructed DP structure, because of spectral interference, the central angular frequency and the spectral bandwidth can be controlled as shown by the blue and orange curves in Figure 3.12.(a) and (b), respectively. Since the relative CEP varies between the two pulses by changing the delay, the two distinct laser electric fields interfere constructively at certain delays, and destructively at other time separations. For this reason, the peak intensity of the sum electric field periodically falls below the ionization threshold. Therefore, at those time separations HHG is only feasible if the pulses are able to generate high-order harmonics individually. However,

in case of such high individual pulse intensities, the sum electric field results in unnecessar-
ily high peak intensities. So it is important to mention that in case of small temporal delays
(< 9.5 fs) this aspect has to be considered to stay physically relevant. I would say, by applying
small time separations the pulses more significantly overlap, resulting in extreme high peak in-
tensities that could cause undesirable physical effects, including overionization and high free
electron density, which may restrict emission efficiency of the harmonic generation process. In
the opposite case, namely at higher time separations (> 17 fs), peak intensity of the sum electric
field can be so low that the driving field is not capable to free electrons, thereby there will be
no XUV photon emission. Therefore, unnecessarily long time delays must be avoided, because
the total peak intensity could be so low that the maximum electric field could not overcome
the ionization potential energy of the target atom. In addition, the observable tuning efficiency
of the central angular frequency decreases. I would like to point out that the two values of the
delay limits for the adequate and physically relevant experimental conditions is only associ-
ated with the current pulse parameters. The most appropriate delay range to drive the HHG
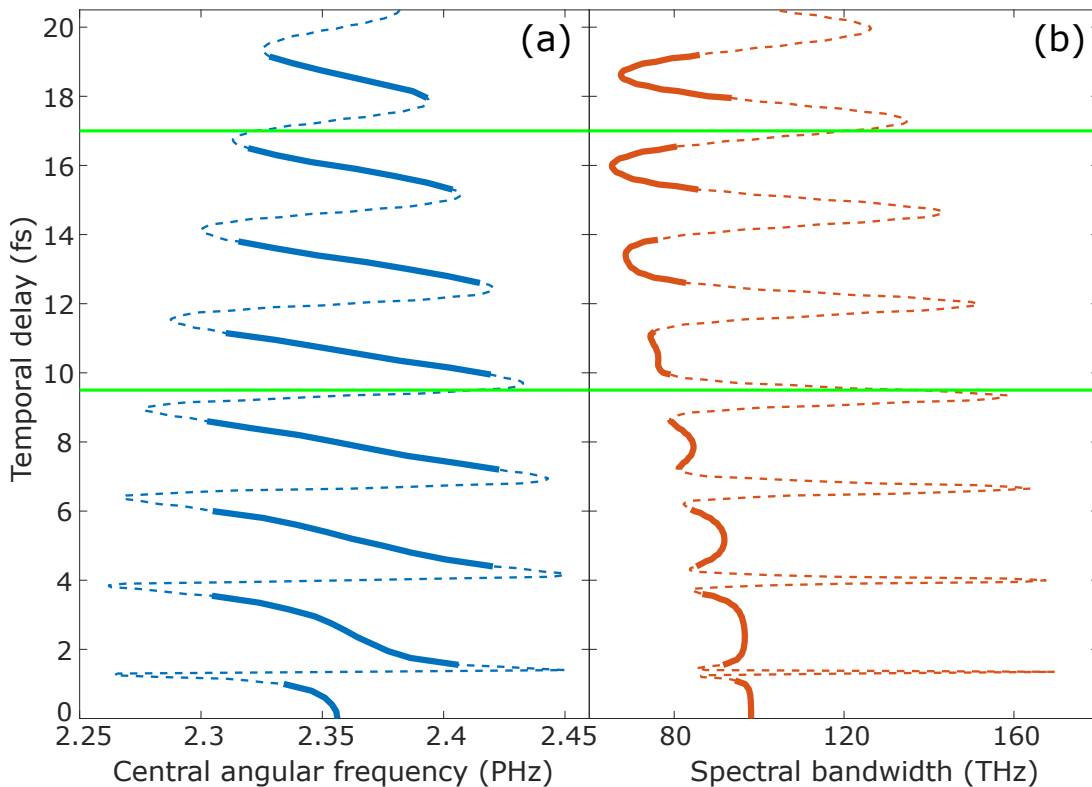
FIGURE 3.12: (a) Variation of the central angular frequency and (b) the spec-
tral bandwidth of the DP structure by changing the time separation between the
constituting pulses. The initial single pulse has 12 fs long FWHM duration and
2.36 PHz central angular frequency, which can be seen in subfigure (a) at the po-
sition of zero delay. The solid blue and orange curves show the delay positions
where the two pulses constructively interfere, or in other words, where the sum
electric field is presumably intense enough to drive the HHG process. The dashed
curves show destructive interference regions in both figures. The two horizontal
solid green lines indicate the delay range used for further simulations.

process is indicated by the two horizontal solid green lines in both subfigures of Figure 3.12. This indicated range is utilized in the further simulations.

This specific delay range varies with changing driving pulse length. Generally speaking, the amount of time separation between the two pulses of the DP structure must be pulse-duration-comparable, otherwise the tuning effects will be less observable, and undesirable hindering processes may occur. The delay regions, where the two constituting pulses constructively interfere, and the double pulses can be applied to drive the HHG process, are approximately presented by the solid blue and orange curves in Figure 3.12.(a) and (b), respectively. In the regions, shown by the dashed curves in both subfigures, there is a close to π phase shift between the two interfering electric fields, so they are out of phase and they destructively interfere with each other. Selecting the appropriate time separation values in case of a given pulse duration is even more critical when using few-cycle pulses as the driving source of HHG, where the peak intensity can dramatically increase or decrease by half-cycle to half-cycle. Moreover, an ultrashort laser pulse electric field consists of fewer cycles which can interfere, but a 12 fs long temporal length for the pulse duration is sufficient to observe the tuning effects in harmonics, as I will present it in the following section. Furthermore, in Section 3.3, I will present that multi-cycle driving laser pulses are also adequate to reach the results presented in this section and to perform a successful experimental realization.

3.2.2 The impact of double pulses on the high-order harmonic generation process

As I proposed an experimentally feasible method in Section 3.2.1 to introduce modifications in the spectrum of a laser source, one can reasonably expect that by using such laser field to drive the HHG process there would also be observable spectral modulations in the produced dipole spectra. For this reason, in this section I will focus on the theoretical investigations of harmonic generation in gaseous material driven by double pulses, where the time delay between the constituting pulses is pulse-duration-comparable, and continuously changes in a physically relevant range from an experimental point of view.

As one could see in Figure 2.9.(a), the numerical solution of the Lewenstein integral results in a harmonic dipole spectrum that has the same, or at least similar spectral characteristics as in case of using SPA. Therefore, in the simulations, I calculated the numerical solution of the Lewenstein integral only. In the calculations, propagation effects, such as dispersion, plasma generation, absorption and self-focusing effects are not considered. The applicability of these simplifications will be justified by the experimental results. In the driving DP structure both single constituting pulses have a Gaussian-shape temporal envelope, having 12 fs long FWHM duration, and their spectral components are concentrated around 800 nm central wavelength (corresponding to 2.36 PHz). The absolute CEP is chosen as 0 rad for both pulses, and higher-order dispersion terms are not added to their simulated spectral phase either. The individual

peak intensity is close to $2.3 \times 10^{14} \; \frac{W}{cm^2}$. However, because of the interaction of the two pulses, the final laser electric field results in slightly higher peak intensity values. The double pulses are constructed by applying time delays between 9.5 fs and 17 fs (indicated by the region between the two green horizontal lines in Figure 3.12), where the total driving electric field does not lead to overionization in the target gas material, but is still intense enough to drive the HHG process. For the delay scan, 50 as time resolution is used. The amplitude ratio between the constituting pulses is chosen as R=1 (Eqn. 2.15). The target gas is argon, which has an ionization energy (I_p) of 15.76 eV. In the atomic dipole matrix element, the fitting parameter is chosen as $\alpha = I_p$ (Eqn. 2.31).

High-order harmonic spectra obtained by applying the parameters summarized above are presented by the coloured map in Figure 3.13. The white dotted curves represent the expected delay-dependent spectral positions of high-order harmonics ($E_q(\tau)$) by upscaling the delay-dependent central angular frequency of the driving laser field ($\omega_0(\tau)$):

$$E_q(\tau) = q\hbar\omega_0(\tau). \tag{3.9}$$

In Eqn. 3.9, q is the harmonic order and $\hbar$ denotes the reduced Planck constant. In fact, the solid blue curves in Figure 3.12.(a) are upscaled only, since destructive interference regions (dashed blue curves in Figure 3.12.(a)) are not relevant. As a matter of fact, there is no XUV photon emission at these destructive interference time delay instants, because of the too low driving peak intensities, which physical reason has already been described in Section 3.2.1. The destructive interference of the driving laser electric field can also be clearly observed in the coloured map of Figure 3.13 (dark blue regions).

The periodicity of the harmonic bunches along the delay axis is unequivocally connected to the period of the laser electric field full cycle (T_0). The peak-to-peak distance in the delay of harmonic bunches can be defined as

$$T_0 = \frac{2\pi}{\omega_0}, \tag{3.10}$$

which is 2.67 fs for the above written simulation parameters. I must point out that in Eqn. 3.10 the parameter ω_0 is not the delay-dependent central angular frequency, but the exact central angular frequency of the single laser pulse, which is chosen as 2.36 PHz. Therefore, the peak of the harmonic bunches appear around the time separations of 10.68 fs, 13.35 fs, and 16.02 fs in the investigated delay region, which specific time instants are the middle regions of constructive interference in Figure 3.12.

One can clearly see in Figure 3.13 that the produced high harmonics show a spectral tuning effect by increasing temporal delay. This phenomenon is unambiguously attributable to the caused spectral modulations in the spectrum of the driving laser. Furthermore, there is a good
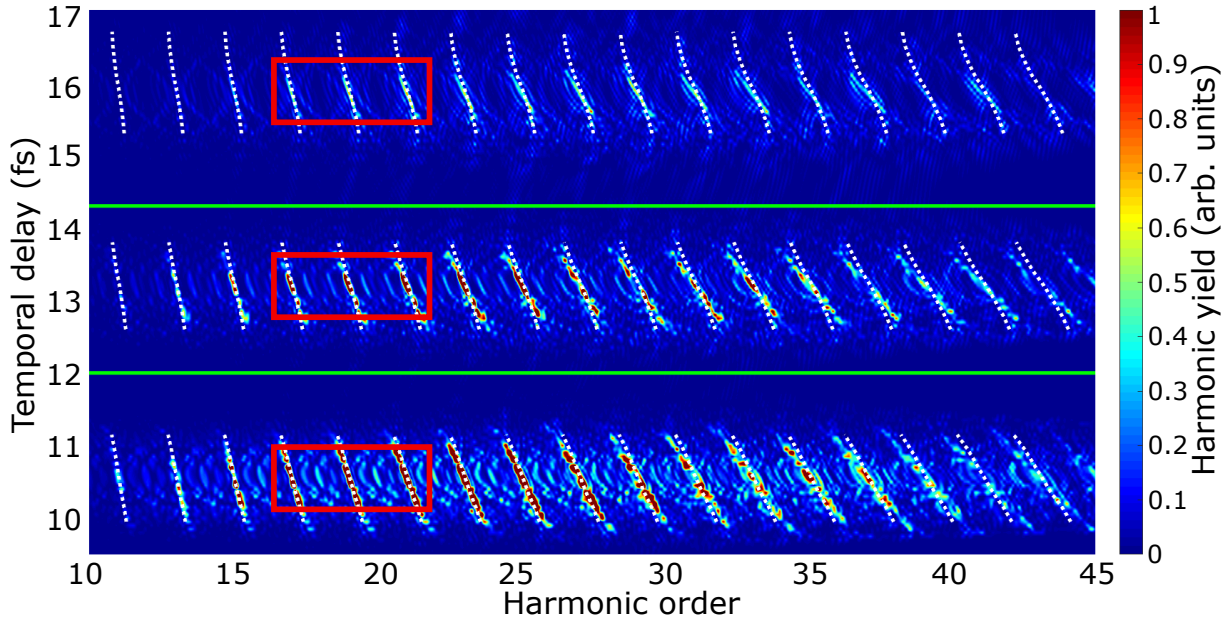
FIGURE 3.13: Simulated high-order harmonic spectra obtained by using the numerical solution of the Lewenstein integral (coloured map). Propagation effects are not considered. The driving DP structure consists of two identical pulses, having a Gaussian-shape temporal envelope with 12 fs long FWHM duration. Their central angular frequency is 2.36 PHz. The amplitude ratio is R=1 (Eqn. 2.15) between the constituting peaks, and the introduced delay between them varies from 9.5 fs to 17 fs by applying 50 as step size. The individual peak intensity of one constituting pulse is $2.3 \times 10^{14} \frac{W}{cm^2}$. The white dotted curves show where the harmonics should appear according to the upscaling of the central angular frequency of the driving laser source, calculated by the expression of Eqn. 3.9. The two horizontal green lines show the region which is investigated in more detail for the photon energy tuning effect. Moreover, the three red rectangles indicate harmonics the spectral bandwidth of which is compared to each other.

match between the produced harmonics and the upscaled delay-dependent central angular frequency curves ($E_q(\tau)$), calculated by Eqn. 3.9. To gain a deeper insight into the real physical phenomenon of photon energy tuning and spectral bandwidth variation, in the following sections I will study the two observed effects separately, and I will quantify the introduced modifications in the spectral characteristics of the produced high-order harmonics. The two horizontal green lines indicate the range of time separations that is used for further investigations of the energy tuning effect. Moreover, the three red rectangles mark the harmonics the spectral bandwidth variation of which is studied more thoroughly via additional simulations.

3.2.2.1 Tuning the energy of extreme ultraviolet photons

Firstly, I investigate the XUV photon energy tuning effect in more detail by choosing a smaller region from the longer delay scan in which only one harmonic bunch is covered. In the following, the delay range between 12 fs and 14.3 fs is studied, which is presented in Figure 3.14. The harmonic spectra are taken from Figure 3.13, namely from the area bounded by the two horizontal green lines, therefore the parameters of the driving double pulses and the
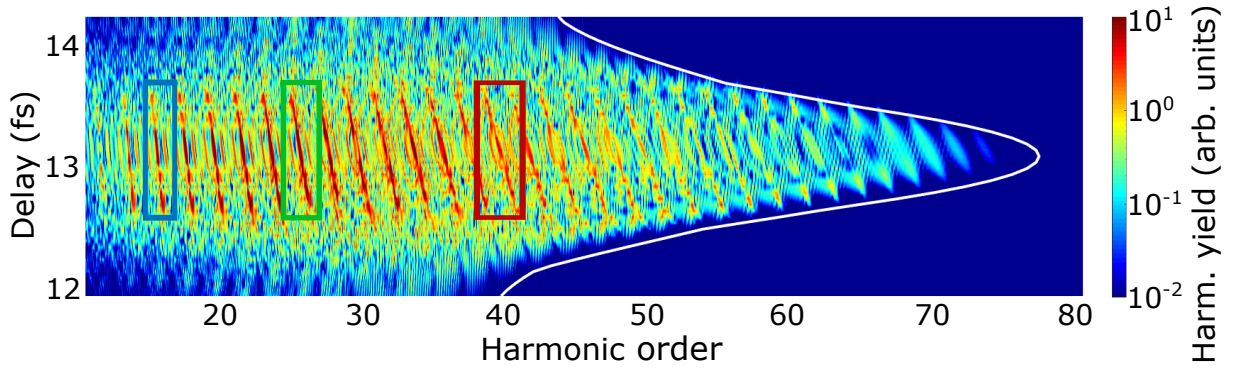
FIGURE 3.14: Harmonic dipole spectra taken from the area bounded by the two horizontal green lines in Figure 3.13. The colourscale in this figure is logarithmic, therefore the less intense cutoff harmonics can also be observed. The limits of the presented delay range are 12 fs and 14.3 fs. The solid white curve demonstrates the cutoff positions of the harmonic spectra at each temporal delay. The blue, green, and dark red rectangles indicate the 15th, 25th, and 39th harmonics, respectively, which are studied for quantifying the photon energy tuning phenomenon of high-order harmonics (Figure 3.15).

simulation conditions of HHG are the same as those in Section 3.2.2. For the sake of the better visibility of the harmonic tuning effect, the dipole spectra are represented on a logarithmic scale in Figure 3.14. Therefore, the less intense harmonics become visible, and the produced XUV radiation can be studied up to the cutoff energy, that is almost at the harmonic order of 70 in case of 13.25 fs delay. In Figure 3.13 the harmonics that have lower photon energy, or in other words, which are located in the plateau region of the HHG spectrum, are presented only, while in Figure 3.14 the entire harmonic spectra can be seen with the cutoff included. The solid white curve represents the cutoff photon energies of the HHG spectra at each temporal delay, calculated by the expression of Eqn. 2.26. In this relation, the ionization potential is fixed at 15.76 eV, since the target gas is argon in these calculations. However, the ponderomotive energy is scaled by the peak intensity (I) and the central wavelength (λ) of the driving double pulses as follows

$$U_p[eV] = 9.337 \times 10^{-14} I \left[\frac{W}{cm^2} \right] (\lambda[\mu m])^2, \qquad (3.11)$$

where λ is also chosen as a fixed value, i.e. as is the central wavelength of the single laser pulse, 0.8 μm. Nevertheless, the peak intensity, given in the units of $\frac{W}{cm^2}$ in Eqn 3.11, significantly varies when the delay is changed. Thus the ponderomotive energy also changes by increasing time separations between the constituting pulses of the DP structure.

One can unambiguously observe that the spectral tuning effect of harmonics is more and more prominent with increasing harmonic order. To be able to quantify this phenomenon, I investigated three different harmonics from the low, middle, and high photon energy ranges

of the harmonic dipole spectra, i.e. the 15th, 25th and 39th harmonic orders. The chosen harmonics are indicated by the blue, green, and dark red rectangles in Figure 3.14. By determining at each delay the spectral positions of the investigated harmonics, one can obtain linearly descending energy values by increasing the temporal delay between the constituting pulses of the DP structure, which is presented by the circles in Figure 3.15 in case of the 15th (blue), 25th (green), and 39th (dark red) harmonic orders. It must be noted that for the sake of better comparability, the nominal photon energy of harmonics (E_{nom}) has been shifted by their central photon energy value ($E_{nom} = q \times \hbar \times \omega_{800nm}$, where q is the harmonic order, ω_{800nm} denotes the central angular frequency of the driving laser source, and $\hbar$ is the reduced Planck constant). Thus the investigated harmonics overlap around the time separation of 13.25 fs, which is approximately $5 \times T_0$ (T_0 is defined by Eqn. 3.10). By making a linear fit to the data (represented by the correspondingly coloured solid lines in Figure 3.15), the tuning ranges of the relative central photon energies in case of different harmonic orders can be quantified. From these linear fits, one can observe clearly that the central photon energy of the 15th harmonic can be controlled within an energy range of ~ 1 eV, while this range in case of the 39th harmonic almost reaches 2 eV, as presented by the solid dark red curve. The scaling of the exact central photon energy tuning ranges with increasing harmonic orders will be given in the discussions of the experimentally obtained results (Section 3.3). In this subsection I just wanted to point out that the observed harmonic tuning effect is more pronounced in case of the plateau harmonics, and
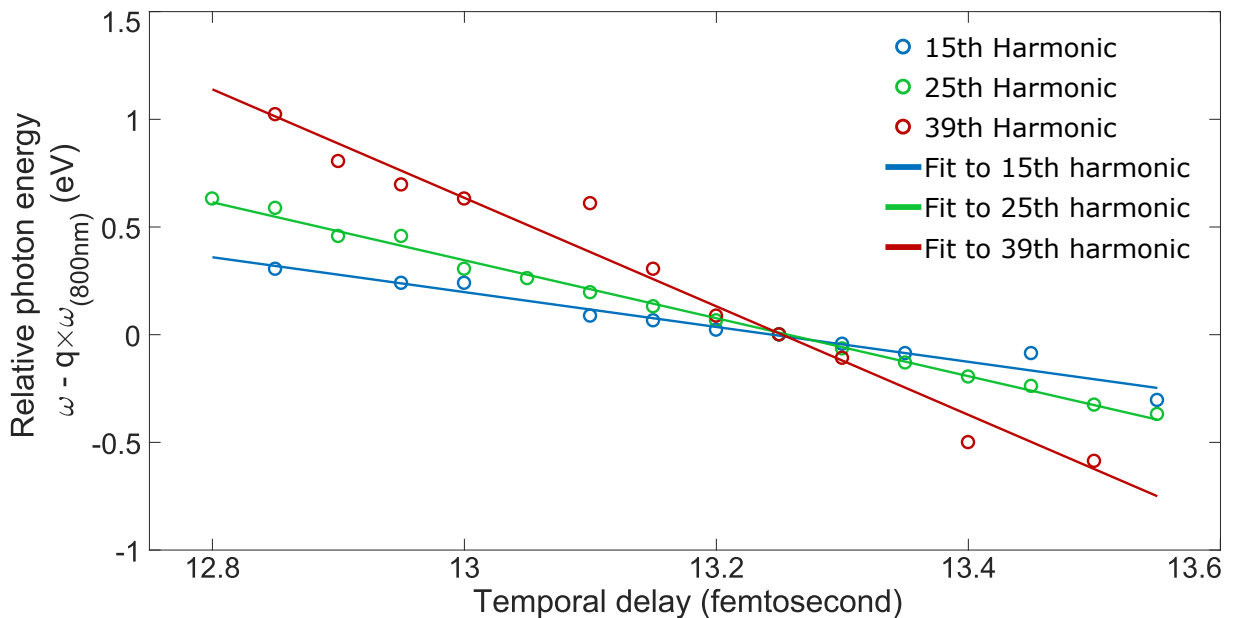
FIGURE 3.15: Central photon energy tuning range of harmonic 15th, 25th, and 39th by changing time delay between the constituting pulses of the driving DP structure. These harmonics are indicated in Figure 3.14 by the blue, green and dark red coloured rectangles in case of the 15th, 25th, and 39th harmonic orders, respectively. The circles represent the spectral positions of harmonics at each delay, while the correspondingly coloured solid lines are linear fits to these data, from which the relative photon energy tuning ranges can be estimated.

the higher-order harmonics can be tuned on a broader energy range than the lower-order ones.

From these theoretical calculations I have concluded that by modulating the spectrum of the driving laser source of HHG, the central photon energy of the generated high-order harmonics can be controlled on a broader energy range than the central photon energy of the driving laser source. This effect is a clear consequence of the simple rules of generating higher-order harmonics, however, the phenomenon is more expressed in case of plateau harmonics, where more electron trajectories contribute to the construction of harmonics. As a conclusion, these spectral characteristics can be studied by numerically solving the Lewenstein integral.

3.2.2.2 Alterations in the spectral bandwidth evolution of high-order harmonics

In Section 3.2.1, I have already demonstrated the spectral modulations in the spectrum of femtosecond double pulses introduced by simply changing the temporal delay between the two constituting pulses of the DP structure. Due to the interference of the pulses, the spectral bandwidth of the resulting spectrum also varies with the modification of the temporal separation, similarly to the modulation of the central angular frequency (Figure 3.12). The impact of the central angular frequency variation of the driving laser source on the generated high-order harmonics has already been presented in the previous section, and the main conclusion was drawn, namely that the produced XUV radiation inherit this modulated spectral property from the driving laser. For this reason, the spectral bandwidth evolution of the generated harmonics is also worth investigating by applying double pulses to drive the HHG process in gaseous material. The modifications caused in the spectral width of the DP spectra have been already presented in Figure 3.12.(b), therefore one can reasonably expect similar tendencies in the spectral bandwidth of the produced high-order harmonics by increasing the temporal delay between the constituting pulses of the driving DP structure.

In this subsection I also choose smaller fractions from the longer delay scan (Figure 3.13), as I did during the investigations of harmonic central photon energy tuning. In the current case, the spectral bandwidths of the harmonics indicated by the three red rectangles in Figure 3.13 are studied in more detail. Evidently, the applied driving laser pulse parameters and HHG conditions are the same as those in Section 3.2.2. The 17th, 19th and 21st harmonics are chosen for the investigation of their spectral bandwidth in a delay range containing three regions with enough intensity to generate harmonics, namely around the time delays of $4 \times T_0$, $5 \times T_0$, and $6 \times T_0$, where T_0 = 2.67 fs is the optical cycle of the driving laser electric field. Around these three specific delays, the spectral intensity of the 17th harmonic is presented by the coloured map in Figure 3.16.(a), (d), (g), the 19th harmonic is shown by (b), (e), (h), and the 21st harmonic is represented by the subfigures (c), (f), (i), respectively. To determine the spectral bandwidth, the relation of Eqn. 3.8 is utilized, where $I(\omega)$ denotes the spectral intensity of the investigated harmonic in the current case, and ω_0 is the central photon energy of the given harmonic peak,
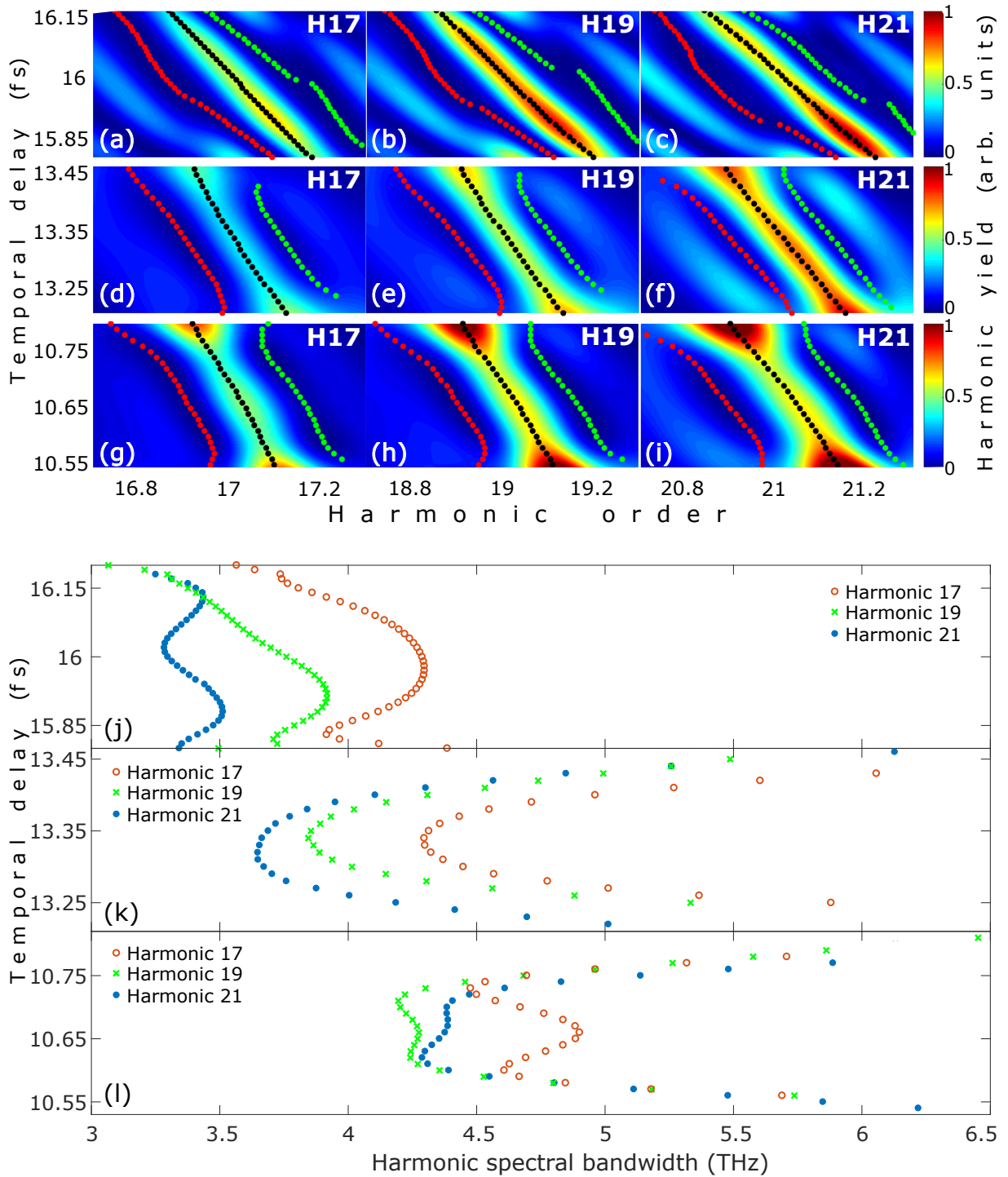
FIGURE 3.16: (a), (d), (g) 17th harmonic, (b), (e), (h) 19th harmonic, and (c), (f), (i) 21st harmonic around the time delays of $4 \times T_0$, $5 \times T_0$, and $6 \times T_0$, where $T_0 = 2.67$ fs is the temporal duration of a full laser optical cycle. The black dots show the central photon energy in each subfigure. The red and green dots represent the lower and upper limits of the evaluation region of the spectral bandwidth. (j), (k), (l) demonstrate the calculated spectral bandwidths around the time delay of $6 \times T_0$, $5 \times T_0$, and $4 \times T_0$, respectively, in case of 17th (orange open circles), 19th (green crosses), and 21st (blue dots) harmonics.

which are represented by the black dots in Figure 3.16.(a)-(i). The spectral positions of the black dots are calculated by using the relation written by Eqn. 3.7. In this equation, $I(\omega)$ has the same meaning as in case of the bandwidth calculations, and the integration is performed between the two nearest spectral valleys to the harmonic peak intensity, presented by the green and the red dots in Figure 3.16.(a)-(i). These borders cover an approximately $0.3 \times E_{laser}$ energy range, where E_{laser} is the energy of one driving laser photon, equalling approximately 1.55 eV. By calculating the bandwidths of the 17th, 19th, and 21st harmonics, the outcomes are shown in Figure 3.16.(j), (k) and (l) in case of temporal delays around $6 \times T_0$, $5 \times T_0$ and $4 \times T_0$, respectively.

One can clearly see that the obtained harmonic bandwidths are in the range of a few THz, which value is significantly smaller than the bandwidth of the driving laser spectrum, being around 60 THz in the range of the investigated time delays, marked approximately by the two horizontal green lines in Figure 3.12.(b). This is a credible outcome, since the harmonic spectral bandwidth is inversely proportional to the number of laser half-cycles, which contribute to the construction of the harmonic dipole spectrum. Therefore, the width of the high-order harmonics must be appreciably narrower than the spectrum of the utilized laser. These spectral bandwidth differences of high-order harmonics within a dipole spectrum can be more clearly observed in case of few-cycle laser pulses, having less than 5 fs long FWHM duration. When following this theoretical approach, the bandwidth grows as the harmonic order increases, but this tendency cannot be observed in Figure 3.16.(j)-(l). The difference from the theoretical observations is due to the large number of contributing half-cycles, since the simulated double pulses contain almost 30 half-cycles at the width of $1/e^2$, all of which contribute to the harmonic emission. Because of the large number of contributing short and long trajectories, trajectory interferences take place. Thereby the bandwidths of the consecutive harmonics cannot be determined with high accuracy.

Nevertheless, by comparing the bandwidth evolutions corresponding to the different harmonic orders we can conclude that spectral narrowing occurs in case of all investigated harmonic peaks when the temporal delay is increased. This narrowing effect also appears in the width of the driving laser spectrum (see Figure 3.12.(b)). Moreover, around the delay values of $4 \times T_0$ and $5 \times T_0$, the tendencies of the studied high harmonic widths are similar to the laser spectral bandwidth evolutions at the corresponding time separations. An exception is the spectral bandwidth tendencies at the delays around $6 \times T_0$ time separations. I also attributed these discrepancies to the large number of interfering trajectories which are getting more conspicuous with increasing temporal delay. Longer time delays between the constituting pulses of the DP structure result in a super-Gaussian shape pulse envelope, which contains more half-cycles able to free electrons, and thereby increase the number of contributing electron trajectories to harmonic emission. This is the main reason why I chose lower order harmonics, because the

higher harmonics are not prominent, and they are slightly blurred as it can be seen in Figure 3.13 and 3.14. Therefore, the evaluation of the spectral bandwidth in case of higher order harmonics becomes difficult.

As a conclusion it can be drawn that the produced high-order harmonics inherit certain spectral bandwidth properties from the driving electric field, in addition to the central angular frequency of the utilized laser. In fact, the large number of interfering electron trajectories affect the spectral bandwidth evolution of harmonics. However, the spectral bandwidth tendency of the driving laser can be observed in the bandwidth curves of the investigated harmonics. Moreover, the demonstrated spectral narrowing effect with increasing time separation, presented in Figure 3.12.(b), can be seen in Figure 3.16.(j)-(l) as well.

Summary II. *I have investigated theoretically the impact of the temporal double-pulse structure on the high-order harmonic generation process. I have proposed to use these electric field structures to control the spectral characteristics of the generated high-order harmonics. I have demonstrated with simulations that the central photon energy of the harmonics can be directly tuned, and that the tuning range broadens with increasing harmonic order. Moreover, I have shown that spectral narrowing of harmonics can also be achieved by increasing of the temporal delay between the driving interfering pulses* [T2].

Legal notes:

3.3 Experimental observations in high-order harmonics generated by double pulses

In Section 3.2, the impact of double pulses on the high-order harmonic generation process has been investigated theoretically. I presented a method to control two important spectral characteristics of the generated harmonics, namely their central photon energy and spectral bandwidth by simply changing the temporal delay between the constituting pulses of the driving DP structure.

In this section I summarize the results of the experimental validation of the theoretically observed spectral tuning effects [T3]. First, the utilized laser system and the attosecond pulse generation beamline will be presented, including the spectral and temporal characteristics of a typical laser pulse [O1]. Second, I will describe the utilized experimental method to produce double pulses, since the applied DP production technique during this experimental campaign is different from the method described in Section 3.1.3. During these measurements a split-and-delay unit (SDU) was applied to form double pulses [49]. Moreover, I will present both simulated and experimentally recorded spectra of double pulses acquired by the utilization of the high-repetition-rate laser source of ELI ALPS, i.e. the HR-1 laser system. In addition, I will show a long delay scan, covering a more than 35 fs temporal range, therefore containing numerous constructive and destructive interference time separations. Finally, I will investigate the control of the two spectral characteristics of the produced XUV radiation, and summarize the observed experimental phenomena.

3.3.1 Technical details of the experimental campaign and the results of preliminary measurements

The experimental campaign took place at the Extreme Light Infrastructure - Attosecond Light Pulse Source (ELI ALPS) Research Facility. We used the HR-1 laser system emitting ultrashort, high-repetition-rate pulses. The most relevant technical details of the laser system will be summarized in Section 3.3.1.1. The laser source drives the gas high-order harmonic generation beamline, where gas phase material is targeted in the experimental end-station (called HR GHHG GAS beamline). This secondary light source emits pulse trains, containing attosecond temporal peaks. The most significant parameters of the beamline will be discussed in Subsection 3.3.1.2. Then, I will describe a noncollinear experimental arrangement for the generation of double pulses in Section 3.3.1.3, namely the application of the SDU will be detailed. Finally, the experimentally produced DP spectra will be demonstrated, together with investigations of delay-dependent spectral characteristics. In Section 3.3.1.4 these pulses are used to drive the high-order harmonic generation process.

3.3.1.1 Driving laser source

As I have already mentioned, the driving laser source used during the experimental campaign was the HR-1 laser system of ELI ALPS Research Institute. The HR-1 laser is designed to emit 1 mJ energy ultrashort pulses, having only a few optical cycles within the temporal envelope of the oscillating electric field. The radiation is emitted in the near-IR wavelength range, the spectrum is concentrated around 1030 nm central wavelength, which corresponds to 1.83 PHz central angular frequency. Therefore, the theoretical limit for a single optical cycle of the laser electric field, discussed in Section 2.1, is ~ 3.4 fs. This characteristic time period will appear in the delay-dependent spectrum of double pulses (Section 3.3.1.4), and therefore in the high-order harmonic generation delay scan too (Figure 3.22).

The temporal duration of laser pulses can be varied on a wide range, between 6.2 fs and 200 fs. It is important to note that the achievable output average power is not constant when the laser pulse duration changes. When the pulse length decreases, the achievable maximum average power also decreases. The physical reason is simple: few-cycle, intense pulses cause undesirable nonlinear effects by propagating through the gas-filled hollow-core fibre. Moreover, the output power of the laser system can be fine-tuned in the long-pulse mode (if pulse duration is longer than 18 fs). The source of the tuning range limitation is the applied transmissive optics, since the power control is carried out by using the sequence of a polarizer and a half-wave plate.

During the measurements, we typically used 30 fs long laser pulses, having an average power of 90 W. In the current configuration, the attosecond pulse generation beamline provides optimum and stable high-order harmonics with the above laser parameters. Additionally, another reason for using such long pulses is that the influence of CEP on the HHG process can be fully eliminated. Regardless whether cutoff harmonics are investigated or not (in the first case the CEP variations of the driving field is more important), I preferred to work in the long-pulse mode since the HR-1 laser system was not CEP stabilized.

A typical single pulse spectrum and temporal envelope of the HR-1 laser is presented in Figure 3.17.(a) and (b), respectively. It must be noted that the demonstrated spectral (solid blue curve in (a)) and temporal evolution (solid blue curve in (b)) are not the results of real pulse characterization. In fact, the laser spectrum was recorded by using a high sensitivity near-IR spectrometer, and the corresponding Fourier-limited pulse envelope was calculated. The central angular frequency of the presented laser spectrum was determined by utilizing Eqn. 3.7, marked by the black dashed vertical line in Figure 3.17.(a). One can clearly observe sharp peaks in the demonstrated laser spectrum, especially in the middle part, which is really far from the ideal Gaussian-shape spectrum. It is the result of the amplification stage of the system, however, the investigation of these spectral characteristics is out of the scope of this research. I just wanted to point out that in contrast to this observation, during the theoretical
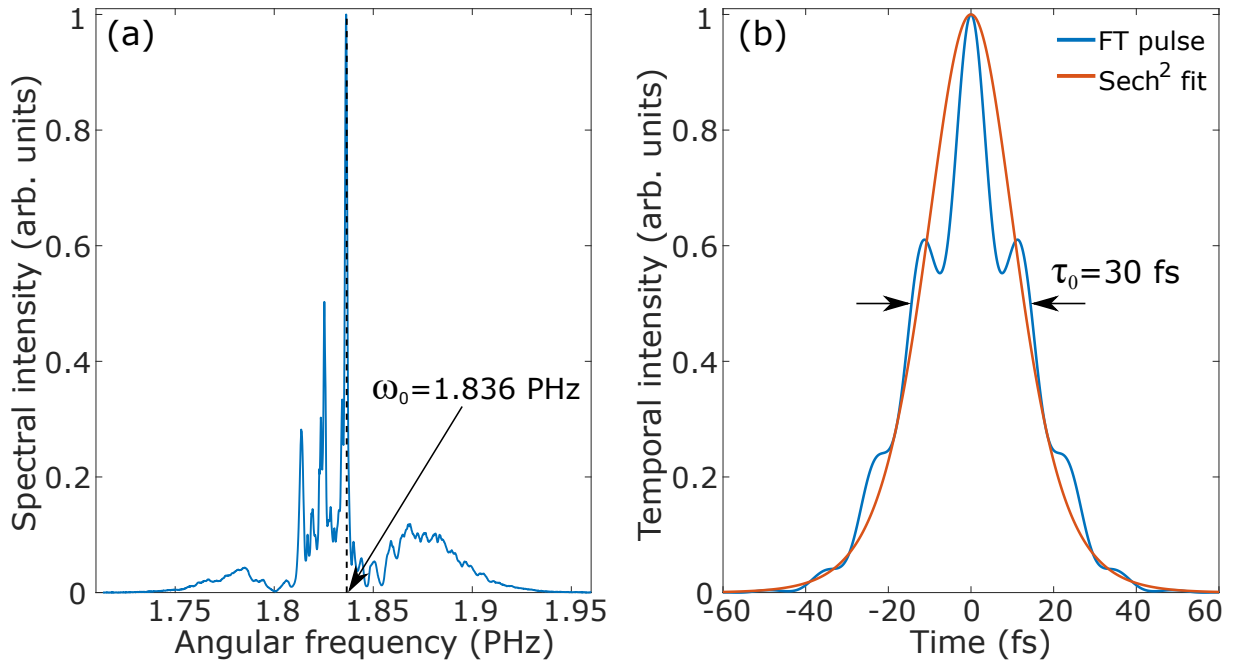
FIGURE 3.17: (a) Spectrum of the utilized laser source and (b) the corresponding temporal envelope of the laser pulse. The central angular frequency is 1.836 PHz, which is calculated by using the formula of Eqn. 3.7. The obtained value is indicated in (a) by the black dashed vertical line. The FWHM duration of the laser pulse is ~ 30 fs, indicated in Subfigure (b). A *sech*² function is fit to the obtained pulse envelope (solid orange in (b)), which has a slightly shorter FWHM duration, approximately 27 fs.

calculations the results were obtained by applying Gaussian-shape laser pulses to drive the HHG process (see Section 3.2). During the experimental campaign, the driving laser spectrum was significantly different from the simulated one, but this does not prevent validation of the theoretically observed spectral tuning effects to be presented later. The transform-limited laser pulse envelope is shown by the solid blue curve in Figure 3.17.(b), calculated by applying the Fourier theorem, and the FWHM duration was found to be τ_0 = 30 fs, which is also indicated in the figure. One can clearly see side-lobes both on the leading and trailing edges of the laser pulse, so the temporal evolution is also different from the ideal Gaussian-shape envelope. Therefore, I made a squared secant hyperbolic (*sech*²) fit to the laser pulse, and the outcome is depicted by the solid orange curve in Figure 3.17.(b). The FWHM duration of *sech*² fit is slightly shorter (27 fs) than the Fourier-limited pulse length.

In the current configuration, the laser system emits high-repetition-rate ultrashort pulses, having the spectral and temporal characteristics summarized above. After the laser output, the beam travels a distance of approximately 12 m until it reaches the harmonic generation beamline. However, the utilized pulses have close to Fourier-limited temporal duration, since most of the propagation takes place in vacuum. Therefore, pulse-distorting effects are only introduced by the beam steering optics, but as they have low dispersion, the laser pulses are not stretched significantly until the experimental application.

3.3.1.2 Attosecond pulse generation beamline

It has already been mentioned that the experimental campaign was carried out at ELI ALPS Research Institute, and the HR GHHG GAS beamline was utilized to verify the theoretically predicted spectral tuning phenomena. In this subsection, I will summarize the technical details of the harmonic generation beamline, and I will describe the experimental conditions, including the generation and detection geometries of high-order harmonics [T3], [O1].

The simplified schematic layout of the attosecond pulse generation beamline is presented in Figure 3.18. The red shaded regions represent the propagation paths of the HR-1 laser beam. The incoming beam is split by the holey-splitting mirror (HSM) into an annular and a central part. The annular beam is used to generate high-order harmonics, while the central part is dedicated to serve as a probe beam for XUV-IR pump-probe experiments, e.g. in measurements aimed at the temporal characterization of the produced XUV radiation by the RABBITT technique, which method was briefly described already in Section 2.3.3. The steering optics
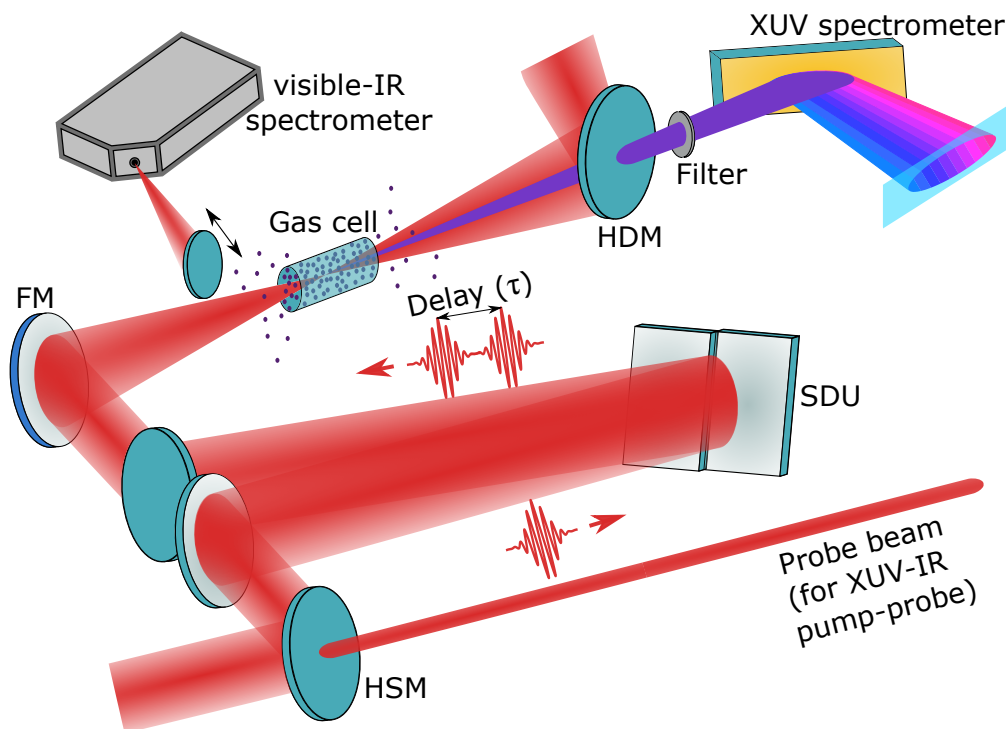
FIGURE 3.18: Simplified schematic experimental arrangement of the HR GHHG GAS attosecond pulse generation beamline at ELI ALPS Research Institute. The main constituting optical elements of the beamline are: holey-splitting mirror (HSM), split-and-delay unit (SDU), focusing mirror (FM), visible-IR spectrometer, XUV generation gas cell, holey-dumping mirror (HDM), metallic filter, and XUV flat-field spectrometer. The flat-field spectrometer consists of a variable-line-spacing XUV grating, a microchannel plate, a phosphor screen, and a CMOS camera. The red shaded parts represent the IR beam, while the purple regions demonstrate the propagation path of the generated XUV radiation. The colourscaled beams from blue to violet in the XUV spectrometer section represent the spectrally resolved high-order harmonics.

of the HR-1 laser beam are low-dispersion, broadband hybrid mirrors having high-reflectivity. The arrangement in the beamline had been demonstrated by Ye *et al.* in Ref. [O1]. However, during the current experimental campaign, one of the steering mirrors in the beampath of the harmonic generation beam was replaced by a custom-made optomechanical element called split-and-delay unit (SDU) [49], which spatially divides the incoming beam into two. Basically, the SDU is utilized to produce the double pulses, therefore the technical details of the device and the production process of the DP structure will be described in more detail in the following section. Regarding the IR propagation path, after the SDU the two laser beams reach the focusing mirror (FM), having 900 mm focal length, and the FM focuses the two beam fractions into the gas cell. The small dots inside and around the gas cell represent gas atoms (or molecules) of the target gaseous material. When sufficiently high driving intensity is achieved, XUV radiation is produced, which is represented by purple coloured line after the gas cell. The generated XUV and the driving IR beams propagate together until they reach another holey mirror, the holey-dumping mirror (HDM), which reflects out most of the IR radiation and then the IR beam is dumped. The XUV goes through the central hole of HDM, because the divergence of the XUV radiation is significantly smaller than the driving laser's field divergence. The residual IR radiation is filtered out by a metallic filter. It must be noted that such filters are also used to spectrally calibrate the generated high-order harmonic spectrum. Finally, the produced XUV radiation reaches the diagnostic section of the beamline. For diagnostic purposes we used an XUV flat-field spectrometer, which consists of a variable-line-spacing XUV grating, a microchannel plate, a phosphor screen and a CMOS camera.

For the experimental validation of the theoretically observed spectral tuning phenomena, the images of the CMOS camera are recorded and later processed. The results will be presented in a subsequent section. Moreover, a further flip mirror is installed before the generation gas cell by which the two half beams can be reflected towards a visible-IR spectrometer, therefore the introduced modulation in the driving laser spectrum can be monitored. The modulation can be clearly attributed to the interference of the two pulses. In this way, both the generated high-order harmonics and the produced IR spectra can be monitored.

3.3.1.3 Experimental production of double pulses

The method used to produce double pulses to drive the HHG process was different from the technique that was experimentally implemented for DP characterization, and presented already in Section 3.1.3. For HHG measurements, the DP structures were produced by a custom-made split-and-delay unit (SDU), mentioned previously in Section 2.1.3. Its schematic layout is presented in Figure 3.19, both in front (left) and back view (right). Basically, this custom-made optomechanical unit is originally designed to control temporal delay in XUV-XUV pump-probe experiments [49], through reflective optics mounted in a grazing incidence angle (> 80°), since

the XUV steering optics need to be used in such a high angle of incidence to reach the best reflectance. In contrast, I inserted mirrors into the SDU to steer broadband IR/near-IR radiation, and in the implemented configuration the incidence angle of the incoming beam was less than 5° (close to normal incidence). However, the reflectivity of the applied IR optics in case of 0° angle of incidence is still acceptable, and this configuration does not cause significant energy losses.

The SDU consists of two separately movable halves, presented by the light and dark green parts in Figure 3.19. The two halves are identical regarding their technical design, in fact, they are mirror images of each other. Both parts have three manually adjustable actuators, indicated by red and blue. In addition, the actuators shown in red are combined with high-precision piezoelectric position adjusters, with electric connections on them (small orange parts on the red actuators). Thereby the position of the motorized actuators can be adjusted with an accuracy of a few nanometres within a moving range of approximately 45 μm. Such high-accuracy piezoelectric positioners are not installed on the blue actuators, they can only be controlled manually. The grey components in Figure 3.19 are fixed elements of the SDU, and are designed to hold the movable parts and secure the whole device onto the optical table. All constituting parts of the SDU are high vacuum compatible, and because of the use of remote-controlled piezoelectric actuators, the device can be used under vacuum too.

The light blue components in Figure 3.19 represent the steering optics, which are 50.8 mm ×
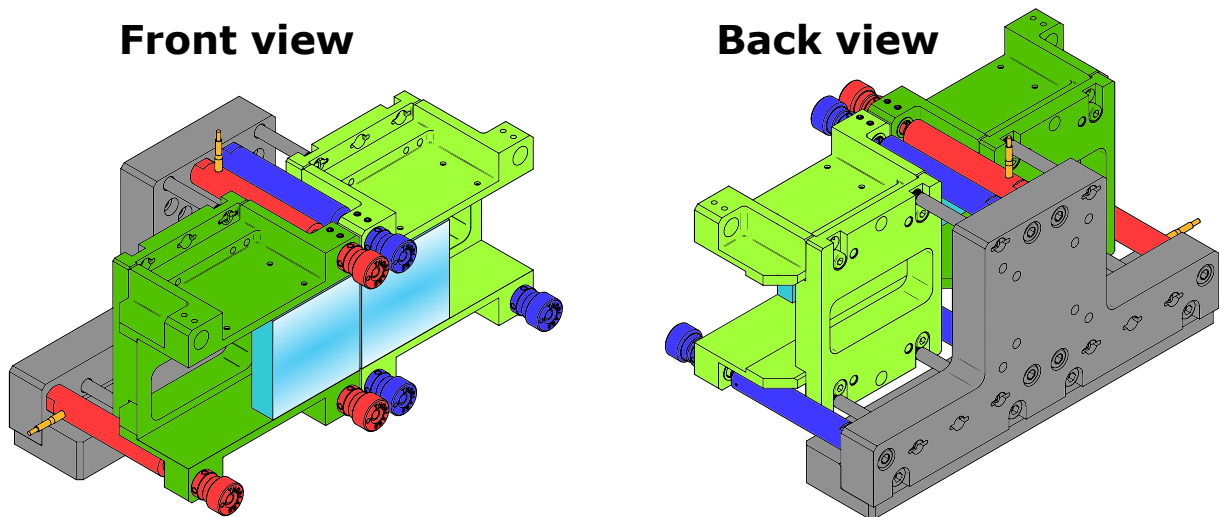
FIGURE 3.19: Front and back view of the SDU device that was used during the experiments. The grey parts are fixed components that are used to mount the device onto the optical table, and to hold the movable constituting parts of the SDU. The movable parts are the light and dark green elements which serve as the mounts of the utilized reflective optics (light blue elements) that are 50.8 mm × 50.8 mm, square-shaped protected silver mirrors. The dark blue components are manually adjustable actuators. The red elements are also actuators but they are combined with high-accuracy piezoelectric positioners, in which the small orange parts demonstrate the electrical connections.

50.8 mm, square-shaped protected silver mirrors. These optics are identical, and they are coated to reflect radiation in the wavelength range between 450 nm and 2000 nm with high reflectance. The incoming round laser beam reaches the two mirrors in a manner that it hits both optics in equal proportions. For this reason, the incident beam is reflected by both mirrors and split into two half-beams in such a way that the splitting ratio is equal or at least close to an equal split. The two half-beams propagate collinearly if the surfaces of the two mirrors are completely parallel to each other. However, the motorized half must be tilted with an amazingly tiny angle for the two half-beams to converge towards each other slightly and to overlap at a spatial point further away. The SDU device is installed in the attosecond pulse generation beamline before the focusing optics (see Figure 3.18) which focuses the beams into the XUV generation gas cell. Because of this focusing element, the two half-beams spatially overlap exactly in the focal point of the mirror, and this is where the DP structure is formed.

The temporal delay between the two pulses, or in other words, between the two half-beams can be varied by changing all three actuators to the same extent. Obviously, this can be easily performed by the motorized piezoelectric positioners (red actuators in Figure 3.19) with approximately 10 nm precision. This step size corresponds to ~ 33 as time resolution, which physically means that around 100 delay positions can be set within a full optical cycle of the applied laser electric field, since the temporal duration of a full cycle is

$$T_{1030nm} = \frac{2\pi}{\omega_0} = 3.42 fs, \tag{3.12}$$

where ω_0 = 1.836 PHz is the central angular frequency of the driving laser radiation. This specific time period can also be observed in the delay-dependent central angular frequency curve of the driving laser field, which will be presented in the following section. Consequently, this periodicity will appear in the delay scans in the double-pulse driven HHG. The validation of these results will be presented later.

3.3.1.4 Spectra of double pulses of the HR-1 laser system and their delay-dependent spectral characteristics

In the previous subsection I presented how double pulses are produced for the generation of high-order harmonics in a gas target. I dedicate this section to present the delay-dependent spectra of double pulses which are obtained both experimentally and by simulations for the sake of comparability. The spectra of experimentally produced DP structures are recorded by a visible-IR spectrometer before the generation of XUV radiation (see Figure 3.18). To theoretically calculate the spectra of double pulses, an experimentally recorded single pulse spectrum is used from which two identical laser pulses are simulated, having variable delay between them. Then, this electric field structure is inverse Fourier transformed back to the spectral domain.

The experimentally implemented delay-dependent DP spectra are demonstrated by the coloured map in Figure 3.20.(a), while the simulated ones are shown in Figure 3.20.(b) and (c), when the temporal amplitude ratios between the constituting pulses of the DP structure are R = 0.3 and 1, respectively (Eqn. 2.15). In all cases, the delay varied between –26 fs and 11 fs. This delay range was chosen because high-order harmonic generation was possible in these cases, as it will be presented in a subsequent section. The corresponding central angular frequency is calculated by using Eqn. 3.7 at each delay, and this way the delay-dependent central angular frequency ($\omega_0(\tau)$) is obtained. In case of the experimentally recorded spectra, $\omega_0(\tau)$ is shown by the grey curve in Figure 3.20.(a), while the simulated values are shown by the dotted and solid black curves in Figure 3.20.(b) and (c), by using R = 0.3 and 1 temporal amplitude ratios, respectively. One can clearly observe the periodic oscillation in each curve, with a periodicity of T_{1030nm} = 3.42 fs. It can also be clearly seen that the oscillation is more visible in case of the simulation, where R = 1 amplitude ratio is applied compared to the experimental values (or simulations with R = 0.3). The reason is that the two half-beams noncollinearly propagate, and the spatial overlap of the two beam fractions is confined only to a small region
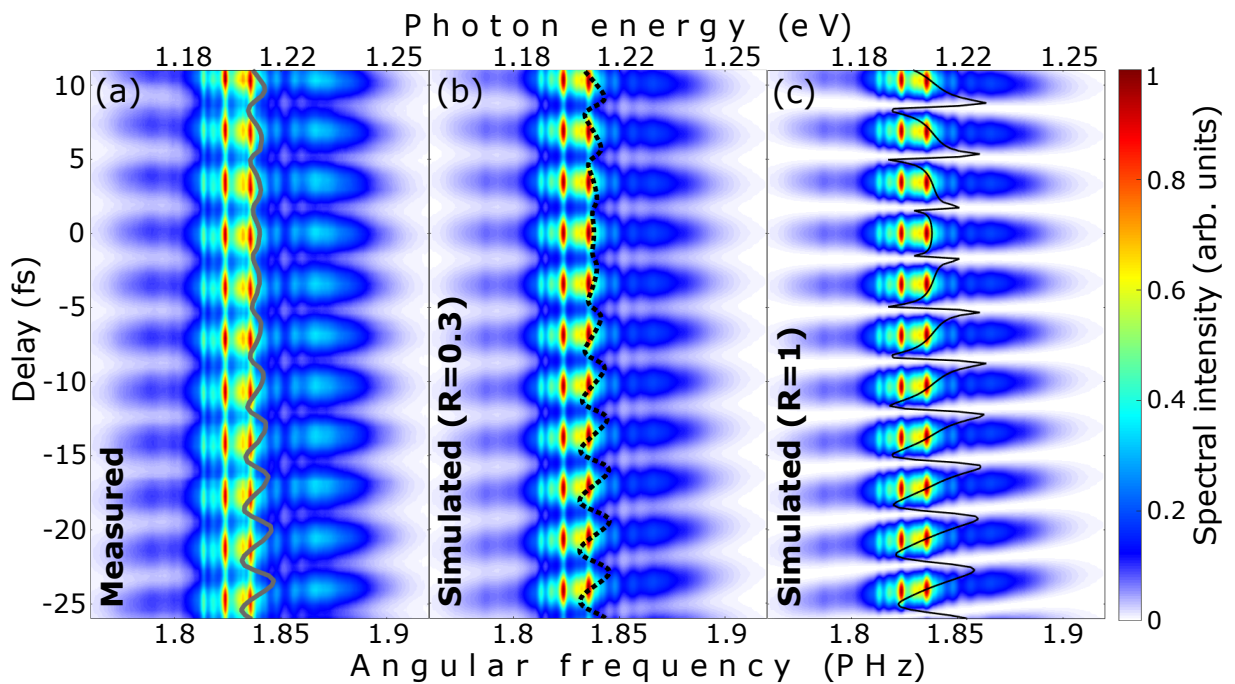
FIGURE 3.20: (a) Measured and (b), (c) simulated delay-dependent DP spectra, by applying a temporal amplitude ratio of R = 0.3 and 1 (Eqn. 2.15), respectively. To obtain the simulation results, a measured spectrum of the HR-1 laser system is utilized. The grey (a), dotted black (b), and solid black (c) curves show the delay dependence of the central angular frequency ($\omega_0(\tau)$), which is calculated by Eqn. 3.7 at each delay. One can clearly observe in each curve that by changing the delay between the constituting pulses of the DP structure, the central angular frequency oscillates around 1.836 PHz, which is the central angular frequency of a single laser spectrum that has already been presented in Figure 3.17.(a). The oscillation period is T_{1030nm} = 3.42 fs in each case.

around the focus, where the double pulses are formed. Therefore, a slight misalignment in the position of the visible-IR spectrometer can cause the two beams to enter the spectrometer neither in equal proportions, nor at the same angle of incidence. Basically, this is equivalent to the spectral interference of two laser pulses with a non-equal spectral amplitude, therefore the visibility of the spectral interferogram is smaller. The simulations reveal that the temporal amplitude ratio of the pulses entering the visible-IR spectrometer (Figure 3.18) is around 0.3. However, this does not mean that the DP structure is not formed according to the expectations. It is only due to the detection geometry of the IR spectra. Apart from this fact, the coloured maps have similar tendencies, and oscillation can be clearly observed in each $\omega_0(\tau)$ curve. The mean of the oscillating $\omega_0(\tau)$ curve is around ω_0 = 1.836 PHz in each case, which is the central angular frequency of a single laser pulse spectrum (see Figure 3.17.(a)). It is also important to mention that there are differences when comparing the black curve in Figure 3.20.(c) to the blue curve in Figure 3.12.(a), as the latter was obtained through the simulation of an ideal Gaussian spectrum. The source of the difference is the distinct shape of the spectral amplitudes, since in Section 3.2.1 a Gaussian-shape laser spectrum is assumed, while the spectral distribution of radiation from the HR-1 laser is quite far from the ideal Gaussian-shape spectral evolution. Nevertheless, the differences in $\omega_0(\tau)$ curves from the previously presented theoretical results (Section 3.2.2.1) will not affect the validation of the observed harmonic central photon energy tuning phenomena.

Similarly to the $\omega_0(\tau)$ curves, the evolution of the delay-dependent spectral bandwidth ($\Delta\omega(\tau)$) can also be determined. For this calculation, Eqn. 3.8 has to be used, in which formula ω_0 denotes the central angular frequency at delay τ in the current case. Basically, the spectral bandwidth of the laser spectra presented in Figure 3.20.(a) and (c) are calculated. The obtained spectral bandwidth variations of the HR-1 laser system are demonstrated by the orange curve with crosses in Figure 3.21.(a), and a black curve with open circles in Figure 3.21.(b) in case of simulated (R = 1) and experimentally recorded DP spectra, respectively. The two green horizontal lines indicate the region which will be investigated in more detail during the harmonic spectral bandwidth calculations. The exact laser spectral bandwidth portions which will be used for further calculations are highlighted by the solid black curves in Figure 3.21.(b). The bandwidth values at the temporal delays where the two pulses destructively interfere can be seen only in Figure 3.21.(a), since at these delays the obtained simulation results show large values for the spectral bandwidth, deteriorating the observable bandwidth evolution. Also at these delay positions, high-order harmonic generation cannot be carried out, since the temporal peak intensity is appreciably lower than necessary for the interaction to occur. These extreme bandwidth values cannot be observed in the experimentally obtained time-dependent spectral bandwidth curve in Figure 3.21.(b). By investigating the constructive interference delay positions only, the evolution of the two spectral bandwidth curves is quite similar, especially
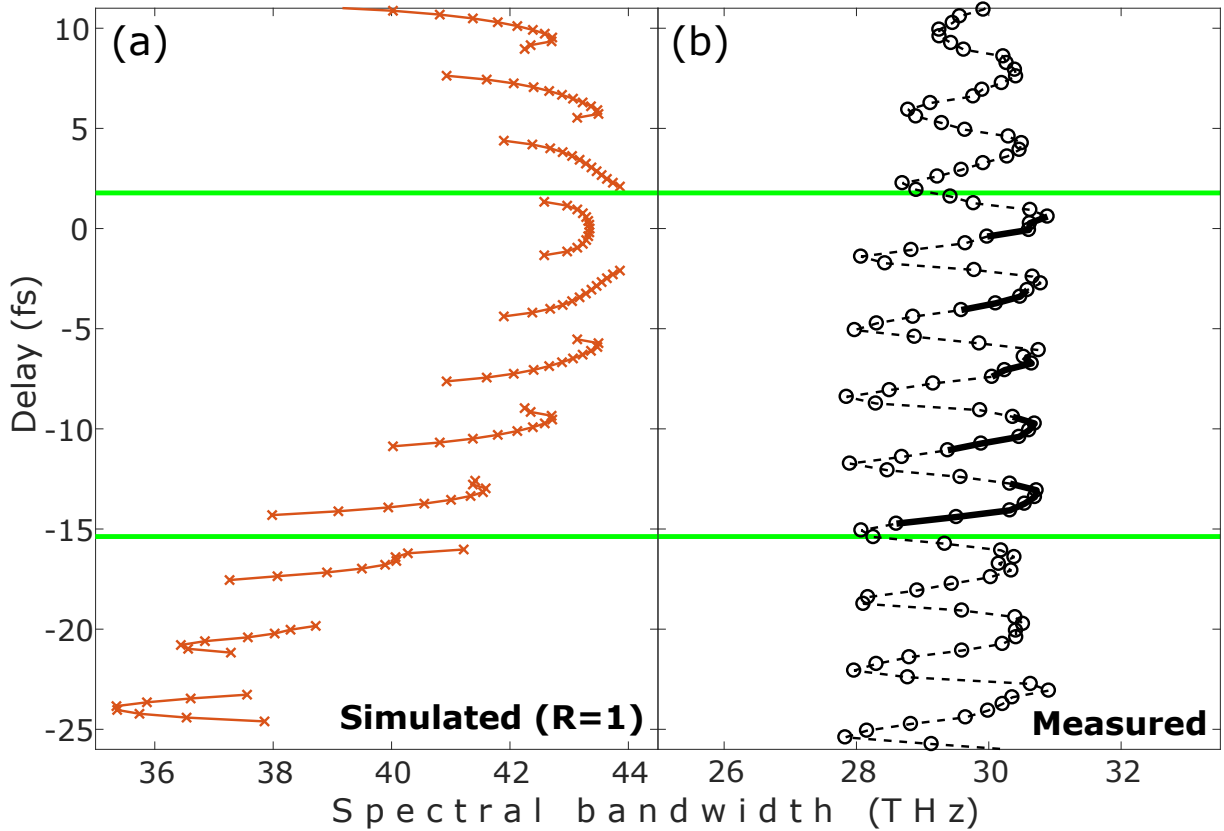
FIGURE 3.21: (a) Delay-dependent spectral bandwidth of the DP structures obtained by evaluating simulated DP spectra using a measured HR-1 laser spectrum for the calculations. The constructive interference delay positions are presented only. (b) The spectral bandwidth evolution of experimentally recorded DP spectra. The two green horizontal lines mark the region which is further investigated during the calculations of the spectral bandwidth of high-order harmonics. In figure (b) the exact laser bandwidth fractions that are utilized are indicated by solid black curves.

between the two green horizontal lines.

3.3.2   High-order harmonics generated experimentally by double pulses

In Section 3.3.1, I summarized all technical details connected to the presented experiment. I must emphasize that the evolution of the delay-dependent spectral characteristics of HR-1 laser radiation is different from the results obtained by the Gaussian-shape laser spectrum (see Section 3.2.1), however, the deviations still allow for the validation of the spectral tuning effects of high harmonics.

In this section, I will demonstrate the results of HHG with double pulses under experimental conditions. First, I will present a long delay scan, covering a time range of approximately 35 fs, where numerous harmonic peaks are generated up to the high-energy cutoff. The target gas is argon, having an ionization potential of 15.76 eV. Argon is injected into a 4-mm-long gas cell, resulting in 210 mbar static pressure at the generation point. The temporal duration

of the incoming laser pulses is close to the transform limit, so the driving pulses are 30 fs long (see Figure 3.17). Due to the loose focusing geometry, harmonics are generated only in case of the proper spatial and temporal overlap of the driving pulses, otherwise the total electric field peak intensity is not high enough to ionize any atom. To vary the delay between the constituting pulses of the DP structure, the motorized actuators of the SDU (red components in Figure 3.19) are changed with the same amount. In the current case, the step size of each piezoelectric actuator is set to 50 nm, which corresponds to ~ 167 as. This means that approximately 20 different harmonic dipole spectra are recorded in a delay range corresponding to a laser cycle. A typical temporal delay scan takes 15 minutes in the course of which the adjusted delay value can be considered as constant. However, to be able to increase the temporal resolution, or extend the time range of the scan, the actuators of the SDU must be actively stabilized to assure the spatial and temporal overlap of the pulses [49]. Otherwise the proper formation of DP structures during a time-consuming delay scan cannot be assured, since the HR-1 laser system's high energy, high-repetition-rate laser pulses, heat up the HR GHHG GAS beamline, together with the SDU device, and the overlap of the two half pulses is guaranteed neither spatially, nor temporally.

By following the experimental conditions summarized in the previous paragraph, we obtained high harmonic spectra which are presented by the coloured map in Figure 3.22. Taking into account the quickness of the performed scans, the SDU device was not stabilized. Since the temporal delay between the generating laser pulses varies, destructive and constructive
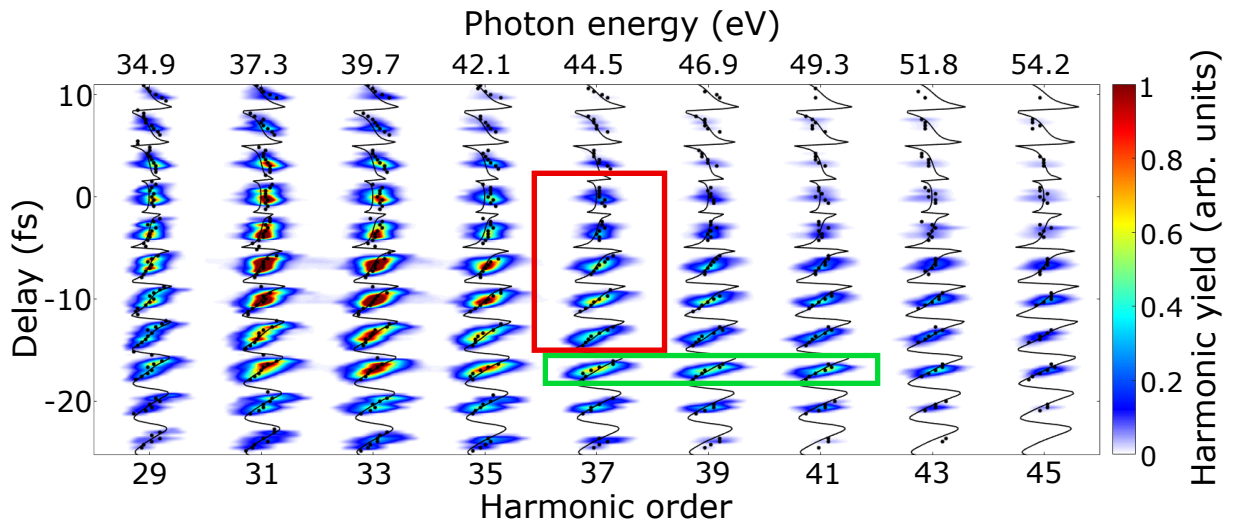
FIGURE 3.22: Experimentally generated high-order harmonic spectra as a function of time separation between the constituting pulses of the driving DP structure (coloured map). The black dots represent the exact spectral positions of the harmonic peaks. The black curves at each harmonic order show where the harmonics should appear according to upscaling the central angular frequency of the driving laser spectrum. To make this spectral position prediction, Eqn. 3.9 is utilized, and in the formula the delay-dependent central angular frequency is the black curve in Figure 3.20.(c).

interference between the pulses can also take place, therefore the total electric field peak intensity periodically falls below the ionization threshold of argon. This manifests in the generated high-order harmonic spectra, since the harmonics periodically appear and disappear as a function of delay. This effect could also be observed in the theoretical calculations (see Figure 3.13). The black dots in Figure 3.22 represent the exact spectral positions of harmonic peaks. The solid black curves at each harmonic order show the expected positions of high harmonics. The predicted harmonic central photon energy ($E_q(\tau)$) is determined by upscaling the delay-dependent central angular frequency of the driving laser spectrum, by applying Eqn. 3.9. In the utilized formula, the delay-dependent central angular frequency curve is the black curve of Figure 3.20.(c). The absolute zero delay of the recorded long scan is also determined by using this delay-dependent central angular frequency curve, which has a well-defined zero delay position. However, the delay-dependent high harmonic spectrum scan shows asymmetries around zero time separation, which could be attributed to imperfections in the produced double pulses, which strongly influence the phase-matching of the HHG process. As a matter of fact, before starting the delay scan measurement, the phase-matching conditions were optimized at a time separation where a perfect temporal overlap was assumed between the driving pulses, together with the best spatial overlap. Apart from this, one can clearly observe that there is a clear match between the black dots and black curves, which means the photon energy tuning effect of high-order harmonics is unambiguously attributable to the introduced modulation in the driving laser spectrum.

To be able to quantify the harmonic photon energy tuning effect and the modulation of the harmonic spectral bandwidth, I investigate in more detail a lower number of harmonics in a shorter delay range. These smaller ranges are presented by the green and the red quadrants in Figure 3.22, providing a deeper insight into the spectral characteristic variations of high order harmonics.

3.3.3 Experimental validation of the photon energy tuning effect

In the previous subsection, I demonstrated high-order harmonic spectra generated by double pulses by changing the time separation between the constituting pulses of the DP structure on a wide delay range. To investigate in more detail the tuning effect of XUV photon energy, a smaller region is chosen (the 37th to 41st harmonic orders in the delay range from −18.3 fs to −15.8 fs). With the time separation values in this delay range the two constituting pulses interfere constructively, resulting in a total peak intensity sufficiently high to ionize the target gas. For the sake of reference, Figure 3.23.(a) shows simulation results by utilizing the laser spectra to drive the HHG process that is presented in Figure 3.20.(c). In the calculations, 100 as step size is used for the delay scan. To obtain the harmonic dipole spectra, the single-atom model is used, similarly to the calculations in Section 3.2. By taking into account that the interaction

length is concentrated into a small region where the interfering pulses overlap spatially and temporally, the outcome of the single-atom model can be considered as valid. The intensity of each pulse is $1.2 \times 10^{14} \frac{W}{cm^2}$ and their spectral phase, including the absolute CEPs, is the same. In the simulations, the target gas is argon to match the current experimental conditions.

The corresponding region in Figure 3.22 is indicated by the green quadrant, and this region is enlarged and presented in Figure 3.23.(b). In both figures, the black curves demonstrate the expected spectral positions of high-order harmonics, which are calculated by multiplication of the delay-dependent central angular frequency curve (black curve in Figure 3.20.(c)) by using the formula of Eqn. 3.9. The black dots in Figure 3.23.(b) represent the exact spectral positions of the harmonic peaks at each delay. Both in Figures 3.23.(a) and (b) one can clearly observe that the upscaled central angular frequency curves follow the generated high-order harmonic peaks when the temporal delay between the constituting pulses of the driving DP structure changes. There is an apparent difference between the two figures: the measured harmonics are blurred compared to the simulated results. This can be attributed to macroscopic propagation effects, such as plasma generation, absorption, and dispersion, which are not taken into account during the calculations. However, without considering the propagation effects, the single-atom model gives reliable results, and these macroscopic effects do not alter the main result of this section,
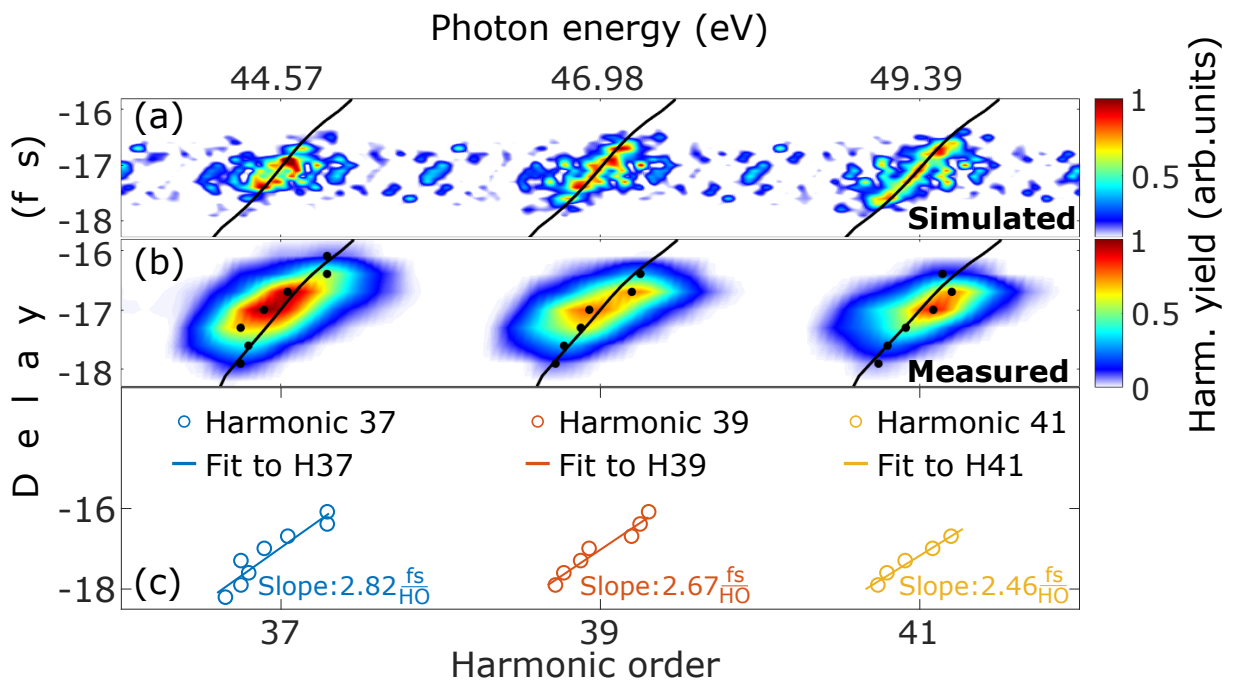
FIGURE 3.23: (a) Simulated and (b) experimentally measured high-order harmonics from the 37th to 41st harmonic order between −18.3 fs and −15.8 fs. In both figures, the black curves represent where the harmonic peaks should appear according to the central angular frequency of the driving laser. The black dots in (b) demonstrate the exact spectral positions of the measured harmonic peaks. (c) Linear fits to the spectral positions of the measured harmonic peaks in case of the 37th to 41st harmonic orders, by indicating the slopes of fits.

the spectral tunability of high-order harmonics.

To quantify the exact tuning ranges of individual harmonics, I made a linear fit to the harmonic peaks, i.e. to the black dots in Figure 3.23.(b). The fits in case of the 37th to 41st harmonic orders are demonstrated in Figure 3.23.(c). The slopes of the distinct linear fits are indicated at each investigated harmonic order. It is clear that the obtained slopes decrease with increasing harmonic order. By determining the slopes for more harmonic orders, and by calculating their reciprocals, or in other words, the $dE_q(\tau)/d\tau$ tuning parameters for each harmonic order, I get a linear increment by the increasing harmonic order, which is presented by the blue squares in Figure 3.24. To be able to make an estimation for the exact tuning ranges of different harmonic orders, a linear fit has to be made to the tuning parameter points. By assuming a delay range of $\tau_q = 2$ fs, where harmonics are visible (see Figure 3.23.(b)), the exact tuning ranges of high-order harmonics can be estimated by

$$\Delta E = \frac{dE_q(\tau)}{d\tau} \times \tau_q. \tag{3.13}$$

The obtained linear fit is presented by the orange curve in Figure 3.24, and the exact tuning ranges can be interpolated for each harmonic order (right-hand axis of Figure 3.24). It is worth mentioning that the tuning range of the highest harmonic order generated reaches almost 1100 meV. This is quite close to the central photon energy of the driving laser source, which is 1200 meV in the current experimental campaign (see Figure 3.20).

In conclusion, the photon energy tuning effect of the generated high-order harmonics in argon gas target is successfully validated. As I have presented, the maximum tuning range by using the experimental conditions summarized above is close to 1100 meV. This can be further extended by increasing the cutoff of the generated harmonic dipole spectrum, since the tuning range linearly increases with increasing harmonic order. Moreover, by applying laser pulses
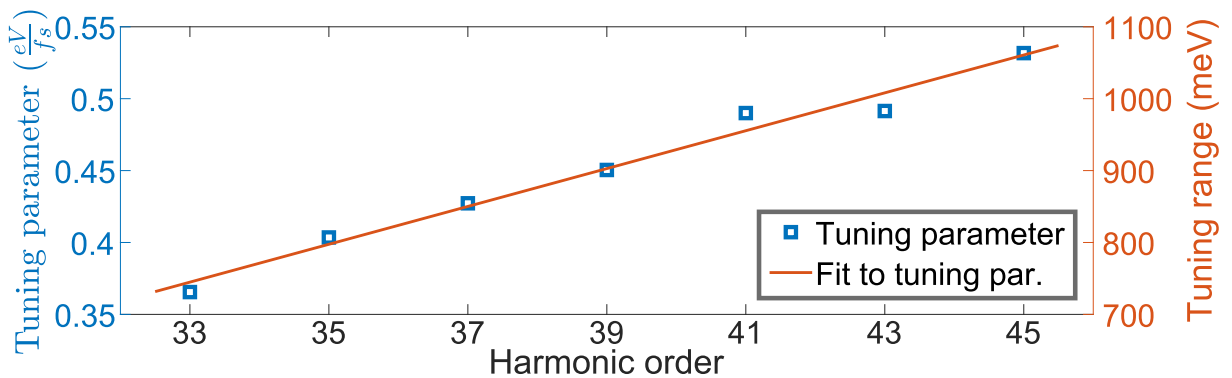
FIGURE 3.24: Calculated tuning parameters for different harmonic orders (blue squares), having $\frac{eV}{fs}$ units. By assuming a 2 fs delay range where harmonics can be observed, and by making a linear fit to the tuning parameters, the exact tuning ranges of the distinct harmonic orders can be determined, as indicated by the solid orange curve and quantified at the right-hand axis of this figure.

with shorter FWHM temporal duration to drive the HHG process, the achieved maximum tuning range can be further extended because of the broader spectrum of the driving laser. However, we must not forget the CEP effects in case of few-cycle driving pulses, therefore too short pulses are not effective to tune the photon energy of XUV sources. Nevertheless, by finding a compromise for the temporal pulse duration to give a broader spectrum but negligible CEP effects, the achieved photon energy tuning range can be fully exploited.

3.3.4 Investigation of the spectral bandwidth variation

After the successful experimental validation of photon energy control in XUV sources, I will now focus on the demonstration of the spectral bandwidth tuning effect of high-order harmonics under experimental conditions. To gain a deeper insight into the spectral bandwidth variation of high harmonics, similarly to the previous section, I choose a smaller range from the full delay scan indicated by the red quadrant in Figure 3.22, i.e. I investigate the 37th harmonic in the delay range from −15 fs to 2 fs.

The red quadrant in Figure 3.22 is enlarged and presented by the coloured map in Figure 3.25.(b). Figure 3.25.(a) shows the laser flux (blue dotted curve) from which on can deduce where the laser is intense enough to generate high-order harmonics. Moreover, the laser's spectral bandwidth (black curves with open circles) is also shown in the same figure. Both curves are calculated from the experimentally recorded double pulse spectra, produced by utilizing the HR-1 laser pulses, previously presented in Figure 3.20.(a). As a matter of fact, the laser spectral bandwidth curve is taken from Figure 3.21.(b); the solid black curves are reproduced here. Analogously to Figure 3.25.(a), subfigure (c) represents the harmonic flux (blue curve with open triangles), and the harmonic spectral bandwidth (black curves with open squares) calculated by evaluating the coloured map in Figure 3.25.(b). The evolution of the harmonic bandwidth is calculated with Eqn. 3.8, in which formula ω_0 denotes the central photon energy of the 37th harmonic at a given temporal delay, and $I(\omega)$ is the harmonic spectral intensity in the specific case. Both in case of the laser and the generated harmonics, the spectral characteristics are investigated only at the temporal delay instants where the constituting pulses of the DP structure constructively interfere, or in other words, where the harmonics are generated. By comparing the spectral bandwidth curves, one can observe a similar tendency in the evolution of the harmonic bandwidth as in the case of the delay-dependent laser bandwidth. However, in case of the laser spectral bandwidth, a spectral narrowing effect can be observed with decreasing temporal delay. On the other hand, the bandwidth evolution of the 37th harmonic oscillates approximately at around 200 meV, and such shortening effect cannot be clearly observed.

Since the spectral bandwidth evolution of the generated high-order harmonics show similarities to the laser bandwidth evolution, it can be stated without doubt that in addition to the central angular frequency, the harmonics inherit this spectral characteristic from the driving
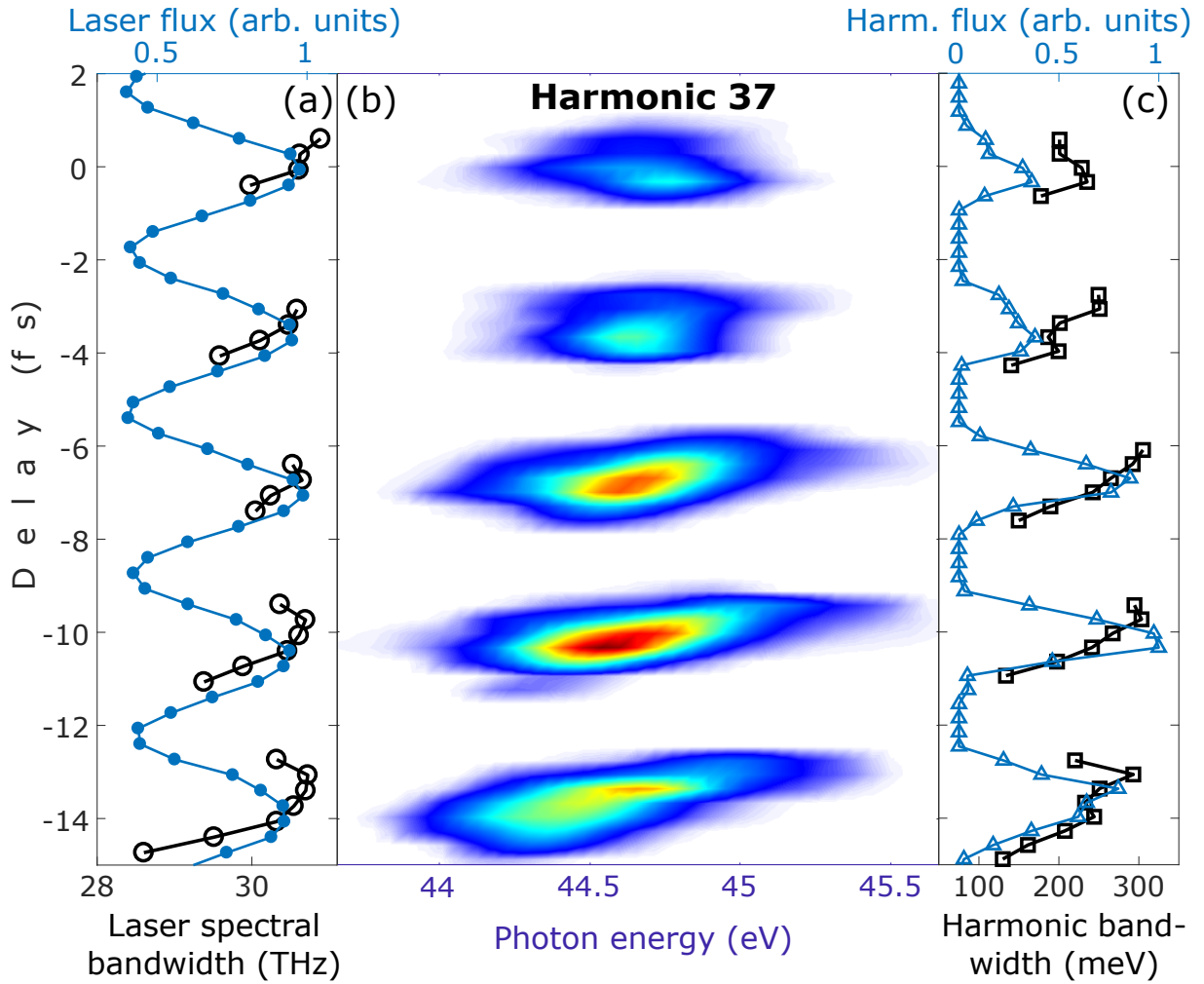
FIGURE 3.25: (a) Delay-dependent laser flux (blue dotted curve) and laser spectral bandwidth evolution (black curve with open circles). (b) The 37th harmonic generated by temporal double pulses, by changing the delay between −15 fs and 2 fs which is taken from Figure 3.22 shown by red rectangle. (c) Harmonic flux (blue curve with open triangles) calculated by utilizing Figure (b), and the harmonic spectral bandwidth by utilizing Eqn. 3.8.

laser source. I must emphasize that by increasing the harmonic order the number of contributing electron trajectories drops, therefore the higher order harmonics are less sharp. For this reason, their bandwidth evolution shows worse match with the bandwidth of the driving laser, similarly as I mentioned in Section 3.2.2.2. Moreover, apart from the fact that the spectral bandwidth evolution of the HR-1 laser source is substantially different from the bandwidth curve presented during the theoretical investigations in Section 3.2, this does not deteriorate the predicted theoretical observations.

Summary III. *I successfully produced double pulses under experimental conditions in noncollinear geometry by utilizing a custom-made split-and-delay unit. I showed that the high-order harmonics generated using these pulse structures inherit the central angular frequency from the driving laser spectrum,*

thereby the central photon energy of the harmonics can be controlled by changing the delay between the driving laser pulses. I demonstrated that the tuning range of certain harmonic orders can reach the photon energy of the fundamental laser field. Moreover, I measured that the delay-dependent spectral bandwidth of the driving laser manifests its effects in the bandwidth evolution of the generated high-order harmonics. With the measurements, I revealed that regardless of the spectral shape of a single pulse originating from the laser source, the spectral characteristics of the generated harmonics can be controlled by using double pulses [T3].

Legal notes:

Chapter 4

Summary

In this thesis I investigated the temporal characterization of ultrashort double pulses, and the impact of this double-pulse structure on the high-order harmonic generation process. The study begins with a brief Introduction, describing the everyday occurrences of electromagnetic radiation through relevant and well-known applications. This serves as the basis of the current research, since both the laser and the XUV radiations are electromagnetic waves. This section is followed by the Scientific background chapter where I describe the scientific knowledge required to understand the motivation and goal of my study. Then the new achievements of the research are detailed in the Results chapter, where both the simulation outcomes and the experimental observations are summarized. In the following, the most important scientific observations are collected point by point:

I. I have improved an already existing femtosecond laser pulse characterization technique, called SRSI to be able to reconstruct femtosecond double-pulse structures. I have shown that by manipulating the temporal interferogram, a spectral phase correction term can be extracted. The combination of this phase correction term and the originally retrieved spectral phase gives an improved final phase for complete pulse reconstruction. I verified the improved method by simulations, and I successfully reconstructed the temporal shape of experimentally produced double pulses. I determined the deviations of the retrieved spectral phases, obtained both by the original and the improved methods, from the expected spectral phase, and by this I quantitatively demonstrated the level of improvement of the technique on a wide range of amplitude ratios of double pulses [T1].

II: I have investigated theoretically the impact of the temporal double-pulse structure on the high-order harmonic generation process. I have proposed to use these electric field structures to control the spectral characteristics of the generated high-order harmonics. I have demonstrated with simulations that the central photon energy of the harmonics can be directly tuned, and that the tuning range broadens with increasing harmonic order. Moreover, I have shown that spectral narrowing of harmonics can also be achieved by increasing of the temporal delay

between the driving interfering pulses [T2].

III: I successfully produced double pulses under experimental conditions in noncollinear geometry by utilizing a custom-made split-and-delay unit. I showed that the high-order harmonics generated using these pulse structures inherit the central angular frequency from the driving laser spectrum, thereby the central photon energy of the harmonics can be controlled by changing the delay between the driving laser pulses. I demonstrated that the tuning range of certain harmonic orders can reach the photon energy of the fundamental laser field. Moreover, I measured that the delay-dependent spectral bandwidth of the driving laser manifests its effects in the bandwidth evolution of the generated high-order harmonics. With the measurements, I revealed that regardless of the spectral shape of a single pulse originating from the laser source, the spectral characteristics of the generated harmonics can be controlled by using double pulses [T3].

Chapter 5

Magyar nyelvű összefoglaló

5.1 Bevezetés

A fény nélkülözhetetlen kísérője életünknek, mégsem érinthetjük meg közvetlenül. A fénynek köszönhetően érzékeljük a tárgyakat, élőlényeket, vagy éppen embertársainkat, más szóval, hogy látunk. A fény az alapvető természeti elemek közé tartozik, akárcsak a víz vagy az oxigén, azonban ez nem létféleme életünknek. A fény valójában elektromágneses sugárzás, amelynek közvetítő részecskéi a fotonok. Az ilyen sugárzásokat legegyszerűbben a közvetítő fotonok frekvenciájával, vagy az ennek megfeleltethető hullámhosszal jellemezhetjük. Egyszerűen fogalmazva, a széles színképet lefedő elektromágneses sugárzások más és más „színű" fotonokat jelentenek, amelyek színük alapján különböző alcsoportokba sorolhatók.

Biológiai evolúciója során az emberi szem, pontosabban a retina, oly módon fejlődött, hogy csak bizonyos hullámhossztartományból képes érzékelni a fotonokat. Az elektromágneses színkép e tartományát nevezzük „látható fénynek". Szemünk a látható tartományon kívül eső sugárzásokra teljesen érzéketlen. Ez veszélyt is hordozhat magában, mivel olyan sugárzások érhetik szervezetünket, amelyekről nincs tudomásunk. Ilyen sugárzások érkezhetnek a világűrből, például a Napból is, azonban ezek elnyelődnek a Föld több mint 10 km vastagságú légkörében. Az elektromágneses sugárzások széles spektrális tartományt fednek le a néhány pikométer hullámhosszúságú kozmikus és gamma-sugaraktól, a röntgen- és látható sugárzásokon keresztül egészen a méteres hullámhosszúságú rádióhullámokig. Bár szemünk e sugárzások nagy részét nem érzékeli, számos jól ismert alkalmazási területük van. Idesorolhatók az orvosi képalkotó eszközök, a hőkamerák, a vezeték nélküli internethálózatok, vagy éppen a mobiltelefonok, amelyek mindannyiunk életének szerves részét képezik.

Elektromágneses sugárzást kibocsátó eszköz a lézer is, amely elnevezés egy angol mozaikszóból ivódott be a mindennapi szóhasználatba (Light Amplification by the Stimulated Emission of Radiation – LASER). Bár a lézerek elektromágneses hullámokat bocsátanak ki, sugárzásuk jellemzői nagyban eltérnek a korábban említett alkalmazásokétól. Emiatt széleskörű felhasználásnak örvendenek: például nyomtatókban, vonalkód leolvasó készülékekben, az autóiparban, vagy akár érrendszeri és látószervi műtétek során hasznosítják őket. A lézerfotonok

színe mellett a lézerek a kibocsátott sugárzás időbeli jellemzői alapján is osztályozhatók. Ennek alapján léteznek folytonos hullámot, vagy impulzussorozatot kibocsátó rendszerek. Míg az első csoportba tartozókat fémmegmunkálásra használják leggyakrabban, addig az impulzuslézerek legfőbb alkalmazási területe az ultragyors folyamatok kísérleti tanulmányozása, mivel az impulzusok hossza elérheti a femtoszekundumos nagyságrendet (1 fs = 10^{-15} s). Ez azt jelenti, hogy rendelkezésünkre áll a másodperc egymilliárdod részének az egymilliomod részének megfelelő hosszúságú sugárzás. Ezáltal olyan folyamatok válnak vizsgálhatóvá, mint például a töltésmozgások. Azonban figyelembe véve a fotonok színét is, a sugárzás időbeli hossza nem lehet rövidebb, mint egy teljes optikai ciklus az adott hullámhosszon, ami fizikai korlátot szab a sugárzások minimálisan elérhető időbeli hosszának.

Emiatt a tudósok kidolgoztak egy olyan módszert, az úgynevezett magasrendű felharmonikus-keltést, amellyel az ultraibolya tartományban szélessávú, koherens sugárzás állítható elő. A módszer a femtoszekundumos lézerforrásokat hasznosítja, és a meghajtó lézer sugárzásának nemlineáris frekvenciakonverzióján alapul. Így rövidebb hullámhosszú, azaz nagyobb frekvenciájú sugárzás állítható elő, mint a meghajtó lézeré, így átléphető a látható tartománybeli impulzusok időbeli hosszának korlátja. Ennek köszönhetően attoszekundum (1 as = 10^{-18} s) hosszúságú impulzusok állíthatók elő. Ez a módszer utat nyit *as* időtartam alatt lejátszódó ultragyors folyamatok, például az elektronmozgások, vagy más atomi és molekuláris folyamatok vizsgálatához.

5.2 Tudományos előzmények

A következő fejezetben részletes áttekintést adok a femtoszekundumos lézerimpulzusok legfontosabb jellemzőiről, bemutatok egy lézerimpulzus rekonstruáló módszert, és ismertetem a lézerimpulzusok egyik kísérleti alkalmazását, a magasrendű felharmonikus-keltés folyamatát.

5.2.1 Ultrarövid lézerimpulzusok leírása

Az ultrarövid lézerimpulzusok matematikai leírása során a Fourier-transzformáció adja meg a kapcsolatot a komplex elektromos tér és a komplex spektrum között. Az egyszerűbb matematikai kezelhetőség érdekében érdemes a spektrális amplitúdót pozitív és negatív frekvenciakomponensekre bontani, valamint az elektromos teret valós összefüggések felhasználásával (valós időfüggő amplitúdó és fázisfüggvény) kifejezni. A spektrális amplitúdó spektrális összetevői leggyakrabban egy jól meghatározott körfrekvencia-érték köré összpontosulnak, amelyet központi körfrekvenciának nevezünk. E körfrekvencia-érték és a komplex időbeli burkoló felhasználásával, ami a valós időbeli burkoló és az időfüggő fázissal írható fel, kifejezhető az elektromos tér. Ezáltal a lézerimpulzus elektromos terének összefüggése olyan

alakra hozható, amely matematikailag egyszerűbben kezelhető, és könnyen kiolvashatók az ultrarövid lézerimpulzusokra ható fő fizikai hatások.

Például egy lézerimpulzus időbeli alakjára ható torzító hatások a fázissal vannak szoros összefüggésben. Ezek jellemzéséhez a fázist Taylor-sorba szükséges fejteni a központi körfrekvencia körül, amely sorfejtésben az egyes fázisderiváltak mind különböző impulzustorzító hatást írnak le. Ilyen például a vivő-burkoló fázis (CEP – Carrier-Envelope Phase), ami a burkoló maximuma és az elektromos tér maximuma közötti fáziskülönbséget írja le, és a csoportkésleltetés (GD – Group Delay), amely a lézerimpulzust időben eltolja, viszont az alakját nem torzítja. Ezek közé tartozik még a csoportkésleltetés-diszperzió (GDD – Group Delay Dispersion), amely megnyújtja az impulzust és változtatja a pillanatnyi frekvenciát, valamint a harmadrendű diszperzió (TOD – Third-Order Dispersion), aminek legjelentősebb hatása, hogy mellékimpulzusokat eredményez a fő impulzus mellett, csökkenő intenzitással. Ezeket az impulzustorzító hatásokat egy hiteles kísérlet elvégzése előtt mindenképp szükséges meghatározni, különben a kívánt eredmények nem lesznek kimutathatók, vagy eltérő végeredményre juthatunk.

A fent említett impulzustorzító hatások mellett számos kísérleti alkalmazás során megjelenhetnek úgynevezett kettős impulzusok is, amelyek olykor pozitív, olykor negatív hatással vannak egy adott kísérlet végkimenetelére. Matematikai szempontból az egy impulzusra vonatkozó összefüggések alkalmazhatók rájuk. Kettős impulzusok esetében az alkotó impulzusok spektrális interferenciája miatt a spektrális amplitúdó változik a két impulzus közötti késleltetés változtatásával. Emellett, ha a késleltetés nagysága az impulzus időbeli hosszával összemérhető, akkor az impulzusok között nem csak spektrális, hanem időbeli interferencia is megfigyelhető, ami összetett intenzitáseloszlást eredményez az elektromos térerősségben.

Ilyen és hasonló intenzitáseloszlások időbeli burkolójának meghatározásához számos impulzusrekonstruáló módszer áll rendelkezésre. Közülük a legelterjedtebbek a frekvenciabontott optikai kapuzás (FROG – Frequency Resolved Optical Gating), a spektrális fázisinterferometria az elektromos tér közvetlen visszanyeréséhez (SPIDER – Spectral Phase Interferometry for Direct Electric field Reconstruction) és az önreferenciás spektrális interferometria (SRSI – Self-Referenced Spectral Interferometry) technikák. Ezek közül az SRSI módszert ismertetem részletesen a következő szakaszban, mivel az SRSI technika részletesebb bemutatása nélkülözhetetlen az eredményeim maradéktalan megértéséhez.

5.2.2 Önreferenciás spektrális interferometria

Az önreferenciás spektrális interferometria olyan impulzuskarakterizálási módszer, ami az ismeretlen impulzus méréséhez szükséges referencia-impulzust leggyakrabban keresztpolarizált hullám (XPW – Cross-Polarized Wave) keltésével állítja elő. Az XPW egy harmadrendű, frekvencia-megőrző, nemlineáris folyamat, ami különösen érzékeny a keltő impulzus polari-

zációs állapotára, ezért a mérési elrendezésnek tartalmaznia kell egy bemeneti polarizátort, ami biztosítja a lineáris polarizációt. A méréshez szükséges két impulzust egy kettőstörő ömlesztett kvarclemez állítja elő, ami után az impulzusok egymásra ortogonálisan polarizáltak, és τ késleltetés lép fel közöttük. Terjedési irányuk kollineáris. Ezután az XPW referencia-impulzus keltése egy BaF_2 kristályban történik a p-polarizált hullámmal, míg az s-polarizált hullám változatlanul keresztülhalad a kristályon. Ezt követően egy kimeneti polarizátor biztosítja, hogy a mérendő és a referencia-impulzusok azonos polarizációs állapottal rendelkezzenek. Végül a két impulzus interferencia-mintázatát, azaz a spektrális interferogramot egy széles spektrális sávszélességű spektrométerrel rögzítjük, amely interferogram magában hordozza az ismeretlen impulzus rekonstruálásához szükséges információt.

A spektrális interferogram kiértékelésének első lépése, hogy inverz Fourier-transzformáljuk a kapott jelet. Ezáltal megkapjuk az időbeli interferogramot, ami három, jól elkülöníthető csúcsból áll. Egy a 0 fs késleltetésnél, és további egy-egy a pozitív és negatív τ késleltetési értékeknél adódik. Numerikusan szűrve a 0 fs és +τ késleltetéseknél megjelenő jelet, és egyenként Fourier-transzformálva őket, mind a mérendő, mind a referencia-impulzus spektrális amplitúdója felírható a kapott jelek felhasználásával egy-egy analitikus formulában. Azonban az impulzusok maradéktalan időbeli rekonstrukciójához szükség van a spektrális fázisok meghatározására is, amit egy iterációs algoritmus segítségével nyerhetünk ki a spektrális interferogramból. Az algoritmus bemeneti változói a korábban megkapott spektrális amplitúdók. Továbbá a kezdeti fázisra szükséges egy becslést adni, ami szintén megtehető az interferogram tanulmányozásával. Az algoritmus minden ciklusban enyhén módosítja a bemeneti fázist, ami konvergál a végső fázishoz, majd néhány iterációt követően a végső spektrális fázis kinyerhető, ami szükséges az impulzus teljes időbeli rekonstrukciójához.

Azonban ez az iteratív algoritmus pontatlanul nyeri vissza a kettős impulzus struktúrához tartozó spektrális fázist, mivel ebben az esetben a fázis hirtelen fázisugrásokat, vagy akár szakadásokat tartalmaz azoknál a pontoknál, ahol a spektrális amplitúdó zérusra csökken a két impulzus spektrális interferenciája miatt. Ez nem folytonos spektrális fázist eredményez, amelynek meghatározása kihívást jelent a fázist kinyerő iteratív algoritmus számára.

5.2.3 Magasrendű felharmonikus-keltés

Ahogyan azt már a Bevezetés részben említettem, a magasrendű felharmonikusok keltéséhez (HHG – High-order Harmonic Generation) femtoszekundum hosszúságú impulzusokat kibocsátó lézereket alkalmaznak. A folyamat során a meghajtó lézer sugárzásának nemlineáris frekvenciakonverziója történik, ezáltal szélessávú, koherens, extrém ultraibolya sugárzás állítható elő. Az előállított sugárzás spektrumában a keltő lézer spektrumának páratlan számú többszörösei jelennek meg a folyamat szimmetria-tulajdonságai miatt. Ezeket a spektrális csúcsokat nevezzük harmonikusoknak, amelyek a spektrumban egyenlő, adott fotonenergiával

jellemezhető távolságra helyezkednek el egymástól. Távolságuk a keltő lézer központi frekvenciájának kétszerese, ezért a harmonikusok központi fotonenergiája nem változtatható önkényesen és egyszerűen, mivel ezt a tulajdonságot a meghajtó lézer határozza meg.

A HHG folyamatot legegyszerűbben a háromlépcsős modell segítségével érthetjük meg. A modell három egyszerű lépésben írja le a harmonikusok keltésének folyamatát: (1) Első lépésben a feltételezett atomi Coulomb-potenciál alakját az erős lézertér oly módon torzítja, hogy az addig kötött, azaz egy potenciálvölgyben elhelyezkedő elektron képes alagutazás útján szabaddá válni. Ezáltal az elektron mozgására az atomi potenciál már nincs hatással, a mozgást csak a lézer elektromos tere befolyásolja. (2) A lézertér az elektront gyorsítja, és mozgása során energiát nyer a tértől. A tér irányának megfordulásával az elektron mozgása az ionizált mag felé irányul. (3) A maghoz közeledve az elektron újra egyesül az ionizált atommaggal, majd ezzel egyidejűleg a lézer terétől szerzett többletenergiát egy nagy energiájú ultraibolya foton formájában kisugározza. Ez a három lépés a meghajtó lézertér minden félciklusában megtörténik, amelyek végeredménye a szélessávú extrém ultraibolya sugárzás. A HHG folyamat legfőbb tulajdonságai a háromlépcsős modellel jól szemléltethetők, és a harmonikus spektrum főbb jellemzői egyszerűen magyarázhatók. A harmonikus-keltés alaposabb vizsgálatához azonban kvantummechanikai megközelítés szükséges.

Ahhoz, hogy a kvantummechanikai hatásokat tárgyalni tudjuk, az időfüggő Schrödinger-egyenletet kell megoldani. Azonban ennek numerikus megoldása nem egyszerű, a számolás még egydimenziós modellt feltételezve is rendkívül időigényes. A számolások jelentősen egyszerűsíthetők az úgynevezett erős tér közelítés alkalmazásával, ami a következő feltételezéseket jelenti: (i) A lézer-anyag kölcsönhatás során a gerjesztett állapotok hozzájárulása elhanyagolható, és csak az atom alapállapota játszik szerepet az ionizációs folyamatban. (ii) Az alapállapotú elektronok energiaszintjének populációja kimeríthetetlennek tekinthető. (iii) A kiszakított elektron szabad részecskeként vizsgálható, és csak a lézertér hat a mozgására. A Coulomb-potenciál hatása ekkor elhanyagolható. E közelítéseket alkalmazva analitikusan felírható az egyatomi dipól spektrum, amelyet Lewenstein és munkatársai vezettek be először, ezért Lewenstein integrálnak nevezünk. A Lewenstein integrál könnyen kiszámítható, így a HHG folyamat a kvantummechanikai jelenségek figyelembevételével is tanulmányozható.

5.3 Eredmények

I. Egy korábban kifejlesztett femtoszekundumos impulzuskarakterizálási módszert, az SRSI technikát fejlesztettem tovább oly módon, hogy rekonstruálhassuk a femtoszekundumos kettős impulzusokat. Megmutattam, hogy az időbeli interferogram manipulálásával egy korrekciós tagot kaphatunk a spektrális fázis pontosabb meghatározásához. A kinyert fáziskorrekciós tag és az eredeti algoritmussal kapott fázis kombinálásával egy pontosabb spektrális fázis nyerhető a teljes impulzusrekonstrukcióhoz. A javított módszer pontosságát szimulációkon keresztül ellenőriztem, valamint sikeresen rekonstruáltam a kísérleti úton előállított kettős impulzusok időbeli alakját. Továbbá meghatároztam az eredeti algoritmus és a javított módszer által szolgáltatott eredmények eltérését a várt spektrális fázistól, amellyel kvantitatív módon megmutattam a technika javulásának mértékét széles amplitúdótartományt vizsgálva [T1].

II: Elméleti síkon vizsgáltam a kettős impulzus struktúra hatását a magasrendű felharmonikus-keltés folyamatára. Javasoltam ezen elektromos tér felhasználását a magasrendű felharmonikusok spektrális jellemzőinek szabályozására. A számolásokkal bemutattam, hogy a harmonikusok központi fotonenergiája közvetlenül hangolható, és hogy az energiahangolási tartomány szélesedik növekvő harmonikus renddel. Ezenkívül megmutattam, hogy a keltett felharmonikusok spektrális beszűkülése elérhető a két interferáló meghajtó impulzus közötti késleltetés növelésével [T2].

III: Sikeresen állítottam elő kísérletileg kettős impulzusokat nem kollineáris elrendezésben egy egyedi gyártású osztó-késleltető elem felhasználásával. Megmutattam, hogy az előállított elektromos térrel generált magasrendű felharmonikusok öröklik a keltő lézer spektrumának központi körfrekvenciájának változásait, ezáltal a magasrendű felharmonikusok központi fotonenergiája szabályozható a két meghajtó lézerimpulzus közötti késleltetés változtatásával. Bemutattam, hogy egyes felharmonikusok hangolási tartománya elérheti a meghajtó lézertér fotonjainak fotonenergia-értékét. Ezenkívül a méréseimmel kimutattam, hogy a keltő lézer késleltetésfüggő spektrális sávszélessége megjelenik a generált magasrendű felharmonikusok spektrális sávszélességének alakulásában. A méréseimmel rávilágítottam arra, hogy a lézerforrásból származó egyetlen impulzus spektrális alakjától függetlenül a generált harmonikusok spektrális jellemzői kettős impulzusok alkalmazásával szabályozhatók [T3].

Acknowledgement

When approaching the end of a long-term research project, I am obliged to express my gratitude to all those people who contributed to the achievement of my goals, and supported me –– everyone in their own way —, both during my research and in the process of dissertation writing.

First of all, I would like to thank my supervisor, Balázs Major, who significantly contributed to this study with his useful and valuable comments, and whose guidance let me find the best way to reach my scientific goals.

This thesis could not have been written without my current and former colleagues. Therefore, my special thanks go to Tamás Csizmadia and Peng Ye, who helped me extensively in conducting my experiments. Furthermore, I am very grateful to Tímea Grósz, Zoltán Filus, Massimo De Marco, Harshitha Nandiga Gopalakrishna and Miklós Füle, who contributed to these results through our valuable discussions.

At last but not least, I must thank my family, who did not contribute scientifically to my research, but without their mental support and the joyful hours spent together my work would have been much more stressful. In addition, I am indebted to my friends, who occasionally made me forget about my tasks, at least for short periods of time, and let me recharge my batteries. Furthermore, I am grateful to my girlfriend, who supported me in every way, and without whom writing the dissertation would have been much more tiresome.

Köszönetnyilvánítás

Egy hosszan tartó kutatás végéhez közeledve elengedhetetlennek tartom, hogy kifejezzem hálámat mindazoknak, akik hozzájárultak céljaim eléréséhez és támogattak – ki-ki a maga módján – akár a kutatásaim, akár az értekezésem megírása alatt.

Elsősorban szeretném megköszönni témavezetőmnek, Major Balázsnak, hogy hasznos és értékes megjegyzéseivel jelentősen hozzájárult a tanulmány megszületéséhez, valamint útmutatásaival segített abban, hogy megtaláljam a legjobb utat a tudományos céljaim eléréséhez.

A jelen tanulmány nem jöhetett volna létre jelenlegi és korábbi munkatársaim nélkül, ezért kiemelt köszönet illeti Csizmadia Tamást és Peng Ye-t, akik rengeteget segítettek a kísérleteim elvégzése során. Nagyon hálás vagyok Grósz Tímeának, Filus Zoltánnak, Massimo De Marcónak, Harshitha Nandiga Gopalakrishnanak és Füle Miklósnak is, akik értékes beszélgetések útján szintén jelentősen hozzájárultak az eredmények megszületéséhez.

Végül, de nem utolsósorban, köszönetet szeretnék mondani családtagjaimnak, akik tudományosan ugyan nem járultak hozzá a kutatáshoz, azonban mentális támogatásuk és a velük töltött örömteli órák miatt a munka sokkal kevésbé volt megterhelő. Ezenkívül hálás vagyok a barátaimnak, akik lehetőséget adtak arra, hogy (rövid időszakokra) félretegyem a feladataimat és feltöltődhessem. Köszönettel tartozom a barátnőmnek is, aki mindenben mellettem állt és támogatott. Nélküle az értekezés írásával töltött időszak sokkal fárasztóbb lett volna.

Bibliography

[1] J. Rothhardt, S. Hädrich, J. C. Delagnes, E. Cormier, and J. Limpert, "High average power near-infrared few-cycle lasers," *Laser Photonics Rev.*, vol. 11, no. 4, p. 1 700 043, 2017. DOI: 10.1002/lpor.201770041.

[2] R. Paschotta, *Encyclopedia of Laser Physics and Technology*. Aug. 2008, vol. 1. [Online]. Available: https://www.rp-photonics.com/encyclopedia.html.

[3] A. Borzsonyi, A. P. Kovacs, and K. Osvay, "What we can learn about ultrashort pulses by linear optical methods," *Appl. Sci.*, vol. 3, no. 2, pp. 515–544, 2013. DOI: 10.3390/app3020515.

[4] C. Iaconis and I. A. Walmsley, "Spectral phase interferometry for direct electric-field reconstruction of ultrashort optical pulses," *Opt. Lett.*, vol. 23, no. 10, pp. 792–794, 1998. DOI: 10.1364/OL.23.000792.

[5] R. Trebino and D. J. Kane, "Using phase retrieval to measure the intensity and phase of ultrashort pulses: Frequency-resolved optical gating," *J. Opt. Soc. Am. A*, vol. 10, no. 5, pp. 1101–1111, 1993. DOI: 10.1364/JOSAA.10.001101.

[6] T. Oksenhendler, S. Coudreau, N. Forget, V. Crozatier, S. Grabielle, R. Herzog, O. Gobert, and D. Kaplan, "Self-referenced spectral interferometry," *Appl. Phys. B*, vol. 99, no. 1, pp. 7–12, 2010. DOI: 10.1007/s00340-010-3916-y.

[7] F. Krausz and M. Ivanov, "Attosecond physics," *Rev. Mod. Phys.*, vol. 81, pp. 163–234, 1 2009. DOI: 10.1103/RevModPhys.81.163.

[8] P. B. Corkum, "Plasma perspective on strong field multiphoton ionization," *Phys. Rev. Lett.*, vol. 71, pp. 1994–1997, 13 1993. DOI: 10.1103/PhysRevLett.71.1994.

[9] A. Nayak, M. Dumergue, S. Kühn, S. Mondal, T. Csizmadia, N. Harshitha, M. Füle, M. Upadhyay Kahaly, B. Farkas, B. Major, V. Szaszkó-Bogár, P. Földi, S. Majorosi, N. Tsatrafyllis, E. Skantzakis, L. Neoričić, M. Shirozhan, G. Vampa, K. Varjú, P. Tzallas, G. Sansone, D. Charalambidis, and S. Kahaly, "Saddle point approaches in strong field physics and generation of attosecond pulses," *Phys. Rep.*, vol. 833, pp. 1–52, 2019. DOI: 10.1016/j.physrep.2019.10.002.

[10] M. Lewenstein, P. Balcou, M. Y. Ivanov, A. L'Huillier, and P. B. Corkum, "Theory of high-harmonic generation by low-frequency laser fields," *Phys. Rev. A*, vol. 49, pp. 2117–2132, 3 1994. DOI: 10.1103/PhysRevA.49.2117.

[11] G. Sansone, E. Benedetti, F. Calegari, C. Vozzi, L. Avaldi, R. Flammini, L. Poletto, P. Villoresi, C. Altucci, R. Velotta, S. Stagira, S. De Silvestri, and M. Nisoli, "Isolated single-cycle attosecond pulses," *Science*, vol. 314, no. 5798, pp. 443–446, 2006. DOI: 10.1126/science.1132838.

[12] A. E. Siegman, *Lasers*. University Science Books, 1986, vol. 1, pp. 1–1283. [Online]. Available: https://www.osapublishing.org/books/bookshelf/lasers.cfm.

[13] E. Nava-Palomares, F. Acosta-Barbosa, S. Camacho-López, and M. Fernández-Guasti, "Femtosecond laser cavity characterization," vol. 2, 2012, pp. 1–38. DOI: 10.5772/50174.

[14] J.-C. Diels and W. Rudolph, *Ultrashort Laser Pulse Phenomena*. Academic Press, 2006, vol. 1, pp. 1–680. [Online]. Available: https://www.sciencedirect.com/book/9780122154935/ultrashort-laser-pulse-phenomena.

[15] B. E. A. Saleh and M. C. Teich, *Fundamentals of photonics*, 2nd edition. Wiley Online Library, 2007, vol. 1, pp. 1–1201. [Online]. Available: https://onlinelibrary.wiley.com/doi/book/10.1002/0471213748.

[16] Y. Cui, Y.-q. Gao, Z.-x. Zhao, Z.-y. Xu, N. An, D.-w. Li, J.-w. Yu, T. Wang, G. Xu, W.-x. Ma, and Y.-p. Dai, "Spectral phase effects and control requirements of coherent beam combining for ultrashort ultrahigh intensity laser systems," *Appl. Opt.*, vol. 55, no. 35, pp. 10 124–10 132, 2016. DOI: 10.1364/AO.55.010124.

[17] T. Grósz, A. P. Kovács, M. Kiss, and R. Szipőcs, "Measurement of higher order chromatic dispersion in a photonic bandgap fiber: Comparative study of spectral interferometric methods," *Appl. Opt.*, vol. 53, no. 9, pp. 1929–1937, 2014. DOI: 10.1364/AO.53.001929.

[18]   S. W. Jolly, F. Ahr, K. Ravi, N. H. Matlis, F. X. Kärtner, and A. R. Maier, "On the effect of third-order dispersion on phase-matched terahertz generation via interfering chirped pulses," *Opt. Express*, vol. 27, no. 24, pp. 34 769–34 787, 2019. DOI: 10.1364/OE.27.034769.

[19]   D. N. Schimpf, E. Seise, J. Limpert, and A. Tünnermann, "The impact of spectral modulations on the contrast of pulses of nonlinear chirped-pulse amplification systems," *Opt. Express*, vol. 16, no. 14, pp. 10 664–10 674, 2008. DOI: 10.1364/OE.16.010664.

[20]   L. E. Chipperfield, J. S. Robinson, J. W. G. Tisch, and J. P. Marangos, "Ideal waveform to generate the maximum possible electron recollision energy for any given oscillation period," *Phys. Rev. Lett.*, vol. 102, p. 063 003, 6 2009. DOI: 10.1103/PhysRevLett.102.063003.

[21]   H.-W. Sun, P.-C. Huang, Y.-H. Tzeng, J.-T. Huang, C. D. Lin, C. Jin, and M.-C. Chen, "Extended phase matching of high harmonic generation by plasma-induced defocusing," *Optica*, vol. 4, no. 8, pp. 976–981, 2017. DOI: 10.1364/OPTICA.4.000976.

[22]   A. Dienes, J. P. Heritage, C. Jasti, and M. Y. Hong, "Femtosecond optical pulse amplification in saturated media," *J. Opt. Soc. Am. B*, vol. 13, no. 4, pp. 725–734, 1996. DOI: 10.1364/JOSAB.13.000725.

[23]   R. Paschotta, "Modeling of ultrashort pulse amplification with gain saturation," *Opt. Express*, vol. 25, no. 16, pp. 19 112–19 116, 2017. DOI: 10.1364/OE.25.019112.

[24]   D. Wolfgang, *Laser Spectroscopy*, 4th edition. Springer, 2008, vol. 1, pp. 1–457. [Online]. Available: https://www.springer.com/gp/book/9783540734185.

[25]   H. C. Kapteyn, M. M. Murnane, A. Szoke, and R. W. Falcone, "Prepulse energy suppression for high-energy ultrashort pulses using self-induced plasma shuttering," *Opt. Lett.*, vol. 16, no. 7, pp. 490–492, 1991. DOI: 10.1364/OL.16.000490.

[26]   C. Thaury, F. Quéré, J.-P. G. A. Levy, T. Ceccotti, P. Monot, M. Bougeard, F. Réau, P. D'oliveira, P. Audebert, R. Marjoribanks, and P. Martin, "Plasma mirrors for ultrahigh-intensity optics," *Nat. Phys.*, vol. 3, no. 6, pp. 424–429, 2007. DOI: 10.1038/nphys595.

[27]   A. A. Andreev, J. Limpouch, A. B. Iskakov, and H. Nakano, "Enhancement of x-ray line emission from plasmas produced by short high-intensity laser double pulses," *Phys. Rev. E*, vol. 65, p. 026 403, 2 2002. DOI: 10.1103/PhysRevE.65.026403.

[28]   B. A. Nechay, U. Siegner, M. Achermann, H. Bielefeldt, and U. Keller, "Femtosecond pump-probe near-field optical microscopy," *Rev. Sci. Instrum.*, vol. 70, no. 6, pp. 2758–2764, 1999. DOI: 10.1063/1.1149841.

[29]   S. Yoon, D. W. McCamant, P. Kukura, R. A. Mathies, D. Zhang, and S.-Y. Lee, "Dependence of line shapes in femtosecond broadband stimulated raman spectroscopy on pump-probe time delay," *J. Chem. Phys.*, vol. 122, no. 2, p. 024 505, 2005. DOI: 10.1063/1.1828044.

[30]   V. Engel, "Femtosecond pump/probe experiments and ionization: The time dependence of the total ion signal," *Chemical Physics Letters*, vol. 178, no. 1, pp. 130–134, 1991. DOI: 10.1016/0009-2614(91)85064-4.

[31]   J. K. Freericks, H. R. Krishnamurthy, and T. Pruschke, "Theoretical description of time - resolved photoemission spectroscopy: Application to pump - probe experiments," *Phys. Rev. Lett.*, vol. 102, p. 136 401, 13 2009. DOI: 10.1103/PhysRevLett.102.136401.

[32]   H. Yoneda, H. Morikami, K.-i. Ueda, and R. M. More, "Ultrashort-pulse laser ellipsometric pump-probe experiments on gold targets," *Phys. Rev. Lett.*, vol. 91, p. 075 004, 7 2003. DOI: 10.1103/PhysRevLett.91.075004.

[33]   C. Daniel, J. Full, L. González, C. Lupulescu, J. Manz, A. Merli, Š. Vajda, and L. Wöste, "Deciphering the reaction dynamics underlying optimal control laser fields," *Science*, vol. 299, no. 5606, pp. 536–539, 2003. DOI: 10.1126/science.1078517.

[34]   J. A. Pérez-Hernández, D. J. Hoffmann, A. Zäir, L. E. Chipperfield, L. Plaja, C. Ruiz, J. P. Marangos, and L. Roso, "Extension of the cut-off in high-harmonic generation using two delayed pulses of the same colour," *J. Phys. B: At. Mol. Opt. Phys.*, vol. 42, p. 134 004, 2009. DOI: 10.1088/0953-4075/42/13/134004/meta.

[35]   P. Raith, C. Ott, C. P. Anderson, A. Kaldun, K. Meyer, M. Laux, Y. Zhang, and T. Pfeifer, "Fractional high-order harmonic combs and energy tuning by attosecond-precision split-spectrum pulse control," *Appl. Phys. Lett.*, vol. 100, p. 121 104, 2012. DOI: 10.1063/1.4827194.

[36]   L. J. Salazar-Serrano, D. Janner, N. Brunner, V. Pruneri, and J. P. Torres, "Measurement of sub-pulse-width temporal delays via spectral interference induced by weak value amplification," *Phys. Rev. A*, vol. 89, p. 012 126, 1 2014. DOI: 10.1103/PhysRevA.89.012126.

[37] L. J. Salazar-Serrano, A. Valencia, and J. P. Torres, "Observation of spectral interference for any path difference in an interferometer," *Opt. Lett.*, vol. 39, no. 15, pp. 4478–4481, 2014. DOI: `10.1364/OL.39.004478`.

[38] M. Wollenhaupt, A. Assion, D. Liese, C. Sarpe-Tudoran, T. Baumert, S. Zamith, M. A. Bouchene, B. Girard, A. Flettner, U. Weichmann, and G. Gerber, "Interferences of ultrashort free electron wave packets," *Phys. Rev. Lett.*, vol. 89, p. 173 001, 17 2002. DOI: `10.1103/PhysRevLett.89.173001`.

[39] E. Goulielmakis, G. Nersisyan, N. Papadogiannis, D. Charalambidis, G. Tsakiris, and K. Witte, "A dispersionless michelson interferometer for the characterization of attosecond pulses," *Appl. Phys. B*, vol. 74, pp. 197–206, 3 2002. DOI: `10.1007/s003400200794`.

[40] W. Schweinberger, L. Vamos, J. Xu, S. A. Hussain, C. Baune, S. Rode, and I. Pupeza, "Interferometric delay tracking for low-noise mach-zehnder-type scanning measurements," *Opt. Express*, vol. 27, no. 4, pp. 4789–4798, 2019. DOI: `10.1364/OE.27.004789`.

[41] F. Fraggelakis, G. Giannuzzi, C. Gaudiuso, I. Manek-Hönninger, G. Mincuzzi, A. Ancona, and R. Kling, "Double- and multi-femtosecond pulses produced by birefringent crystals for the generation of 2d laser-induced structures on a stainless steel surface," *Materials*, vol. 12, no. 8, pp. 1996–1944, 2019. DOI: `10.3390/ma12081257`.

[42] S. Zhou, D. Ouzounov, H. Li, I. Bazarov, B. Dunham, C. Sinclair, and F. W. Wise, "Efficient temporal shaping of ultrashort pulses with birefringent crystals," *Appl. Opt.*, vol. 46, no. 35, pp. 8488–8492, 2007. DOI: `10.1364/AO.46.008488`.

[43] C. Sarpe, J. Köhler, T. Winkler, M. Wollenhaupt, and T. Baumert, "Real-time observation of transient electron density in water irradiated with tailored femtosecond laser pulses," *New J. Phys.*, vol. 14, no. 7, p. 075 021, 2012. DOI: `10.1088/1367-2630/14/7/075021`.

[44] B. Bai, C. Zhou, E. Dai, and J. Zheng, "Generation of double pulses in-line by using reflective dammann gratings," *Optik (Stuttg.)*, vol. 119, no. 2, pp. 74–80, 2008. DOI: `10.1016/j.ijleo.2006.07.002`.

[45] F. Frank, C. Arrell, T. Witting, W. A. Okell, J. McKenna, J. S. Robinson, C. A. Haworth, D. Austin, H. Teng, I. A. Walmsley, J. P. Marangos, and J. W. G. Tisch, "Invited review article: Technology for attosecond science," *Rev. Sci. Instrum.*, vol. 83, no. 7, p. 071 101, 2012. DOI: `10.1063/1.4731658`.

[46] M. Reduzzi, J. Hummert, A. Dubrouil, F. Calegari, M. Nisoli, F. Frassetto, L. Poletto, S. Chen, M. Wu, M. B. Gaarde, K. Schafer, and G. Sansone, "Polarization control of absorption of virtual dressed states in helium," *Phys. Rev. A*, vol. 92, p. 033 408, 3 2015. DOI: `10.1103/PhysRevA.92.033408`.

[47] Y. Mairesse, A. de Bohan, L. J. Frasinski, H. Merdji, L. C. Dinu, P. Monchicourt, P. Breger, M. Kovačev, R. Taïeb, B. Carré, H. G. Muller, P. Agostini, and P. Salières, "Attosecond synchronization of high-harmonic soft x-rays," *Science*, vol. 302, no. 5650, pp. 1540–1543, 2003. DOI: `10.1126/science.1090277`.

[48] S. Bonora, D. Brida, P. Villoresi, and G. Cerullo, "Ultrabroadband pulse shaping with a push-pull deformable mirror," *Opt. Express*, vol. 18, no. 22, pp. 23 147–23 152, 2010. DOI: `10.1364/OE.18.023147`.

[49] F. Campi, H. Coudert-Alteirac, M. Miranda, L. Rading, B. Manschwetus, P. Rudawski, A. L'Huil-lier, and P. Johnsson, "Design and test of a broadband split-and-delay unit for attosecond xuv-xuv pump-probe experiments," *Rev. Sci. Instrum.*, vol. 87, no. 2, p. 023 106, 2016. DOI: `10.1063/1.4941722`.

[50] F. Verluise, V. Laude, Z. Cheng, C. Spielmann, and P. Tournois, "Amplitude and phase control of ultrashort pulses by use of an acousto-optic programmable dispersive filter: Pulse compression and shaping," *Opt. Lett.*, vol. 25, no. 8, pp. 575–577, 2000. DOI: `10.1364/OL.25.000575`.

[51] A. M. Weiner, "Ultrafast optical pulse shaping: A tutorial review," *Opt. Commun.*, vol. 284, no. 15, pp. 3669–3692, 2011. DOI: `https://doi.org/10.1016/j.optcom.2011.03.084`.

[52] P. Tournois, "Acousto-optic programmable dispersive filter for adaptive compensation of group delay time dispersion in laser systems," *Opt. Commun.*, vol. 140, no. 4, pp. 245–249, 1997. DOI: `10.1016/S0030-4018(97)00153-3`.

[53] I. H. Malitson, "Interspecimen comparison of the refractive index of fused silica," *J. Opt. Soc. Am.*, vol. 55, no. 10, pp. 1205–1209, 1965. DOI: `10.1364/JOSA.55.001205`.

[54] G. Ghosh, "Dispersion-equation coefficients for the refractive index and birefringence of calcite and quartz crystals," *Opt. Commun.*, vol. 163, no. 1, pp. 95–102, 1999. DOI: `10.1016/S0030-4018(99)00091-7`.

[55] K. Osvay, P. Dombi, A. P. Kovács, and Z. Bor, "Fine tuning of the higher-order dispersion of a prismatic pulse compressor," *Appl. Phys. B*, vol. 75, no. 6, pp. 649–654, 2002. DOI: 10.1007/s00340-002-1021-6.

[56] A. Börzsönyi, Z. Heiner, M. P. Kalashnikov, A. P. Kovács, and K. Osvay, "Dispersion measurement of inert gases and gas mixtures at 800 nm," *Appl. Opt.*, vol. 47, no. 27, pp. 4856–4863, 2008. DOI: 10.1364/AO.47.004856.

[57] J. Odhner and R. J. Levis, "Direct phase and amplitude characterization of femtosecond laser pulses undergoing filamentation in air," *Opt. Lett.*, vol. 37, no. 10, pp. 1775–1777, 2012. DOI: 10.1364/OL.37.001775.

[58] A. Blättermann, C. Ott, A. Kaldun, T. Ding, V. Stooß, M. Laux, M. Rebholz, and T. Pfeifer, "In situ characterization of few-cycle laser pulses in transient absorption spectroscopy," *Opt. Lett.*, vol. 40, no. 15, pp. 3464–3467, 2015. DOI: 10.1364/OL.40.003464.

[59] H. M. Crespo, T. Witting, M. Canhota, M. Miranda, and J. W. G. Tisch, "In situ temporal measurement of ultrashort laser pulses at full power during high-intensity laser–matter interactions," *Optica*, vol. 7, no. 8, pp. 995–1002, 2020. DOI: 10.1364/OPTICA.398319.

[60] M. A. Galle, W. Mohammed, L. Qian, and P. W. E. Smith, "Single-arm three-wave interferometer for measuring dispersion of short lengths of fiber," *Opt. Express*, vol. 15, no. 25, pp. 16 896–16 908, 2007. DOI: 10.1364/OE.15.016896.

[61] A. Börzsönyi, A. Kovács, M. Görbe, and K. Osvay, "Advances and limitations of phase dispersion measurement by spectrally and spatially resolved interferometry," *Opt. Commun.*, vol. 281, no. 11, pp. 3051–3061, 2008. DOI: 10.1016/j.optcom.2008.02.002.

[62] A. P. Kovács, K. Osvay, G. Kurdi, M. Görbe, J. Klebniczki, and Z. Bor, "Dispersion control of a pulse stretcher– compressor system with two-dimensional spectral interferometry," *Appl. Phys. B*, vol. 80, no. 2, pp. 165–170, 2005. DOI: 10.1007/s00340-004-1706-0.

[63] J.-C. M. Diels, J. J. Fontaine, I. C. McMichael, and F. Simoni, "Control and measurement of ultrashort pulse shapes (in amplitude and phase) with femtosecond accuracy," *Appl. Opt.*, vol. 24, no. 9, pp. 1270–1282, 1985. DOI: 10.1364/AO.24.001270.

[64] D. J. Kane and R. Trebino, "Characterization of arbitrary femtosecond pulses using frequency-resolved optical gating," *IEEE J. Quantum Electron.*, vol. 29, no. 2, pp. 571–579, 1993. DOI: 10.1109/3.199311.

[65] K. W. DeLong, R. Trebino, J. Hunter, and W. E. White, "Frequency-resolved optical gating with the use of second-harmonic generation," *J. Opt. Soc. Am. B*, vol. 11, no. 11, pp. 2206–2215, 1994. DOI: 10.1364/JOSAB.11.002206.

[66] R. C. Miller, "Optical second harmonic generation in piezoelectric crystals," *Appl. Phys. Lett.*, vol. 5, no. 1, pp. 17–19, 1964. DOI: 10.1063/1.1754022.

[67] S. Linden, H. Giessen, and J. Kuhl, "XFROG — a new method for amplitude and phase characterization of weak ultrashort pulses," *Phys. Status Solidi A*, vol. 206, no. 1, pp. 119–124, 1998. DOI: 10.1002/(SICI)1521-3951(199803)206:1<119::AID-PSSB119>3.0.CO;2-X.

[68] C. C. Wang and G. W. Racette, "Measurement of parametric gain accompanying optical difference frequency generation," *Appl. Phys. Lett.*, vol. 6, no. 8, pp. 169–171, 1965. DOI: 10.1063/1.1754219.

[69] P. Baum, S. Lochbrunner, and E. Riedle, "Zero-additional-phase spider: Full characterization of visible and sub-20-fs ultraviolet pulses," *Opt. Lett.*, vol. 29, no. 2, pp. 210–212, 2004. DOI: 10.1364/OL.29.000210.

[70] T. H. Jeys, A. A. Brailove, and A. Mooradian, "Sum frequency generation of sodium resonance radiation," *Appl. Opt.*, vol. 28, no. 13, pp. 2588–2591, 1989. DOI: 10.1364/AO.28.002588.

[71] T. S. Clement, A. J. Taylor, and D. J. Kane, "Single-shot measurement of the amplitude and phase of ultrashort laser pulses in the violet," *Opt. Lett.*, vol. 20, no. 1, pp. 70–72, 1995. DOI: 10.1364/OL.20.000070.

[72] K. W. DeLong, R. Trebino, and D. J. Kane, "Comparison of ultrashort-pulse frequency-resolved-optical-gating traces for three common beam geometries," *J. Opt. Soc. Am. B*, vol. 11, no. 9, pp. 1595–1608, 1994. DOI: 10.1364/JOSAB.11.001595.

[73] D. J. Kane and R. Trebino, "Single-shot measurement of the intensity and phase of an arbitrary ultrashort pulse by using frequency-resolved optical gating," *Opt. Lett.*, vol. 18, no. 10, pp. 823–825, 1993. DOI: 10.1364/OL.18.000823.

[74] D. J. Kane, A. J. Taylor, R. Trebino, and K. W. DeLong, "Single-shot measurement of the intensity and phase of a femtosecond uv laser pulse with frequency-resolved optical gating," *Opt. Lett.*, vol. 19, no. 14, pp. 1061–1063, 1994. DOI: 10.1364/OL.19.001061.

[75] B. Kohler, V. V. Yakovlev, K. R. Wilson, J. Squier, K. W. DeLong, and R. Trebino, "Phase and intensity characterization of femtosecond pulses from a chirped-pulse amplifier by frequency-resolved optical gating," *Opt. Lett.*, vol. 20, no. 5, pp. 483–485, 1995. DOI: 10.1364/OL.20.000483.

[76] B. Richman, K. DeLong, and R. Trebino, "Temporal characterization of the stanford mid-ir fel micropulses by "frog"," *Nucl. Instrum. Methods Phys. Res. Sec. A*, vol. 358, no. 1, pp. 268–271, 1995. DOI: 10.1016/0168-9002(94)01488-4.

[77] J. N. Sweetser, D. N. Fittinghoff, and R. Trebino, "Transient-grating frequency-resolved optical gating," *Opt. Lett.*, vol. 22, no. 8, pp. 519–521, 1997. DOI: 10.1364/OL.22.000519.

[78] M. Li, J. P. Nibarger, C. Guo, and G. N. Gibson, "Dispersion-free transient-grating frequency-resolved optical gating," *Appl. Opt.*, vol. 38, no. 24, pp. 5250–5253, 1999. DOI: 10.1364/AO.38.005250.

[79] T. Tsang, M. A. Krumbügel, K. W. DeLong, D. N. Fittinghoff, and R. Trebino, "Frequency-resolved optical-gating measurements of ultrashort pulses using surface third-harmonic generation," *Opt. Lett.*, vol. 21, no. 17, pp. 1381–1383, 1996. DOI: 10.1364/OL.21.001381.

[80] J. Hyyti, E. Escoto, and G. Steinmeyer, "Third-harmonic interferometric frequency-resolved optical gating," *J. Opt. Soc. Am. B*, vol. 34, no. 11, pp. 2367–2375, 2017. DOI: 10.1364/JOSAB.34.002367.

[81] M. Rhodes, G. Steinmeyer, and R. Trebino, "Standards for ultrashort-laser-pulse-measurement techniques and their consideration for self - referenced spectral interferometry," *Appl. Opt.*, vol. 53, no. 16, pp. D1–D11, 2014. DOI: 10.1364/AO.53.0000D1.

[82] X. Shen, P. Wang, J. Liu, T. Kobayashi, and R. Li, "Self-referenced spectral interferometry for femtosecond pulse characterization," *Appl. Sci.*, vol. 7, no. 4, pp. 1–22, 2017. DOI: 10.3390/app7040407.

[83] N. Minkovski, G. I. Petrov, S. M. Saltiel, O. Albert, and J. Etchepare, "Nonlinear polarization rotation and orthogonal polarization generation experienced in a single-beam configuration," *J. Opt. Soc. Am. B*, vol. 21, no. 9, pp. 1659–1664, 2004. DOI: 10.1364/JOSAB.21.001659.

[84] A. Jullien, L. Canova, O. Albert, D. Boschetto, L. Antonucci, Y. H. Cha, J. P. Rousseau, P. Chaudet, G. Chériaux, J. Etchepare, S. Kourtev, N. Minkonvski, and S. M. Saltiel, "Spectral broadening and pulse duration reduction during cross-polarized wave generation: Influence of the quadratic spectral phase," *Appl. Phys.B*, vol. 87, no. 4, pp. 595–601, 2007. DOI: 10.1007/s00340-007-2685-8.

[85] S. Grabielle, A. Moulet, N. Forget, V. Crozatier, S. Coudreau, R. Herzog, T. Oksenhendler, C. Cornaggia, and O. Gobert, "Self-referenced spectral interferometry cross-checked with spider on sub-15fs pulses," *Nucl. Instrum. Methods Phys. Res. Sec. A*, vol. 653, no. 1, pp. 121–125, 2011. DOI: 10.1016/j.nima.2011.01.007.

[86] E. J. Brown, Q. Zhang, and M. Dantus, "Femtosecond transient-grating techniques: Population and coherence dynamics involving ground and excited states," *J. Chem. Phys.*, vol. 110, no. 12, pp. 5772–5788, 1999. DOI: 10.1063/1.478476.

[87] J. Liu, F. J. Li, Y. L. Jiang, C. Li, Y. X. Leng, T. Kobayashi, R. X. Li, and Z. Z. Xu, "Transient-grating self-referenced spectral interferometry for infrared femtosecond pulse characterization," *Opt. Lett.*, vol. 37, no. 23, pp. 4829–4831, 2012. DOI: 10.1364/OL.37.004829.

[88] J. Liu, K. Okamura, Y. Kida, and T. Kobayashi, "Temporal contrast enhancement of femtosecond pulses by a self-diffraction process in a bulk kerr medium," *Opt. Exp.*, vol. 18, no. 21, pp. 22 245–22 254, 2010. DOI: 10.1364/OE.18.022245.

[89] J. Liu, Y. Jiang, T. Kobayashi, R. Li, and Z. Xu, "Self-referenced spectral interferometry based on self-diffraction effect," *J. Opt. Soc. Am. B*, vol. 29, no. 1, pp. 29–34, 2012. DOI: 10.1364/JOSAB.29.000029.

[90] B. Seifert and H. Stolz, "A method for unique phase retrieval of ultrafast optical fields," *Meas. Sci. Technol.*, vol. 20, no. 1, p. 015 303, 2008. DOI: 10.1088/0957-0233/20/1/015303.

[91] V. V. Lozovoy, I. Pastirk, and M. Dantus, "Multiphoton intrapulse interference. iv. ultrashort laser pulse spectral phase characterization and compensation," *Opt. Lett.*, vol. 29, no. 7, pp. 775–777, 2004. DOI: 10.1364/OL.29.000775.

[92] A. Borot and F. Quéré, "Spatio-spectral metrology at focus of ultrashort lasers: A phase-retrieval approach," *Opt. Express*, vol. 26, no. 20, pp. 26 444–26 461, 2018. DOI: 10.1364/OE.26.026444.

[93] M. Miranda, C. L. Arnold, T. Fordell, F. Silva, B. Alonso, R. Weigand, A. L'Huillier, and H. Crespo, "Characterization of broadband few-cycle laser pulses with the d-scan technique," *Opt. Express*, vol. 20, no. 17, pp. 18 732–18 743, 2012. DOI: 10.1364/OE.20.018732.

[94] P. Wnuk, H. Fuest, M. Neuhaus, L. Loetscher, S. Zherebtsov, E. Riedle, Z. Major, and M. Kling, "Discrete dispersion scanning as a simple method for broadband femtosecond pulse characterization," *Opt. Express*, vol. 24, no. 16, pp. 18 551–18 558, 2016. DOI: 10.1364/OE.24.018551.

[95] L. Gallmann, D. Sutter, N. Matuschek, G. Steinmeyer, and U. Keller, "Techniques for the characterization of sub-10-fs optical pulses: A comparison," *Appl Phys. B*, vol. 70, no. 1, S67–S75, 2000. DOI: 10.1007/s003400000307.

[96] G. Stibenz and G. Steinmeyer, "Optimizing spectral phase interferometry for direct electric-field reconstruction," *Rev. Sci. Instrum.*, vol. 77, no. 7, p. 073 105, 2006. DOI: 10.1063/1.2221511.

[97] Y. Cai, Z. Chen, X. Zeng, H. Shangguan, X. Lu, Q. Song, Y. Ai, S. Xu, and J. Li, "The development of the temporal measurements for ultrashort laser pulses," *Appl. Sci.*, vol. 10, no. 21, p. 7401, 2020. DOI: 10.3390/app10217401.

[98] L. Gallmann, D. H. Sutter, N. Matuschek, G. Steinmeyer, U. Keller, C. Iaconis, and I. A. Walmsley, "Characterization of sub-6-fs optical pulses with spectral phase interferometry for direct electric-field reconstruction," *Opt. Lett.*, vol. 24, no. 18, pp. 1314–1316, 1999. DOI: 10.1364/OL.24.001314.

[99] M. E. Anderson, T. Witting, and I. A. Walmsley, "Gold-spider: Spectral phase interferometry for direct electric field reconstruction utilizing sum-frequency generation from a gold surface," *J. Opt. Soc. Am. B*, vol. 25, no. 6, A13–A16, 2008. DOI: 10.1364/JOSAB.25.000A13.

[100] A. Kwok, L. Jusinski, M. Krumbiigel, J. Sweetser, D. Fittinghoff, and R. Trebino, "Frequency-resolved optical gating using cascaded second-order nonlinearities," *IEEE J. Sel. Top. Quantum Electron.*, vol. 4, no. 2, pp. 271–277, 1998. DOI: 10.1109/2944.686732.

[101] R. Trebino, K. W. DeLong, D. N. Fittinghoff, J. N. Sweetser, M. A. Krumbügel, B. A. Richman, and D. J. Kane, "Measuring ultrashort laser pulses in the time-frequency domain using frequency-resolved optical gating," *Rev. Sci. Instrum.*, vol. 68, no. 9, pp. 3277–3295, 1997. DOI: 10.1063/1.1148286.

[102] A. Baltuska, M. Pshenichnikov, and D. Wiersma, "Second-harmonic generation frequency-resolved optical gating in the single-cycle regime," *IEEE J. Quantum Electron.*, vol. 35, no. 4, pp. 459–478, 1999. DOI: 10.1109/3.753651.

[103] T. C. Wong and R. Trebino, "Recent developments in experimental techniques for measuring two pulses simultaneously," *Appl. Sci.*, vol. 3, no. 1, pp. 299–313, 2013. DOI: 10.3390/app3010299.

[104] T. Kanai, S. Minemoto, and H. Sakai, "Quantum interference during high-order harmonic generation from aligned molecules," *Nature*, vol. 435, no. 7041, pp. 470–474, 2005. DOI: 10.1038/nature03577.

[105] K. Schiessl, K. L. Ishikawa, E. Persson, and J. Burgdörfer, "Quantum path interference in the wavelength dependence of high-harmonic generation," *Phys. Rev. Lett.*, vol. 99, p. 253 903, 25 2007. DOI: 10.1103/PhysRevLett.99.253903.

[106] A. Zaïr, M. Holler, A. Guandalini, F. Schapper, J. Biegert, L. Gallmann, U. Keller, A. S. Wyatt, A. Monmayrant, I. A. Walmsley, E. Cormier, T. Auguste, J. P. Caumes, and P. Salières, "Quantum path interferences in high-order harmonic generation," *Phys. Rev. Lett.*, vol. 100, p. 143 902, 14 2008. DOI: 10.1103/PhysRevLett.100.143902.

[107] E. Goulielmakis, M. Schultze, M. Hofstetter, V. S. Yakovlev, J. Gagnon, M. Uiberacker, A. L. Aquila, E. M. Gullikson, D. T. Attwood, R. Kienberger, F. Krausz, and U. Kleineberg, "Single-cycle nonlinear optics," *Science*, vol. 320, no. 5883, pp. 1614–1617, 2008, ISSN: 0036-8075. DOI: 10.1126/science.1157846.

[108] F. Ferrari, F. Calegari, M. Lucchini, C. Vozzi, S. Stagira, G. Sansone, and M. Nisoli, "High-energy isolated attosecond pulses generated by above-saturation few-cycle fields," *Nat. Photonics*, vol. 4, pp. 875–879, 12 2010. DOI: 10.1038/nphoton.2010.250.

[109] T. Oksenhendler, P. Bizouard, O. Albert, S. Bock, and U. Schramm, "High dynamic, high resolution and wide range single shot temporal pulse contrast measurement," *Opt. Express*, vol. 25, no. 11, pp. 12 588–12 600, 2017. DOI: 10.1364/OE.25.012588.

[110] A. Trabattoni, T. Oksenhendler, H. Jousselin, G. Tempea, S. De Silvestri, G. Sansone, F. Calegari, and M. Nisoli, "Self-referenced spectral interferometry for single-shot measurement of sub-5-fs pulses," *Rev. Sci. Instrum.*, vol. 86, no. 11, p. 113 106, 2015. DOI: 10.1063/1.4936289.

[111] A. Trisorio, S. Grabielle, M. Divall, N. Forget, and C. P. Hauri, "Self-referenced spectral interferometry for ultrashort infrared pulse characterization," *Opt. Lett.*, vol. 37, no. 14, pp. 2892–2894, 2012. DOI: 10.1364/OL.37.002892.

[112] A. Moulet, S. Grabielle, C. Cornaggia, N. Forget, and T. Oksenhendler, "Single-shot, high-dynamic-range measurement of sub-15 fs pulses by self-referenced spectral interferometry," *Opt. Lett.*, vol. 35, no. 22, pp. 3856–3858, 2010. DOI: 10.1364/OL.35.003856.

[113] T. Oksenhendler, "Self-referenced spectral interferometry theory," *Arxiv*, 2012. [Online]. Available: https://arxiv.org/abs/1204.4949.

[114] A. Jullien, O. Albert, F. Burgy, G. Hamoniaux, J.-P. Rousseau, J.-P. Chambaret, G. Chériaux, F. Augé-Rochereau, J. Etchepare, N. Minkovski, and S. M. Saltiel, "10^{-10} temporal contrast for femtosecond ultraintense lasers by cross-polarized wave generation," *Opt. Lett.*, vol. 30, no. 8, pp. 920–922, 2005. DOI: 10.1364/OL.30.000920.

[115] A. Jullien, S. Kourtev, O. Albert, G. Chériaux, J. Etchepare, N. Minkovski, and S. Saltiel, "Highly efficient temporal cleaner for femtosecond pulses based on cross-polarized wave generation in a dual crystal scheme," *Appl. Phys. B*, vol. 84, no. 3, pp. 409–414, 2006. DOI: 10.1007/s00340-006-2334-7.

[116] S. Yang, X. Xie, M. Sun, X. Liang, Z. Cui, P. Zhu, X. Zhang, Y. Zhang, Y. Zhang, and J. Zhu, "Characterization of spectral broadening and contrast enhancement in cross-polarized wave generation based on gadolinium gallium garnet crystal," *Appl. Phys. Express*, vol. 13, no. 3, p. 032 010, 2020. DOI: 10.35848/1882-0786/ab7320.

[117] G. Achazi and A. Cannizzo, "Fourier transform spectral interferometry with non-phase stable setups by broadband single shot detection of fs and ps pulses," *Rev. Sci. Instrum.*, vol. 88, no. 8, p. 083 110, 2017. DOI: 10.1063/1.4998989.

[118] L. Lepetit, G. Chériaux, and M. Joffre, "Linear techniques of phase measurement by femtosecond spectral interferometry for applications in spectroscopy," *J. Opt. Soc. Am. B*, vol. 12, no. 12, pp. 2467–2474, 1995. DOI: 10.1364/JOSAB.12.002467.

[119] R. W. Gerchberg and W. O. Saxton, "A practical algorithm for the determination of phase from image and diffraction plane pictures," *Optik*, vol. 35, pp. 237–246, 1972.

[120] J. S. Liu and M. R. Taghizadeh, "Iterative algorithm for the design of diffractive phase elements for laser beam shaping," *Opt. Lett.*, vol. 27, no. 16, pp. 1463–1465, 2002. DOI: 10.1364/OL.27.001463.

[121] D. Keusters, H.-S. Tan, P. O'Shea, E. Zeek, R. Trebino, and W. S. Warren, "Relative-phase ambiguities in measurements of ultrashort pulses with well-separated multiple frequency components," *J. Opt. Soc. Am. B*, vol. 20, no. 10, pp. 2226–2237, 2003. DOI: 10.1364/JOSAB.20.002226.

[122] M. Rhodes, G. Steinmeyer, J. Ratner, and R. Trebino, "Pulse-shape instabilities and their measurement," *Laser Photonics Rev.*, vol. 7, no. 4, pp. 557–565, 2013. DOI: 10.1002/lpor.201200102.

[123] M. Rhodes, Z. Guang, and R. Trebino, "Unstable and multiple pulsing can be invisible to ultrashort pulse measurement techniques," *Appl. Sci.*, vol. 7, no. 1, 2017. DOI: 10.3390/app7010040.

[124] K. W. DeLong and R. Trebino, "Improved ultrashort pulse-retrieval algorithm for frequency-resolved optical gating," *J. Opt. Soc. Am. A*, vol. 11, no. 9, pp. 2429–2437, 1994. DOI: 10.1364/JOSAA.11.002429.

[125] D. J. Kane, "Principal components generalized projections: A review [invited]," *J. Opt. Soc. Am. B*, vol. 25, no. 6, A120–A132, 2008. DOI: 10.1364/JOSAB.25.00A120.

[126] E. M. Kosik, A. S. Radunsky, I. A. Walmsley, and C. Dorrer, "Interferometric technique for measuring broadband ultrashort pulses at the sampling limit," *Opt. Lett.*, vol. 30, no. 3, pp. 326–328, 2005. DOI: 10.1364/OL.30.000326.

[127] T. Schibli, O. Kuzucu, J.-W. Kim, E. Ippen, J. Fujimoto, F. Kaertner, V. Scheuer, and G. Angelow, "Toward single-cycle laser systems," *IEEE J. Quantum Electron.*, vol. 9, no. 4, pp. 990–1001, 2003. DOI: 10.1109/JSTQE.2003.819108.

[128] K. Ursula, "Recent developments in compact ultrafast lasers," *Nature*, vol. 424, pp. 831–838, 2003. DOI: 10.1038/nature01938.

[129] P. Salières, A. L'Huillier, and M. Lewenstein, "Coherence control of high-order harmonics," *Phys. Rev. Lett.*, vol. 74, pp. 3776–3779, 19 1995. DOI: 10.1103/PhysRevLett.74.3776.

[130] T. T. Luu, Z. Yin, A. Jain, T. Gaumnitz, Y. Pertot, J. Ma, and H. J. Wörner, "Extreme–ultraviolet high–harmonic generation in liquids," *Nat. Commun.*, vol. 9, no. 1, p. 3723, 2018. DOI: 10.1038/s41467-018-06040-4.

[131] S. Ghimire, A. D. DiChiara, E. Sistrunk, P. Agostini, L. F. DiMauro, and D. A. Reis, "Observation of high-order harmonic generation in a bulk crystal," *Nat. Phys.*, vol. 7, no. 2, pp. 138–141, 2011. DOI: 10.1038/nphys1847.

[132] G. Vampa, C. R. McDonald, G. Orlando, D. D. Klug, P. B. Corkum, and T. Brabec, "Theoretical analysis of high-harmonic generation in solids," *Phys. Rev. Lett.*, vol. 113, p. 073 901, 7 2014. DOI: 10.1103/PhysRevLett.113.073901.

[133] M. Ferray, A. L'Huillier, X. F. Li, L. A. Lompre, G. Mainfray, and C. Manus, "Multiple-harmonic conversion of 1064 nm radiation in rare gases," *J. Phys. B: At. Mol. Opt. Phys.*, vol. 21, no. 3, pp. L31–L35, 1988. DOI: 10.1088/0953-4075/21/3/001.

[134] P. Antoine, A. L'Huillier, and M. Lewenstein, "Attosecond pulse trains using high–order harmonics," *Phys. Rev. Lett.*, vol. 77, pp. 1234–1237, 7 1996. DOI: 10.1103/PhysRevLett.77.1234.

[135] I. P. Christov, M. M. Murnane, and H. C. Kapteyn, "High-harmonic generation of attosecond pulses in the "single-cycle" regime," *Phys. Rev. Lett.*, vol. 78, pp. 1251–1254, 7 1997. DOI: 10.1103/PhysRevLett.78.1251.

[136] M. Schultze, A. Wirth, I. Grguras, M. Uiberacker, T. Uphues, A. Verhoef, J. Gagnon, M. Hofstetter, U. Kleineberg, E. Goulielmakis, and F. Krausz, "State-of-the-art attosecond metrology," *J. Electron Spectrosc. Relat. Phenom.*, vol. 184, no. 3, pp. 68–77, 2011. DOI: 10.1016/j.elspec.2011.01.003.

[137] S. Kühn, M. Dumergue, S. Kahaly, S. Mondal, M. Füle, T. Csizmadia, B. Farkas, B. Major, Z. Várallyay, E. Cormier, M. Kalashnikov, F. Calegari, M. Devetta, F. Frassetto, E. Månsson, L. Poletto, S. Stagira, C. Vozzi, M. Nisoli, P. Rudawski, S. Maclot, F. Campi, H. Wikmark, C. L. Arnold, C. M. Heyl, P. Johnsson, A. L'Huillier, R. Lopez-Martens, S. Haessler, M. Bocoum, F. Boehle, A. Vernier, G. Iaquaniello, E. Skantzakis, N. Papadakis, C. Kalpouzos, P. Tzallas, F. Lépine, D. Charalambidis, K. Varjú, K. Osvay, and G. Sansone, "The ELI-ALPS facility: The next generation of attosecond sources," *J. Phys. B: At. Mol. Opt. Phys*, vol. 50, no. 13, p. 132 002, 2017. DOI: 10.1088/1361-6455/aa6ee8.

[138] N. Kanda, T. Imahoko, K. Yoshida, A. Tanabashi, A. Amani Eilanlou, Y. Nabekawa, T. Sumiyoshi, M. Kuwata-Gonokami, and K. Midorikawa, "Opening a new route to multiport coherent xuv sources via intracavity high-order harmonic generation," *Light Sci. Appl.*, vol. 9, no. 1, p. 168, 2020. DOI: 10.1038/s41377-020-00405-5.

[139] T. Gaumnitz, A. Jain, Y. Pertot, M. Huppert, I. Jordan, F. Ardana-Lamas, and H. J. Wörner, "Streaking of 43-attosecond soft-x-ray pulses generated by a passively cep-stable mid-infrared driver," *Opt. Express*, vol. 25, no. 22, pp. 27 506–27 518, 2017. DOI: 10.1364/OE.25.027506.

[140] S. Mikaelsson, J. Vogelsang, C. Guo, I. Sytcevich, A.-L. Viotti, F. Langer, Y.-C. Cheng, S. Nandi, W. Jin, A. Olofsson, R. Weissenbilder, J. Mauritsson, A. L'Huillier, M. Gisselbrecht, and C. L. Arnold, "A high-repetition rate attosecond light source for time-resolved coincidence spectroscopy," *Nanophotonics*, vol. 10, no. 1, pp. 117–128, 2021. DOI: 10.1515/nanoph-2020-0424.

[141] K. J. Schafer, B. Yang, L. F. DiMauro, and K. C. Kulander, "Above threshold ionization beyond the high harmonic cutoff," *Phys. Rev. Lett.*, vol. 70, pp. 1599–1602, 11 1993. DOI: 10.1103/PhysRevLett.70.1599.

[142] K. Varjú, P. Johnsson, J. Mauritsson, A. L'Huillier, and R. López-Martens, "Physics of attosecond pulses produced via high harmonic generation," *Am. J. Phys.*, vol. 77, no. 5, pp. 389–395, 2009. DOI: 10.1119/1.3086028.

[143] A. L'Huillier, M. Lewenstein, P. Salières, P. Balcou, M. Y. Ivanov, J. Larsson, and C. G. Wahlström, "High-order harmonic-generation cutoff," *Phys. Rev. A*, vol. 48, R3433–R3436, 5 1993. DOI: 10.1103/PhysRevA.48.R3433.

[144] C. Vozzi, M. Negro, F. Calegari, S. Stagira, K. Kovács, and V. Tosa, "Phase-matching effects in the generation of high-energy photons by mid-infrared few-cycle laser pulses," *New J. Phys.*, vol. 13, no. 7, p. 073 003, 2011. DOI: 10.1088/1367-2630/13/7/073003.

[145] A. D. Shiner, C. Trallero-Herrero, N. Kajumba, H.-C. Bandulet, D. Comtois, F. Légaré, M. Giguè-re, J. Kieffer, P. B. Corkum, and D. M. Villeneuve, "Wavelength scaling of high harmonic generation efficiency," *Phys. Rev. Lett.*, vol. 103, p. 073 902, 2009. DOI: 10.1103/PhysRevLett.103.073902.

[146] C.-G. Wahlström, J. Larsson, A. Persson, T. Starczewski, S. Svanberg, P. Salières, P. Balcou, and A. L'Huillier, "High-order harmonic generation in rare gases with an intense short-pulse laser," *Phys. Rev. A*, vol. 48, pp. 4709–4720, 6 1993. DOI: 10.1103/PhysRevA.48.4709.

[147] R. A. Ganeev, "The second plateau in the distribution of high harmonics generated in plasma torches," *Opt. Spectrosc.*, vol. 105, no. 6, pp. 930–935, 2008. DOI: 10.1134/S0030400X08120199.

[148] R. A. Ganeev, G. S. Boltaev, R. I. Tugushev, T. Usmanov, M. Baba, and H. Kuroda, "Low- and high-order nonlinear optical characterization of c60-containing media," *Eur. Phys. J. D*, vol. 64, no. 1, p. 109, 2011. DOI: 10.1140/epjd/e2011-20030-7.

[149] K. L. Ishikawa, *Advances in Solid State Lasers Development and Applications: High-Harmonic Generation*. IntechOpen, 2010, vol. 19, pp. 439–464. [Online]. Available: https://www.intechopen.com/books/advances-in-solid-state-lasers-development-and-applications.

[150] A. L'Huillier, X. F. Li, and L. A. Lompré, "Propagation effects in high-order harmonic generation in rare gases," *J. Opt. Soc. Am. B*, vol. 7, no. 4, pp. 527–536, 1990. DOI: 10.1364/JOSAB.7.000527.

[151] M. Lewenstein, P. Salières, and A. L'Huillier, "Phase of the atomic polarization in high-order harmonic generation," *Phys. Rev. A*, vol. 52, pp. 4747–4754, 6 1995. DOI: 10.1103/PhysRevA.52.4747.

[152] G. Sansone, C. Vozzi, S. Stagira, and M. Nisoli, "Nonadiabatic quantum path analysis of high-order harmonic generation: Role of the carrier-envelope phase on short and long paths," *Phys. Rev. A*, vol. 70, p. 013 411, 1 2004. DOI: 10.1103/PhysRevA.70.013411.

[153] M. Uiberacker, T. Uphues, M. Schultze, A. J. Verhoef, V. Yakovlev, M. F. Kling, J. Rauschenberger, N. M. Kabachnik, H. Schröder, M. Lezius, K. L. Kompa, H.-G. Muller, M. J. J. Vrakking, S. Hendel, U. Kleineberg, U. Heinzmann, M. Drescher, and F. Krausz, "Attosecond real-time observation of electron tunnelling in atoms," *Nature*, vol. 446, no. 7136, pp. 627–632, 2007. DOI: 10.1038/nature05648.

[154] Y. Pan, F. Guo, C. Jin, Y. Yang, and D. Ding, "Selection of electron quantum trajectories in the macroscopic high-order harmonics generated by near-infrared lasers," *Phys. Rev. A*, vol. 99, p. 033 411, 3 2019. DOI: 10.1103/PhysRevA.99.033411.

[155] G. Sansone, E. Benedetti, J.-P. Caumes, S. Stagira, C. Vozzi, S. De Silvestri, and M. Nisoli, "Control of long electron quantum paths in high-order harmonic generation by phase-stabilized light pulses," *Phys. Rev. A*, vol. 73, p. 053 408, 5 2006. DOI: 10.1103/PhysRevA.73.053408.

[156] C. Liu, Y. Zheng, Z. Zeng, P. Liu, R. Li, and Z. Xu, "Multi-quantum-path interference in high harmonic generation driven by a chirped laser pulse," *Opt. Express*, vol. 17, no. 12, pp. 10 319–10 326, 2009. DOI: 10.1364/OE.17.010319.

[157] C. Hernández-García, J. S. Román, L. Plaja, and A. Picón, "Quantum-path signatures in attosecond helical beams driven by optical vortices," *New J. Phys.*, vol. 17, no. 9, p. 093 029, 2015. DOI: 10.1088/1367-2630/17/9/093029.

[158] P. M. Paul, E. S. Toma, P. Breger, G. Mullot, F. Augé, P. Balcou, H. G. Muller, and P. Agostini, "Observation of a train of attosecond pulses from high harmonic generation," *Science*, vol. 292, no. 5522, pp. 1689–1692, 2001. DOI: 10.1126/science.1059413.

[159] H. Muller, "Reconstruction of attosecond harmonic beating by interference of two-photon transitions," *Appl. Phys. B*, vol. 74, no. 1, s17–s21, 2002. DOI: 10.1007/s00340-002-0894-8.

[160] M. Isinger, D. Busto, S. Mikaelsson, S. Zhong, C. Guo, P. Salières, C. L. Arnold, A. L'Huillier, and M. Gisselbrecht, "Accuracy and precision of the rabbit technique," *Philos. Trans. R. Soc. A: Math. Phy.s Eng. Sci.*, vol. 377, no. 2145, p. 20 170 475, 2019. DOI: 10.1098/rsta.2017.0475.

[161] A. W. Bray, F. Naseem, and A. S. Kheifets, "Simulation of angular-resolved rabbitt measurements in noble-gas atoms," *Phys. Rev. A*, vol. 97, p. 063 404, 6 2018. DOI: 10.1103/PhysRevA.97.063404.

[162] F. Wiesner, M. Wünsche, J. Reinhard, J. J. Abel, J. Nathanael, S. Skruszewicz, C. Rödel, S. Yulin, A. Gawlik, G. Schmidl, U. Hübner, J. Plentz, G. G. Paulus, and S. Fuchs, "Material-specific imaging of nanolayers using extreme ultraviolet coherence tomography," *Optica*, vol. 8, no. 2, pp. 230–238, 2021. DOI: 10.1364/OPTICA.412036.

[163] T. Ding, M. Rebholz, L. Aufleger, M. Hartmann, V. Stooß, A. Magunia, P. Birk, G. D. Borisova, D. Wachs, C. da Costa Castanheira, P. Rupprecht, Y. Mi, A. R. Attar, T. Gaumnitz, Z.-H. Loh, S. Roling, M. Butz, H. Zacharias, S. Düsterer, R. Treusch, A. Eislage, S. M. Cavaletto, C. Ott, and T. Pfeifer, "Measuring the frequency chirp of extreme-ultraviolet free-electron laser pulses by transient absorption spectroscopy," *Nat. Commun.*, vol. 12, no. 1, p. 643, 2021. DOI: 10.1038/s41467-020-20846-1.

[164] P. M. Kraus, B. Mignolet, D. Baykusheva, A. Rupenyan, L. Horný, E. F. Penka, G. Grassi, O. I. Tolstikhin, J. Schneider, F. Jensen, L. B. Madsen, A. D. Bandrauk, F. Remacle, and H. J. Wörner, "Measurement and laser control of attosecond charge migration in ionized iodoacetylene," *Science*, vol. 350, no. 6262, pp. 790–795, 2015. DOI: 10.1126/science.aab2160.

[165] J. Ullrich, R. Moshammer, A. Dorn, R. D. rner, L. P. H. Schmidt, and H. S.-B. cking, "Recoil-ion and electron momentum spectroscopy: Reaction-microscopes," *Rep. Prog. Phys.*, vol. 66, no. 9, pp. 1463–1545, 2003. DOI: 10.1088/0034-4885/66/9/203.

[166] T. Remetter, P. Johnsson, J. Mauritsson, K. Varjú, Y. Ni, F. Lépine, E. Gustafsson, M. Kling, J. Khan, R. López-Martens, K. J. Schafer, M. J. J. Vrakking, and A. L'Huillier, "Attosecond electron wave packet interferometry," *Nat. Phys.*, vol. 2, no. 5, pp. 323–326, 2006. DOI: 10.1038/nphys290.

[167] C. Schmitz, D. Wilson, D. Rudolf, C. Wiemann, L. Plucinski, S. Riess, M. Schuck, H. Hardt-degen, C. M. Schneider, F. S. Tautz, and L. Juschkin, "Compact extreme ultraviolet source for laboratory-based photoemission spectromicroscopy," *Appl. Phys. Lett.*, vol. 108, no. 23, p. 234 101, 2016. DOI: 10.1063/1.4953071.

[168] S. Anders, H. A. Padmore, R. M. Duarte, T. Renner, T. Stammler, A. Scholl, M. R. Scheinfein, J. Stöhr, L. Séve, and B. Sinkovic, "Photoemission electron microscope for the study of magnetic materials," *Rev. Sci. Instrum.*, vol. 70, no. 10, pp. 3973–3981, 1999. DOI: 10.1063/1.1150023.

[169] Z. Qu, A. Goonewardene, K. Subramanian, J. Karunamuni, N. Mainkar, L. Ye, R. L. Stockbauer, and R. L. Kurtz, "Imaging the fermi surface of cu using photoelectron spectroscopy," *Surf. Sci.*, vol. 324, no. 2, pp. 133–139, 1995. DOI: 10.1016/0039-6028(94)00701-2.

[170] C. Leforestier, R. Bisseling, C. Cerjan, M. Feit, R. Friesner, A. Guldberg, A. Hammerich, G. Jolicard, W. Karrlein, H.-D. Meyer, N. Lipkin, O. Roncero, and R. Kosloff, "A comparison of different propagation schemes for the time dependent schrödinger equation," *J. Comput. Phys.*, vol. 94, no. 1, pp. 59–80, 1991. DOI: 10.1016/0021-9991(91)90137-A.

Own publications

[T1] **L. Gulyás Oldal**, T. Csizmadia, P. Ye, N. G. Harshitha, M. Füle, and A. Zaïr, "Double-pulse characterization by self-referenced spectral interferometry," *Appl. Phys. Lett.*, vol. 115, no. 5, p. 051 106, 2019. DOI: `10.1063/1.5089959`.

[T2] **L. Gulyás Oldal**, T. Csizmadia, P. Ye, N. G. Harshitha, A. Zaïr, S. Kahaly, K. Varjú, M. Füle, and B. Major, "Generation of high-order harmonics with tunable photon energy and spectral width using double pulses," *Phys. Rev. A*, vol. 102, p. 013 504, 2020. DOI: `10.1103/PhysRevA.102.013504`.

[T3] **L. Gulyás Oldal**, P. Ye, Z. Filus, T. Csizmadia, T. Grósz, M. De Marco, Z. Bengery, I. Seres, B. Gilicze, P. Jójárt, K. Varjú, S. Kahaly, and B. Major, "All-optical experimental control of high-harmonic photon energy," *Phys. Rev. Applied*, vol. 16, p. L011001, 2021. DOI: `10.1103/PhysRevApplied.16.L011001`.

Other scientific publications

[O1] P. Ye, T. Csizmadia, **L. Gulyás Oldal**, H. N. Gopalakrishna, M. Füle, Z. Filus, B. Nagyillés, Z. Divéki, T. Grósz, M. Dumergue, P. Jójárt, I. Seres, Z. Bengery, V. Zuba, Z. Várallyay, B. Major, F. Frassetto, M. Devetta, G. D. Lucarelli, M. Lucchini, B. Moio, S. Stagira, C. Vozzi, L. Poletto, M. Nisoli, D. Charalambidis, S. Kahaly, A. Zaïr, and K. Varjú, "Attosecond pulse generation at eli-alps 100 khz repetition rate beamline," *J. Phys. B: At. Mol. Opt. Phys.*, vol. 53, no. 15, p. 154 004, 2020. DOI: `10.1088/1361-6455/ab92bf`.

[O2] D. You, K. Ueda, M. Ruberti, K. L. Ishikawa, P. A. Carpeggiani, T. Csizmadia, **L. Gulyás Oldal**, H. N. G, G. Sansone, P. K. Maroju, K. Kooser, C. Callegari, M. D. Fraia, O. Plekan, L. Giannessi, E. Allaria, G. D. Ninno, M. Trovò, L. Badano, B. Diviacco, D. Gauthier, N. Mirian, G. Penco, P. R. Ribič, S. Spampinati, C. Spezzani, S. D. Mitri, G. Gaio, and K. C. Prince, "A detailed investigation of single-photon laser enabled auger decay in neon," *New J. Phys.*, vol. 21, no. 11, p. 113 036, 2019. DOI: `10.1088/1367-2630/ab520d`.

[O3] T. Grósz, A. P. Kovács, K. Mecseki, **L. Gulyás**, and R. Szipőcs, "Monitoring the dominance of higher-order chromatic dispersion with spectral interferometry using the stationary phase point method," *Opt. Commun.*, vol. 338, pp. 292–299, 2015, ISSN: 0030-4018. DOI: `https://doi.org/10.1016/j.optcom.2014.10.047`.

[O4] T. Grósz, **L. Gulyás**, and A. P. Kovács, "Advanced laboratory exercise: Studying the dispersion properties of a prism pair," in *ETOP 2015 Proceedings*, Optical Society of America, 2015, TPE32. [Online]. Available: `http://www.osapublishing.org/abstract.cfm?URI=ETOP-2015-TPE32`.

Conference presentations

* Presenting author;   OP - Oral presentation;   PP - Poster presentation

[OP1]   P. Ye, **L. Gulyás Oldal***, T. Csizmadia, Z. Filus, T. Grósz, P. Jójárt, I. Seres, Z. Bengery, B. Gilicze, S. Kahaly, K. Varjú, and B. Major, "High-flux, 100-khz attosecond pulse train source driven by a high average-power laser beam," in *Frontiers in Optics + Laser Science*, Online, 2021.

[OP2]   **L. Gulyás Oldal***, P. Ye, Z. Filus, T. Csizmadia, T. Grósz, M. De Marco, and B. Major, "Spectrally tunable attosecond pulse generation," in *Conference on Lasers and Electro-Optics/Europe — European Quantum Electronics Virtual Conferences*, Online, 2021.

[OP3]   P. Ye, **L. Gulyás Oldal**, T. Csizmadia, Z. Filus, T. Grósz, M. De Marco, P. Jójárt, I. Seres, Z. Bengery, Z. Várallyay, B. Gilicze, S. Kahaly, K. Varjú, and B. Major*, "High-flux attosecond source at 100 khz repetition rate," in *Conference on Lasers and Electro-Optics/Europe — European Quantum Electronics Virtual Conferences*, Online, 2021.

[OP4]   T. Csizmadia*, P. Ye, **L. Gulyás Oldal**, Z. Filus, T. Grósz, P. Jójárt, I. Seres, Z. Bengery, Z. Várallyay, B. Gilicze, S. Kahaly, K. Varjú, B. Major, and M. Füle*, "Firstly commissioned secondary source of eli-alps: The hr ghhg gas beamline," in *7th ELI-ALPS User Workshop*, Szeged, Hungary, 2019.

[PP1]   **L. Gulyás Oldal***, P. Ye, Z. Filus, T. Csizmadia, T. Grósz, M. De Marco, Z. Bengery, I. Seres, B. Gilicze, P. Jójárt, K. Varjú, S. Kahaly, and B. Major, "All-optical control of high-harmonic photon energy," in *Frontiers in Optics + Laser Science*, Online, 2021.

[PP2]   **L. Gulyás Oldal***, P. Ye, T. Csizmadia, T. Grósz, Z. Filus, and B. Major, "Generation of high-order harmonics with tunable photon energy and spectral width using double pulses," in *ELI Summer School*, Szeged, Hungary, 2020.

[PP3]   **L. Gulyás Oldal***, T. Csizmadia, P. Ye, N. G. Harshitha, A. Zaïr, and M. Füle, "High-harmonic generation in gaseous medium by double pulse forms," in *7th International Conference on Attosecond Science and Technology*, Szeged, Hungary, 2019.

[PP4]   T. Csizmadia*, **L. Gulyás Oldal**, P. Ye, N. G. Harshitha, M. Füle, and A. Zaïr, "Microscopic analysis of the intensity and wavelength dependence of quantum path interferences in high-order harmonic generation," in *7th International Conference on Attosecond Science and Technology*, Szeged, Hungary, 2019.

[PP5]   N. G. Harshitha*, T. Csizmadia, P. Ye, M. Füle, **L. Gulyás Oldal**, E. Constant, and A. Zaïr, "Characterisation of attosecond pulse train using windowed rabbitt technique," in *7th International Conference on Attosecond Science and Technology*, Szeged, Hungary, 2019.

[PP6]   Z. Filus*, T. Csizmadia, M. Füle, **L. Gulyás Oldal**, N. G. Harshitha, P. Ye, B. Nagyillés, Z. Divéki, T. Tímár-Grósz, M. Dumergue, A. Zaïr, S. Kahaly, and K. Varjú, "High harmonic generation gas cell for high repetition rate secondary sources," in *7th International Conference on Attosecond Science and Technology*, Szeged, Hungary, 2019.

[PP7]   M. Füle*, P. Ye, T. Csizmadia, N. G. Harshitha, **L. Gulyás Oldal**, B. Nagyillés, Z. Divéki, T. Tímár-Grósz, M. Dumergue, Z. Filus, P. Jójárt, I. Seres, V. Zuba, Z. Bengery, M. Devetta, F. Frassetto, B. Moio, M. Lucchini, M. Nisoli, L. Poletto, S. Stagira, C. Vozzi, G. Sansone, K. Osvay, S. Kahaly, K. Varjú, and A. Zaïr, "First attosecond beamline operational at eli-alps," in *7th International Conference on Attosecond Science and Technology*, Szeged, Hungary, 2019.

[PP8]   **L. Gulyás Oldal***, T. Csizmadia, P. Ye, N. G. Harshitha, M. Füle, and A. Zaïr, "Double pulse characterisation by self-referenced spectral interferometry," in *Erice Attosecond School - The Frontiers of Attosecond and Ultrafast X-ray Science*, Erice, Sicily, Italy, 2019.

[PP9] T. Csizmadia*, **L. Gulyás Oldal**, P. Ye, N. G. Harshitha, M. Füle, and A. Zaïr., "Double pulse characterisation by self-referenced spectral interferometry," in *ELI Summer School*, Szeged, Hungary, 2018.

[PP10] N. G. Harshitha*, T. Csizmadia, **L. Gulyás Oldal**, P. Ye, M. Füle, K. Varjú, G. Sansone, and A. Zaïr, "Characterisation of attosecond pulse train using rabbitt method," in *Laser Plasma Summer School*, Salamanca, Spain, 2018.